THERMO-HYDRAULIC PERFORMANCE EVALUATION OF A SOLAR AIR HEATER HAVING DIFFERENT GEOMETRICAL PROTRUSIONS/DIMPLES AND PATTERNS IN ABSORBER PLATES

THESIS SUBMITTED BY

PREMCHAND KUMAR MAHTO

DOCTOR OF PHILOSOPHY (ENGINEERING)

DEPARTMENT OF MECHANICAL ENGINEERING

FACULTY COUNCIL OF ENGINEERING & TECHNOLOGY

JADAVPUR UNIVERSITY

KOLKATA, INDIA

2025

LIST OF PUBLICATIONS

Title of Thesis : Thermo-hydraulic performance evaluation of a solar air heater having different geometrical protrusions/dimples and patterns in absorber plates.

Name, Designation and Institute of the Supervisor : Dr. Balaram Kundu, Professor
Department of Mechanical Engineering
Jadavpur University, Kolkata, India

List of publications:

a) In International Journal

Sl. No.	Title of the paper	Name of the Journal
1	Parametric optimization of solar air heaters with dimples on absorber plates using metaheuristic approaches	Applied Thermal Engineering, 2024, p.122537.
2	Experimental and meta-heuristic optimization for the highest thermo-hydraulic performance of a solar air heater with a V-notch pattern of hemispherical protrusions on absorber surfaces	International Communications in Heat and Mass Transfer, 2024, 154, p.107440.
3	Thermo-hydraulic characteristics of solar air heaters designed with semi-capsule-shaped protrusions arranged in a staggered pattern	International Journal of Thermal Sciences, 2026,220, p.110435.

b) In Proceedings of Conference/Seminars

Sl. No.	Title of the paper	Name of the Conference Proceedings
1	Parametric Optimization of Solar Air Heaters Having Hemispherical Protrusion Roughness in the V-Notch Pattern on the Absorber Plate: A Metaheuristics Optimization Approach	Engineering Proceedings, 2024, 59(1), p.183.

c) List of Patents: Nil

d) List of presentations in National/International Conference/Seminar

Sl. No.	Title of the paper	Name of the Conference
1	Parametric Optimization of Solar Air Heaters Having Hemispherical Protrusion Roughness in the V-Notch Pattern on the Absorber Plate: A Metaheuristics Optimization Approach	International Conference on Recent Advances in Science and Engineering, Dubai, United Emirates, 4-5 October 2023.
2	Parametric optimization of solar air heater having semi-capsule protrusions on absorber plate: A metaheuristics optimization approach	3rd International Conference on Innovative Research and Development (ICIRD-2024), Shinawatra University, Thailand, 8th -11th November 2024.

STATEMENT OF ORIGINALITY

I, **Premchand Kumar Mahto,** registered on **03.07.2019,** do hereby declare that this thesis entitled **"Thermo-hydraulic performance evaluation of a solar air heater having different geometrical protrusions/dimples and patterns in absorber plates"** contains a literature survey and original research work done by the undersigned candidate as part of Doctoral studies.

All information in this thesis has been obtained and presented in accordance with existing academic rules and ethical conduct. I declare that, as required by these rules and conduct, I have fully cited and referred all materials and results that are not original to this work.

I also declare that I have checked this thesis as per the "Policy on Anti Plagiarism, Jadavpur University, 2019", and the level of similarity as checked by iThenticate software is 8 %.

.....

Signature of the Candidate

Date: 30/12/2025

Certified by Supervisor

30-12-2025

.....

Prof. (Dr.) Balaram Kundu Professor

Thesis Advisor Dept. of Mechanical Engineering

Department of Mechanical Engineering Jadavpur University, Kolkata-32

JADAVPUR UNIVERSITY

Kolkata-700032

CERTIFICATE FROM THE SUPERVISOR

This is to certify that the thesis entitled "**Thermo-hydraulic performance evaluation of a solar air heater having different geometrical protrusions/dimples and patterns in absorber plates**" submitted by **Shri Premchand Kumar Mahto**, who got his name registered on 03.07.2019 for the award of Ph. D. (Engineering.) degree of Jadavpur University is absolutely based upon his own work under the supervision of **Prof. (Dr.) Balaram Kundu** and that neither his thesis nor any part of the thesis has been submitted for any degree/diploma or any other academic award anywhere before.

30-12-2025

.....

Professor
Dept. of Mechanical Engineering
Jadavpur University, Kolkata-32

Prof. (Dr.) Balaram Kundu
Thesis Advisor
Department of Mechanical Engineering
JADAVPUR UNIVERSITY
Kolkata-700032

ACKNOWLEDGEMENT

The research presented in this thesis would not have been accomplished without the guidance and support of many individuals. I would like to take this moment to express my heartfelt gratitude to all those who contributed to the completion of this research.

Foremost, I extend my deepest appreciation to my esteemed advisor, Dr. Balaram Kundu, Professor in the Department of Mechanical Engineering at Jadavpur University. His introduction to this fascinating field of engineering, coupled with his unwavering guidance, insightful advice, encouragement, and continuous support, has been instrumental in shaping this research. His passion for research, commitment to excellence, and pursuit of high-quality work have left a lasting impact on me. He will continue to serve as an inspiration throughout my career and life.

I am also immensely grateful to the Head of the Department of Mechanical Engineering, Jadavpur University, Kolkata, for giving me the opportunity and facilities to pursue my Ph.D. I am equally grateful to Sikkim Manipal Institute of Technology, Majhitar, Sikkim, for allowing me to pursue my Ph.D. research.

I owe special thanks to Dr. Partha Protim Das and Dr. Sunny Diyaley, Mr. Chandan Sharma, Mr. Nasib Alam, and Mr. Gaurav Sapkota for their valuable cooperation, assistance, and unwavering support throughout the research process.

Lastly, I am profoundly thankful to my teachers, parents and my wife for their endless love, support, and encouragement, which have been a constant source of strength throughout this research. I am indebted to all of you for your unwavering belief in me.

Above all, I bow in gratitude to the Almighty for granting me the courage, strength, and patience needed to undertake and complete this research work.

Date: 30/12/2025

Premchand Kumar Mahto

Registration No,: 1011911003

Department of Mechanical Engineering

Jadavpur University, Kolkata, India

VITA

The author, **Mr. Premchand Kumar Mahto**, is an Assistant Professor (Selection Grade) in the Department of Mechanical Engineering at Sikkim Manipal Institute of Technology, Sikkim, India. He has eleven years of academic experience in engineering institutions. During this tenure, he has taught many subjects, like Heat Transfer, Thermal Engineering-I, Thermal Engineering-II, Power Plant Engineering, Refrigeration and Air-Conditioning, Theory of Machine-I, Alternative Fuels and Lubrications, Mechanical Vibration, and Mechanical Drawing, etc.

He obtained a Diploma of Engineering in Manufacturing Technology in 2008 from Birla Institute of Technology, Ranchi, Jharkhand. He then completed a B.Tech in Mechanical Engineering in 2011 at Sikkim Manipal Institute of Technology, Sikkim. He then obtained his M.Tech in Heat power engineering from B.I.T, Sindri, Jharkhand, in 2013. He qualified in the Graduate Aptitude Test in Engineering (GATE) examination in 2011, 2012, and 2013, conducted by the Department of Higher Education, Ministry of Human Resources Development, India. He has attended numerous workshops, seminars, webinars, and faculty development programs in technology and management.

His research interests are heat transfer, solar energy, Nano-fluids, and optimization techniques. He has guided several undergraduate projects thesis. He has published some research articles in high-repute international journals and presented several research articles at international conferences.

TABLE OF CONTENT

CHAPTER 1 1
INTRODUCTION 1
1.1 Energy Scenario 1
1.2 Solar Energy 2
1.3 Solar Air Heater 3
1.3.i Limitations of Solar Air Heaters 3
1.3.ii Importance of Artificial Roughness 5
1.3.iii Artificial roughness as protrusions/dimples 5
1.4 Optimization of influencing parameters 6
1.5 Metaheuristic Optimization Techniques 6
1.5.i Firefly algorithm 6
1.5.ii Particle-swarm optimization 7
1.5.iii Differential evolution 7
1.5.iv Teaching-learning-based optimization 8
1.5.v Ant colony optimization 11
1.5.vi Grass-hopper optimization algorithm 12
1.5.vii Whale optimization algorithm 13
1.5.viii Grey wolf optimization 14
1.5.ix Dragonfly algorithm 16
1.6 Motivation 17
1.7 Research objectives 18
1.8 Thesis Organization 18
CHAPTER 2 20
LITERATURE SURVEY 20
2.1 Application of Artificial Roughness 20
2.2 Parametric Optimization of Solar Air Heaters 23
2.3 Research Gap 25
CHAPTER 3 27
DIMPLES IN ZIG-ZAG AND STRAIGHT-LINE PATTERN 27
3.1 Introduction 27
3.2 Application of metaheuristic algorithms 28
3.3 Example 1-Dimples in a Zig-Zag Pattern 29
3.3.i Single-objective optimization 30
3.3.ii Multi-objective optimization 32
3.3.iii Hypothesis Testing: *t*-test 33

3.3.iv Results and Discussion 34
3.4 Example 2- Dimples in a straight-line pattern 35
3.4.i Single-objective optimization 37
3.4.ii Multi-objective optimization 39
3.4.iii Results and Discussion 40
3.5 Performance Comparison 40
3.6 Conclusions 41
3.7 Summary 43
CHAPTER 4 45
PROTRUSIONS IN V-NOTCH PATTERN 45
4.1 Introduction 45
4.2 Experimentation test rig 46
4.3 Parametric selection 50
4.4 Data Reduction 50
4.5 Validity test 51
4.6 Error analysis 51
4.7 Metaheuristic optimization 52
4.8 Results and Discussion 53
4.8.1 Correlations 60
4.8.1.i Correlation for Nusselt number (Nu) 60
4.8.1.ii Correlation for friction factor 63
4.8.2 Performance comparison 65
4.8.3 Optimization 67
4.8.3.i Single objective optimization 67
4.8.3.ii Multi-objective optimization 69
4.8.3.iii Validation of optimization results 71
4.9 Conclusions 72
4.10 Summary 73
CHAPTER 5 74
SEMI-CAPSULE PROTRUSIONS IN STAGGERED PATTERN 74
5.1 Introduction 74
5.2 Experimental Setup and Conduction 76
5.2.i Data Reduction 78
5.2.ii Data validation test 79
5.2.iii Uncertainty test 80
5.3 Metaheuristic optimization 80
5.4 Results and discussion 81

5.4.i Influence of Reynolds number (Re) 81
5.4.ii Effects of comparative protrusion tallness (e_c/D_h) 82
5.4.iii Influence of comparative pitch (p/e_c) 84
5.4.iv Protrusion angle (α_p) influence 86
5.4.v Thermohydraulic Performance Index (THPi) 87
5.5 Statistical correlations 88
5.6 Performance Comparison 93
5.7 Optimization 95
5.8 Conclusions 99
5.9 Summary 100
CHAPTER 6 101
CONCLUSIONS, LIMITATIONS AND SUGGESTIONS FOR FUTURE WORK 101
6.1 Introduction 101
6.2 Overall Conclusions of this Research Work 102
6.2.i Problem 1 102
6.2.ii Problem 2 102
6.2.iii Problem 3 103
6.3 Comprehensive comparison of the performance across the three problems 103
6.4 Limitations 104
6.5 Suggestions for Future Work 104
References: 106

LIST OF FIGURES

Figure 1.1: Solar Air Heater....3
Figure 1.2 : Classifications of Solar Air Heater....4
Figure 1.3 : Boundary layer over a flat plate 4
Figure 1.4 : Methods to improve the performance 5
Figure 1.5 : Flowchart of TLBO algorithm 10
Figure 1.6 : Flow chart of ACO algorithm 12
Figure 1.7 :Flow chart of GOA algorithm. 13
Figure 1.8 Flow chart of WOA algorithm 14
Figure 1.9 : Flow chart of GWO algorithm 15
Figure 1.10 : Flow chart of DA algorithm 16
Figure 3.1: Layout of protruded surface for example 1 30
Figure 3.2 : Convergence diagram for the metaheuristic algorithms for example 1 31
Figure 3.3: Box plot for the metaheuristic algorithms for example 1....32
Figure 3.4: Variations of Nusselt number to different operating parameters for example 1 35
Figure 3.5: Variations of friction factor to different operating parameters for example 1 36
Figure 3.6: Layout of dimpled surface for example 2 37
Figure 3.7: Convergence diagram for the metaheuristic algorithms for example 2 38
Figure 3.8: Box plot for the metaheuristic algorithms for example 2.....38
Figure 3.9: Variations of Nusselt number with respect to different operating parameters for example 2 41
Figure 3.10: Variations of friction factor to different operating parameters for example 2. 43

Figure 4.1: Detailed sketch of the collector: (a) Top view of the collector, and (b) Cross-section view of the collector.....47
Figure 4.2: Absorber plate:- (a) Actual absorber plate, and (b) Schematic diagram of absorber plate.....48
Figure 4.3 : Actual experimental test rig. 49
Figure 4.4 : Schematic diagram of experimental test rig. 49
Figure 4.5: Comparison of experimental and theoretical results. 52

Figure 4.6: Variation of Nu with protrusion relative height. 54
Figure 4.7: Variation of Nu with relative protrusion pitch. 55
Figure 4.8: Variation of Nu with protrusion angle of attack. 56
Figure 4.9 :Variation of friction factor with relative protrusion height. 56
Figure 4.10 :Variation of friction factor with relative protrusion pitch. 57
Figure 4.11 :Variation of friction factor with protrusion angle of attack. 57
Figure 4.12 : Variation of THPP with relative protrusion height. 59
Figure 4.13 : Variation of THPP with relative protrusion pitch. 59
Figure 4.14 : Variation of THPP with relative protrusion angle of attack. 60
Figure 4.15 :Plot of Ln(Nu) Vs. Ln (Re) 61
Figure 4.16 : Plot of Ln(C_0) Vs. Ln (h_p/D_h) 61
Figure 4.17 : Plot of Ln(C_1) Vs. Ln(p_p/h_p) 63
Figure 4.18 :Plot of Ln(C_2) Vs. Ln($\alpha_{ap}/45$) 64
Figure 4.19 : Plot of Ln(F_f) Vs. Ln(Re). 64
Figure 4.20 : Plot of Ln(k_0) Vs. Ln(h_p/D_h) 65
Figure 4.21 : Plot of Ln(k_1) Vs. Ln(p_p/h_p) 65
Figure 4.22 :Plot of Ln(k_2) Vs. Ln($\alpha_{ap}/45$) 66
Figure 4.23 :Comparison of Nu (predicted) and Nu (Experimental). 66
Figure 4.24 : Comparison of f (predicted) and f (Experimental) 67
Figure 4.25 :Convergence diagram for Nu. 68
Figure 4.26 :Convergence diagram for f. 69
Figure 4.27 : Pareto front for:- (a) ACO, (b) GOA, (c) WOA, (d) GWO, (e) DA. 70
Figure 4.28 : Validation of WOA results with experimental results for Nusselt number. 71
Figure 4.29 : Validation of WOA results with experimental results for friction factor. 72
Figure 5.1: Actual absorber plate having semi-capsule protrusions 75
Figure 5.2: Schematic representation of absorber plate 76
Figure 5.3: Experimental setup: (a) Actual experimental setup (b) Schematic diagram 77
Figure 5.4: Dimensions of the test duct. 78
Figure 5.5: Practical data validation with variations of Re: (a) Nusselt number, and (b) Friction factor. 79
Figure 5.6: Effect of Reynolds number on Nu. 82

Figure 5.7: Effect of Reynolds number on f_f. 83
Figure 5.8 : Influence of e_c/D_h on Nu. 83
Figure 5.9 : Influence of e_c/D_h on f_f. 84
Figure 5.10 : Influence of comparative pitch (p/e_c) on Nu. 85
Figure 5.11 : Influence of comparative pitch (p/e_c) on f_f. 86
Figure 5.12 : Influence of protrusion angle (α_p) on Nu. 87
Figure 5.13 : Influence of protrusion angle (α_p) on f_f. 87
Figure 5.14 : THPi vs. Reynolds number. 88
Figure 5.15 : Variation of Nu as a function of Re. 90
Figure 5.16 : Logarithmic plotting between Xo and e_c/D_h. 90
Figure 5.17 : Logarithmic variation of X_1 and p/e_c. 91
Figure 5.18 : Logarithmic plotting of X_2 and $\alpha_p/60$. 91
Figure 5.19 : Plotting in log scale of f_f and Re. 92
Figure 5.20 : Variation of Ko and e_c/D_h in log scale. 92
Figure 5.21: Variation of K_1 and p/e_c in log scale. 93
Figure 5.22 : Variation of K_2 and $\alpha_p/60$ in log scale. 93
Figure 5.23: Comparisons of experimental and correlation results for (a) Nu and (b) f_f. 94
Figure 5.24: THPi comparisons of semi-capsule protrusion with existing roughness [93],[94],[95],[96]. 95
Figure 5.25: Convergence plot for: (a) Nu, and (b) f_f. 96
Figure 5.26: Pareto front of GWOPareto front of GWO 98
Figure 5.27: Pareto front of WOA 98
Figure 5.28: Pareto front of GOA 98
Figure 5.29: Pareto front of ACO 99
Figure 5.30: Pareto front of DA 99

LIST OF TABLE

Table 3.1 : Geometric and flow parameters for example 1.....29
Table 3.2 : Results of single-objective optimization for Example1.....31
Table 3.3 : Results of multi-objective optimization for example 1. 33
Table 3.4 : Outcomes of t-test 34
Table 3.5: Geometric and flow parameters for example 2.....37
Table 3.6 : Results of single-objective optimization for example 2. 38
Table 3.7 :Results of multi-objective optimization for example 2. 39
Table 3.8: The outcomes of the paired t-test related to the TLBO algorithm for Example 2. 40
Table 3.9 : Comparisons of different studies. 43
Table 4.1: Protrusion/Dimple dimensions 47
Table 4.2: Geometric and flow parameters 50
Table 4.3: Uncertainty of measuring instruments 53
Table 4.4: Uncertainty of measurement of various parameters 53
Table 4.5: Comparison of THPP of the presented solar air heater with previous studies 67
Table 4.6: Results of single-objective optimization. 68
Table 4.7: Results of Pareto multi-objective optimization. 71
Table 5.1: Geometric and flow parameters. 78
Table 5.2: Uncertainty of gauging devices 80
Table 5.3: Uncertainty of gauging parameters. 80
Table 5.4: Results of single-objective optimization 96
Table 5.5: Optimum range for Nu and f_f using Pareto multi-objective optimization. 97

NOMENCLATURE

A_d	cross-section area duct, m^2
A_p	area of the absorber plate, m^2
c_1, c_2,	Arbitrary numbers between 0 and 1
d/D	Relative print diameter
C_p	heat capacity of air, $Jkg^{-1}\,{}^oC^{-1}$
d_p	protrusion diameter, m
D_h	mean hydraulic diameter of duct, m
e/D	Relative roughness height
e_c/D_h	relative height of protrusion
E_x	% uncertainties
f	friction factor in artificially roughened absorber plate
f_f	friction factor in artificially roughened absorber plate
f_{fs}	theoretical friction factor in smooth absorber plate
f_s	friction factor in smooth absorber plate
F	Scaling factor varies from 1 to 0
F_f	Friction factor
F_{fmin}	Minimum Friction factor
F_x, F_y	Two fireflies
f_s	friction factor in smooth absorber plate
h	convective heat transfer coefficient, $Wm^{-2}K^{-1}$
H	height of the duct, m
h_p	protrusion height, m
h_p/d_p	relative size of protrusion
h_p/D_h	relative height of protrusion
I	solar radiation, Wm^{-2}
k	thermal conductivity of air, $Wm^{-1}\,K^{-1}$
k_n	independent parameters
L	length of the absorber plate/ Length of the test section, m
P_L/e	Relative longitudinal pitch
m_1,m_2	Arbitrarily selected vectors
m	mass flow rate of air, kg/s
$\dot{m}$	mass flow rate of air, kgs^{-1}
Nu	Nusselt number for protrusion absorber plate
Nu_s	Nusselt number for smooth absorber plate
p/e	Relative pitch length
p/e_c	relative pitch
p_i	Initial position of swarm
p_i^p	Current individual position swarm
p_i^g	Best global solution
P^p	Population of generation
p_p	protrusion pitch, m
p_p/h_p	relative pitch of protrusion
Pr	Prandtl number of air
ΔP	pressure drop in test section, Pa
Q_u	heat gain by air, KJs^{-1}

r_1, r_2	Arbitrary numbers between 0 and 1
Re	Reynolds number
P_S/e	Relative lateral pitch
T_i	inlet temperature of air, ^oC
T_{ma}	mean temperature of the air in the duct, ^oC
T_0	outlet air temperature, ^oC
T_{pm}	mean temperature of the absorber plate, ^oC
THPP	thermo-hydraulic performance parameter
THPi	thermo-hydraulic performance index
U_x	uncertainties
V	velocity of air in duct, ms^{-1}
v_i	Initial velocity of swarm
V_k^p	Mutation vector
w	width of a duct, m
x	dependent parameter
X_l, X_u	Minimum and maximum levels of the search environment P^p
X_k^p	D-dimension vector

Greek Letters

α_{ap}	protrusion angle of attack
α_p	alternate protrusion angle
δx	change of dependent parameter
δk	change of independent parameter
μ	dynamic viscosity of air at T_{ma}, Nsm^{-1}
ρ	density of air at T_{ma}, kgm^{-3}
η_{th}	thermal efficiency, %
ξ	Attractiveness
γ	Light absorption coefficient
α_t	Randomization
ε_x^t	Vector of uniformly distributed random numbers with time t.

Subscript

p	protrusion
ap	protrusion attack
s	smooth absorber plate
max	Maximum
min	Minimum
c	capsule
h	hydraulic
p	protrusion
	smooth absorber plate

Abbreviations

ACO	Ant Colony Optimization
ASHRAE	American Society Of Heating, Refrigerating And Air-Conditioning Engineers
BO	Bonobo Optimization
COPRAS	Complex Proportional Assessment

CRITIC	Inter-Criteria Correlation
CSP	Concentrated Solar Power
DA	Dragonfly Algorithm
DE	Differential Evolution
FA	Firefly Algorithm
GA	Genetic Algorithm
GOA	Grass-hopper Optimization Algorithm
GRA	Grey Relational Analysis
GWO	Grey Wolf Optimization
MCDM	Multi-Criteria Decision Making
NSGA	Non Dominated Sorting Genetic Algorithm
PSO	Particle-Swarm Optimization
RSM	Response Surface Methodology
PV	Photovoltaic
SAH	Solar Air Heater
SD	Standard deviation
THP	Thermo-Hydraulic Performance
THPi	Thermohydraulic Performance Index
THPP	Thermohydraulic Performance Parameters
TLBO	Teaching-Learning-Based Optimization
VIKOR	VIekriterijumsko KOmpromisno Rangiranje
WOA	Whale Optimization Algorithm
Z	Multi-objective function

Dedicated to my teachers, parents and wife

For their endless love, support and encouragement

ABSTRACT

Our environment is facing air pollution and climate change due to the vast use of fossil fuels. It will be more problematic for humankind, as well as all living organisms, to sustain their lives in this environment. Also, the use of energy consumption is drastically increasing because of vast industrialization and improvements in the standard of living. So, the world is focusing on the maximum use of renewable energy resources as they are very environmentally friendly. Scientists are deliberately working on the development of efficient energy devices and energy conversion processes for renewable energy with minimal carbon footprint. The renewable energy can be harvested from numerous natural resources like solar, wind, water, and geothermal etc. The solar energy has the vast potential to generate energy in the terms of photo-voltaic and thermal energy. Solar thermal energy can be utilized directly or indirectly for various industrial and domestic purposes, such as in the textile industry, agriculture industry, thermal power plant, space heating, etc. Researchers have developed different space heating techniques for harvesting solar thermal energy. A solar air heater harness solar thermal energy, and heat air for various processes such as space heating, crop drying, wood drying, etc. The major drawback of solar air heaters is their low thermal efficiency because of the formation of laminar sub-layers and the low thermal conductivity of air. Researchers have suggested various techniques for the higher thermo-hydraulic performance of solar air heaters; one of the prominent methods is the use of artificial roughness in different geometrical shapes and sizes. The artificial roughness helps in breaking the laminar sub-layer, by creating more eddies, turbulence, and secondary flows, which leads to increase in convective heat transfer. The artificial roughness as protrusions/dimples has emerged as prominence ways to improve the thermo-hydraulic performance of solar air heaters. However, the application of artificial roughness impacts the overall thermo-hydraulic performance by increasing the friction losses. So, this research works emphasizes the effects of artificial roughness in the form of dimples and protrusions. An experimental and metaheuristic optimization approach has been applied for the analysis.

The performance optimization of artificially roughened solar air heater (SAH) becomes complex using analytical optimization techniques. Metaheuristic algorithms can be used as an optimization methodology to solve complex engineering problems with minimal computational efforts and high accuracy. However, due to their stochastic

nature, every metaheuristic algorithm is unsuitable for solving a specific problem. Hence, a comparative performance analysis of different metaheuristic algorithms is needed to optimize SAH. A comparative analysis of four metaheuristics algorithms, i.e., Firefly algorithm (FA), Particle swarm optimization (PSO), Differential evolution (DE), and Teaching learning-based optimization (TLBO), has been performed in optimizing the geometric and flow parameters of SAH. Two types of artificially roughened SAH absorber plate design patterns have been considered, namely, dimpled plate in a zig-zag pattern and straight-line pattern. Both single and multi-objective optimization processes have been performed while considering the maximization of Nusselt number (*Nu*) and minimization of friction factor (F_f) as two objective functions in single-objective optimization. Results showed that for both single and multi-objective optimization, the TLBO algorithm delivered better optimal solutions than the other three metaheuristic algorithms. In single-objective optimization, the maximum improvement in *Nu* and F_f is found to be 16.81% and 3.61%, respectively. In multi-objective optimization of a zig-zag pattern, the suitable parametric setting is found to be Re = 20000, P_S/e = 30.83, P_L/e = 30.83, and d/D = 0.2515. for the optimal value of *Nu* and F_f as 204.7034, and 0.0134, respectively and for straight-line pattern, it is Re = 12000, p/e= 12, and e/D = 0.0379 as with optimal values for *Nu* and F_f as 108.6901, and 0.0237, respectively.

After seeing the better performance of metaheuristic algorithms, this research work is extended to Thermo-hydraulic performances of a new solar air heater with single V-notch patterns of hemispherical protrusions on the absorber plate are investigated experimentally for different relative protrusion heights (h_p/D_h = 0.027-0.069), relative pitch (p_p/h_p = 6-14), angle of attack (α_{ap}= 15º-75º), and Reynolds number (Re =3600-21700). Also, five meta-heuristic algorithms, i.e., Ant colony optimization (ACO), Whale optimization algorithm (WOA), and Grass-hopper optimization algorithm (GOA), grey wolf optimization (GWO), and Dragonfly algorithm (DA), were used for single and multi-objective optimizations. Experimental results provide the maximum Nusselt number (Nu) as 127.07 at h_p/D_h= 0.050, p_p/h_p =10, $\alpha_{ap} = 60^0$, and Re =21700, whereas the minimum friction factor (*f*) becomes 0.0165 at h_p/D_h=0.027, p_p/h_p =10, α_{ap}= 45^0, and Re =21700. The highest normalized Nusselt number (Nu/Nu_s) is found to be 2.56 corresponding to h_p/D_h= 0.050, p_p/h_p =10, α_{ap} = 60^0, and Re =7200 and the maximum normalized friction factor (f/f_s) is observed as

4.30 at h_p/D_h= 0.050, p_p/h_p =10, α_{ap} = 45^0, and Re =7200. The highest value of thermo-hydraulic performance parameter (THPP) is found to be 1.60 corresponding to p_p/h_p =10, h_p/D_h=0.050, α_{ap} = 60^0, and Re =7200. An empirical correlation was developed. In single objective optimization for maximizing Nu, WOA provided the best results, Nu=144.56 at h_p/D_h=0.07, p_p/h_p = 8.54, α_{ap}=75^0, and Re=21700. Also, for minimizing *f*, WOA gives a minimum value of *f* = 0.012 at h_p/D_h = 0.03, p_p/h_p =14, α_{ap}=15^0, and Re =21700. The WOA metaheuristic algorithm outperformed the ACO and GOA algorithms in single and multi-objective optimization. The obtained results by GOA have been validated with experimental results.

Further, the work has been extended to explore the effects of semi-capsule-shaped protrusions in a staggered pattern. The heat transfer, flow characteristics, and thermo-hydraulic performance of solar air heater are examined experimentally with altered relative protrusion heights (e_c/D_h = 0.041-0.067), Relative pitch (p/e_c = 18-36), protrusion angle (α_p = 30º-90º), and Reynolds number (Re=3600-21700). Also, a comparative performance analysis of five metaheuristic optimization, i.e. Grey Wolf optimization algorithm (GWO), Whale optimization algorithm (WOA), Grass-hopper optimization algorithm (GOA), Ant colony optimization algorithm (ACO), and Dragonfly algorithm (DA) has been performed. From experimental results, the highest value of Nusselt number (Nu) is obtained as 182.62, at e_c/D_h=0.067, p/e_c=27, α_p= 60º, and Re=21700. The highest enhancement in heat transfer augmentation is 3.14 times than conventional solar air heater. The maximum friction factor (f_f) is 0.073, at e_c/D_h=0.067, p/e_c=18, α_p= 30º, and Re=3600. The maximum increment of friction factor is 6.66 times of a conventional solar air heater. The highest thermo-hydraulic performance index (THPi) is 2.06, at e_c/D_h=0.067, p/e_c=27, α_p= 90º, and Re=10900. The statistical correlations for Nu and f_f exhibited a satisfactory prediction with a mean absolute percentage error of ± 9.19% and ± 3.26%, respectively. For single and multi-objective optimization, the WOA has delivered best optimal solutions than others algorithms.

The Investigated solar air heaters with artificial roughness as dimples and protrusions, showed an improved thermo-hydraulic performance with the considered flow parameters, geometric parameters and roughness patterns. Based on the findings, these solar air heaters can be effectively used in various practical applications such as

agricultural drying, space heating, pre-heating of air for ventilations and industrial use etc.

Keywords: Solar air heater, Artificial roughness, Protrusions/Dimples, Hemispherical Dimples, Hemispherical protrusion, Semi-Capsule protrusion, Nusselt number, Friction factor, Thermo-hydraulic performance, Metaheuristic optimization.

CHAPTER 1

INTRODUCTION

Preface

This chapter provides an overview of energy scenarios, solar energy, solar air heaters, limitations of solar air heaters, methods to improve the limitations, different forms of roughness, the role of protrusions/ dimples, the importance of optimization of influencing parameters, different optimization techniques, the importance of metaheuristic optimization, brief details of some of the metaheuristic algorithms.

1.1 Energy Scenario

The world is drastically shifting from fossil fuel to renewable energy resources due to increased harsh climate change and the need for more sustainable energy [1]. The depletion of fossil fuels and non-renewable energy brings more concern, as it is on the brink of being exhausted [2]. Burning fossil fuels releases greenhouse gases into the atmosphere, which raises global temperatures and causes environmental instability. This causes major economic expenditures, including medical bills and infrastructure damage, upsetting ecosystems and intensifying natural disasters. Fossil fuels are economically necessary for energy generation, yet their reliance exposes economies to geopolitical tensions and market volatility. While switching to renewable energy sources reduces environmental effects and presents chances for sustainable growth, it also necessitates significant investment and legislative adjustments. A comprehensive strategy that takes into account both environmental and economic issues to address the interwoven challenges of climate change and fossil fuel dependency in order to secure a resilient and prosperous future.

An environmentally friendly substitute for fossil fuels is provided by renewable energy sources as geothermal, hydroelectric, solar, and wind power. They have a beneficial and diverse impact. They do this in two ways. First, they diminish global warming and carbon footprint by generating power with low greenhouse gas emissions. Second, they

improve energy security by lowering reliance on limited fossil fuel supplies and diversifying the energy mix, which stabilises energy prices and boosts resilience to supply interruptions. Furthermore, manufacturing, installation, and maintenance jobs are generated by renewable energy, which promotes innovation and economic progress. Their decentralised structure also encourages energy independence and democratises energy access by enabling communities to produce their own power. A future with cleaner, more sustainable, and egalitarian energy requires embracing renewable energy.

1.2 Solar Energy

Solar energy is abundantly available on the earth's surface and could be subjugated for various applications. This is where solar energy comes into play; along with being an inexhaustible, clean source, and can be supplied without any damage to our environment. Utilising solar energy has become increasingly important in India, with significant advantages and implications for the nation's energy environment. First, India is ideally suited for producing solar energy due to its abundance of sunshine receiving approximately 300-330 days annually which can generate 5000 trillion kWh energy in a year, that is more than total annual energy consumption of country. The average solar irradiation is 4 - 7 $kWh/m^2/day$, which offers a sustainable and renewable substitute for fossil fuels. The sector has experienced tremendous expansion, attracting investments and fostering innovation because of the government's ambitious solar energy ambitions and supportive regulations. By increasing access to electricity and improving livelihoods, the use of solar energy has helped reduce energy poverty in rural areas. Furthermore, by cutting greenhouse gas emissions and lowering air pollution, solar projects help India fight against climate change. Moreover, the solar industry's rise has improved energy security, boosted economic growth, and produced jobs. India's overall usage of solar energy represents a relatively small share of the total energy consumption, vast potential of solar energy demands the need for improved solar energy devices and their utilization.

There are several ways to utilize solar energy. Solar energy is directly converted into electrical power using photovoltaic (PV) cells, which may run vast cities or even tiny gadgets. Concentrated solar power (CSP) plants employ steam produced by solar thermal systems to produce electricity and heat water for domestic and commercial usage. By combining architectural elements to optimise natural light and heat, passive solar architecture lowers energy usage for heating and lighting. Solar cookers and dryers use sunshine to cook and dry food, promoting sustainability and energy independence.

Additionally, solar water and air heaters offer an effective way to heat water and air for domestic and commercial uses.

1.3 Solar Air Heater

A solar air heater is a device that heats air in homes or businesses by harnessing solar radiation. Solar air heaters absorb irradiation and alter them into heat through a medium. It usually has an insulated backing, a transparent cover, and a number of absorber plates or collectors. When sunlight enters through the transparent cover, it heats the absorber plate and further heat transfer to the flowing air. After that, the warm air is recirculated throughout the structure to serve as either primary or supplemental heating. A schematic diagram of a general solar air heater is shown in Figure 1.1. By lowering energy costs and carbon emissions, solar air heaters provide a viable and affordable replacement for conventional heating systems. They are particularly useful in areas with lots of sunlight and can be utilised in various climates. Solar heated air has many applications, such as space heating, seasoning of wood, crop drying, drying laundry, paper drying, food products drying, and many more applications as such exist[3][4]. Solar air heaters are classified based on flow pass, flow pattern, absorber design, and absorber materials, and they are integrated with PV and thermal storage types. A broad classification of solar air heaters is provided in Figure 1.2.

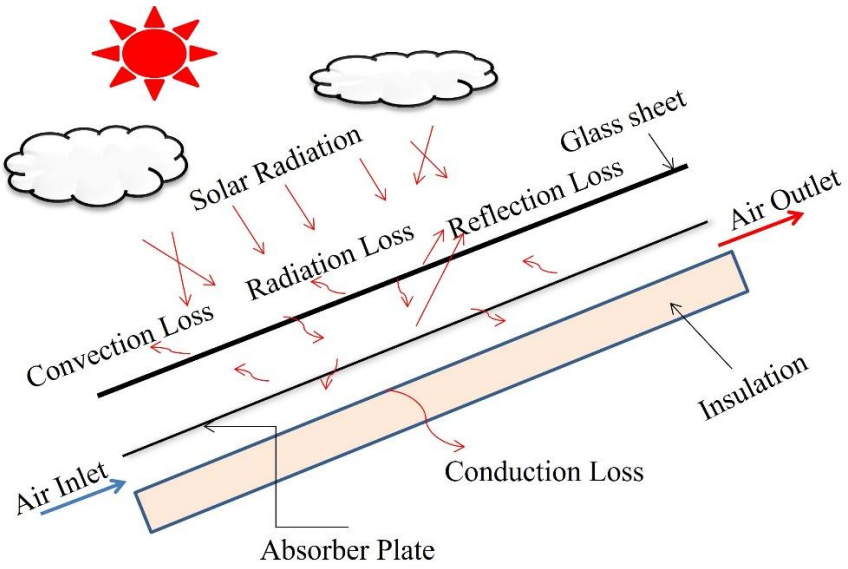

Figure 1.1: Solar Air Heater

1.3.i Limitations of Solar Air Heaters

Solar air heaters are generally cheap as they use less material to fabricate and are also more compact in comparison to solar water heaters, but these solar air heaters,

however, have low thermal efficiency because of their low heat transfer from absorber plates to the air flowing in the duct[5][6]. The low convective heat transfer coefficient is due to the generation of a viscous sub-layer that also called a laminar sub-layer that is represented in Figure 1.3. To increase the heat transfer coefficient and so the thermal performance the collector design needs to be improved.

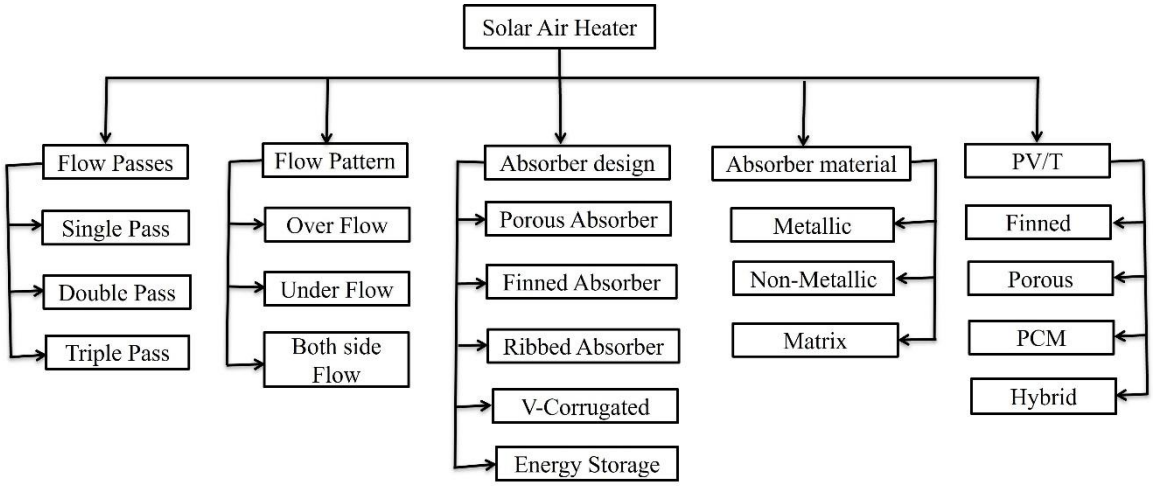

Figure 1.2 : Classifications of Solar Air Heater

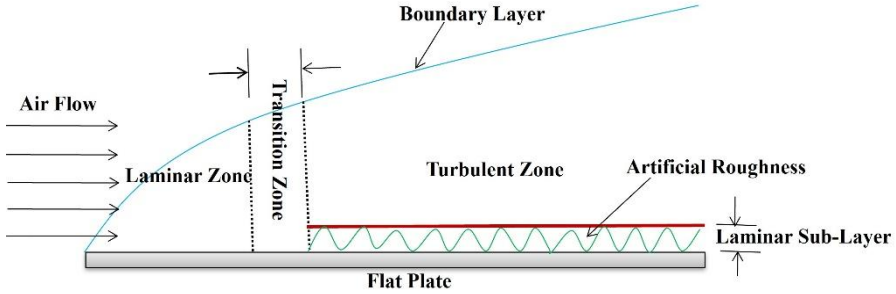

Figure 1.3 : Boundary layer over a flat plate

In past research, various methods have been used to improve the thermo-hydraulic performance of solar air heaters (SAHs)[7]. The details are represented in the below Figure 1.4.

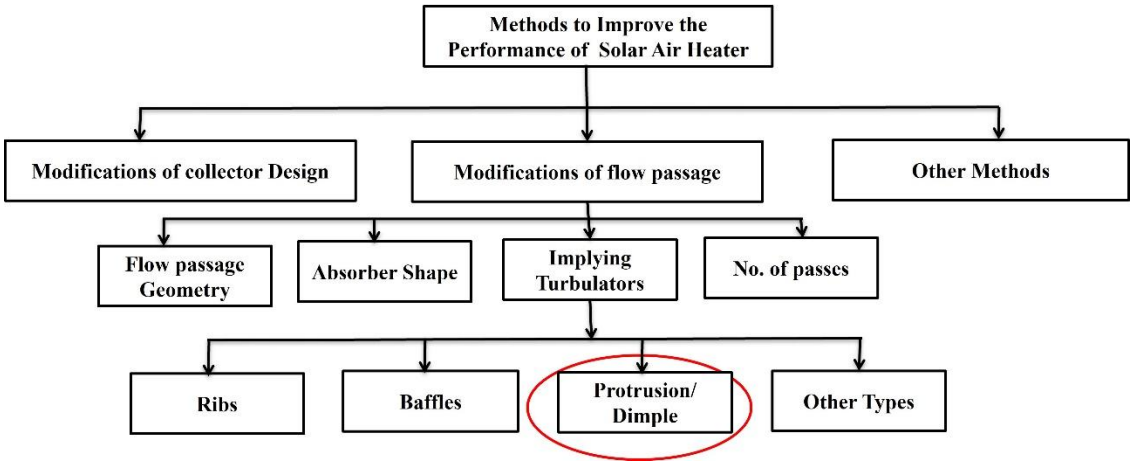

Figure 1.4 : Methods to improve the performance

1.3.ii Importance of Artificial Roughness

A turbulence flow is required in the vicinity of the heated absorber plate to improve the convective heat transfer coefficient. It can be achieved by providing artificial roughness on the surface [8]. The roughness breaks the laminar sub-layer and creates turbulence in the airflow, causing flow separation and reattachment due to the placement of the artificial roughness. Hence, the heat transfer rate increases. On the other hand, artificial roughness increases friction, which leads to higher pressure drops and more power consumption. So, to reduce the frictional losses, the turbulence created should be close to the absorber surface from where the heat is transferred, i.e. inside the laminar sub-layer. Thus, the height of the artificial roughness should be much smaller than the dimension of the duct.

1.3.iii Artificial roughness as protrusions/dimples

The use of protrusions/dimples as an artificial roughness is gaining momentum because it can be made off without any special manufacturing technique also it does not add extra weight to the absorber plate[9]. Protrusions/dimples increase turbulence, improving heat transfer between the absorber plate and the air. Enhanced heat transfer leads to higher thermal efficiency, making the solar air heater more effective at capturing and utilizing solar energy. By disrupting the laminar sub-layer, these roughness elements ensure better mixing of air, reducing thermal resistance. Protrusions/dimples elements can have different shapes and patterns; for example, the shape can be square, cylindrical, spherical, teardrop, airfoil, etc., with a different pattern such as Square pattern, V pattern, Multi-V pattern, C-arc pattern, S-pattern, etc.

1.4 Optimization of influencing parameters

Optimization techniques are crucial in engineering for enhancing performance, efficiency, and cost-effectiveness. They enable engineers to design systems and processes that maximize output while minimizing resource use and waste. Optimization techniques also facilitate solving complex problems by systematically evaluating multiple variables and constraints. Optimization techniques are broadly classified into linear and nonlinear optimization based on the nature of the objective function and constraints. They can also be categorized by variable types into continuous, discrete, and mixed-integer optimization. Deterministic and stochastic optimization differ by data certainty. Solution approaches include analytical and numerical methods, while search space strategies divide into local and global optimization. Single-objective and multi-objective optimization address the number of objectives. Finally, computational approaches consist of exact methods, which guarantee optimal solutions, and heuristic and metaheuristic methods, which provide good solutions within reasonable time frames.

1.5 Metaheuristic Optimization Techniques

Engineering challenges often involve intricate optimization problems stemming from complicated design functions and multiple design objectives. In such scenarios, metaheuristic algorithms have proven to be more effective than traditional optimization methods because of their versatility. As a result, they have developed more rapidly alongside advancements in computer processing power. Also, the metaheuristics algorithms are straightforward to apply with fewer data and the least computational time. Single-based and population-based algorithms are two significant categories of metaheuristics. Single-based metaheuristic algorithms generate single solutions. On the other hand, population-based meta-heuristic algorithms create a set of multiple solutions at each run. The population-based metaheuristic algorithms are further divided into four types, i.e., evolutionary-based, swarm intelligence-based, event-based, and physics-based. The description of some of the selected metaheuristics algorithms is presented in subsections.

1.5.i Firefly algorithm

Firefly algorithm **(**FA) is a population intelligence-based algorithm used in most optimization areas. It is simple to understand and implement. It is inspired by a firefly that produces a flashlight by Bio-luminescence in lanterns. The flashlight is used as a signal to invite the mate and is also used as a warning signal from threats. The adult firefly can control the bio-luminescence process to produce low or high-intensity flashlights. The

flushing pattern follows a particular law of physics, such as the intensity of the flashlight decreases with an increase in distance and the time interval of blink. So, the firefly uses a brightness pattern as a key objective function to live in a society. The foundation of the FA algorithm is the decentralized decision-making and self-organizing behavior of the firefly.

Let's say F_x and F_y are two fireflies, so the attraction of x_{th} firefly towards y_{th} firefly is defined as [10]:

$$F_x^{t+1} = F_x^t + \xi_0 e^{-\gamma r_{xy}^2}(F_y^t - F_x^t) + \alpha_t \varepsilon_x^t \tag{1.1}$$

where $\xi_0 e^{-\gamma r_{xy}^2}(F_y^t - F_x^t)$ defines attraction for distance r, ξ is attractiveness, γ is light absorption coefficient, α_t is randomization between 0 to 1, and ε_x^t defines a vector of uniformly distributed random numbers with time t.

In short, the FA algorithm is controlled by three parameters i.e. ξ, γ, and α_t.

1.5.ii Particle-swarm optimization

It is a popular metaheuristic procedure inspired by the preying behaviour of a bird's flock. The particle-swarm optimization **(**PSO) imitate the social behaviour of birds to communicate about their position and food source. In PSO, the position and movement of each particle are determined by the previous experience stored in each particle. The individual particle represents the solution, and the best global solution is considered. The new velocity and position of each individual are evaluated by the expressions below [11]:

$$v_i(t+1) = wv_i(t) + c_1 r_1(p_i^p(t) - p_i(t)) + c_2 r_2(p_i^g(t) - p_i(t)) \tag{1.2}$$

$$p_i(t+1) = p_{t_i}^p + v_i(t+1) \tag{1.3}$$

where c_1, c_2, r_1, and r_2 represent arbitrary numbers between 0 and 1, and w represents equal weight. p_i^p and p_i^g represents the current individual position and the best global solution, respectively. The above step is repeated until the best global solution is met.

1.5.iii Differential evolution

Like Genetic Algorithm (GA), differential evolution (DE) is also a population-based metaheuristics algorithm, but the only difference is that its optimal solution relies on mutation operation. The random generation of the population happened in the initialization phase, and then the generated population passed through the mutation, crossover, and selection processes in the evolution phase.

Initialization phase: A uniformly distributed random population is generated as per the following equation [12]:

Population of generation, $P^p = [X_k^p : k = 1,2,\ldots,np]$ (1.4)

D-dimension vector, $X_k^p = X_l + (X_u - X_l) \times rand(0,1)$ (1.5)

Where np is the population size, X_l, X_u are the minimum and maximum levels of the search environment P^p.

Mutation vectors are generated for each target vector during the mutation phase.

Mutation vector, $V_k^p = X_{m1}^P + F \times (X_{m2}^P - X_{m3}^P)$ (1.6)

Where scaling factor F varies from 1 to 0, and $m1, m2, m3 \in \{1,2,\ldots np\}$ different arbitrarily selected vectors.

In the crossover phase, the trailing vector is generated by the crossover of the original vector and mutation vector and is written as:

$$U_{i,k}^{\ p} = \begin{cases} V_{I,K}^P if rand_k \leq Cr \\ X_{i,k}^P otherwise \end{cases} \quad (1.7)$$

Where the random number $i \in \{1,2,...,D\}$ and crossover probability $Cr \in [0,1]$. In the evolution phase, the performance of the trailing vector is compared with the original vector, and a better one is selected.

1.5.iv Teaching-learning-based optimization

The teaching-learning-based optimization **(**TLBO) methodology is a human-instigated procedure that is applied in the teaching-learning process. It is established for the theory of information improvement of students by teachers in a classroom, which is further enhanced through mutual interaction among the students [13]. Like other popular optimization techniques such as Ant Colony Optimization (ACO), FA, PSO, DE, GA, etc., this technique involves a population-based meta-heuristic algorithm to find optimal global solutions. Thus, the teacher and learner phases constitute the TLBO algorithm. The teacher delivers the learning skills to learners in the first phase, and in the second phase, the acquired knowledge is upgraded among the learners through mutual interactions. Hence, the population size constitutes groups of learners in the TLBO algorithm. The design parameters are of various subjects taught, and the corresponding results are fitness values for a selected optimization problem. A flow chart explains the procedures of the TLBO

algorithm, as shown in Figure 1.5. The principle process of the above two phases is described in the sub-sections below.

Teaching phase

In TLBO algorithms, the teacher deliberates the best solution in whole solutions. In the initial phases of the algorithm, learners gain information from teachers, and teachers try to progress learners' overall performances by increasing the average score of the whole class as per competency. However, in actual practice, it depends on the ability to grasp the knowledge of individual learners, and we know all learners may not have the same ability.

A teacher shares knowledge with the learners on a particular subject and emphasizes enhancing the overall class outcome from the old mean score (m_{old}) to the new mean score (m_{new}). The algorithm developed as a teacher determines the best-identified learner. Let $X_{j,k}$, is a solution value, j represents the number of subjects taught in the class (j=1,2,3, …., m), k indicates the learners' population size (k=1,2,3, …., n), and i is used for iteration numbers (i=1,2,3,…., i_{max}). The teacher phase initiates to identify the class's best student considering all subjects. Let for an *i-th* iteration, M_j be the mean score for a subject "j" and $X_{j,kbest}$, be the best learners score of the class of that subject. In this algorithm, the teacher always puts effort into improving the overall results of the whole class for any specific subject. The global output can be achieved by estimating the change in results evaluated by the teacher and the average results of respective subjects:

$$Difference\_mean_{j,k,i} = r_{j,i}\,(X_{j,kbest,i} - T_f M_{j,i}) \tag{1.8}$$

where, $r_{j,i}$ be a random number to choose (between 0 and 1) and T_f is a teaching index factor used to calculate the mean value to be updated. Value of T_f is either 1 or 2 to be selected randomly using this equation:

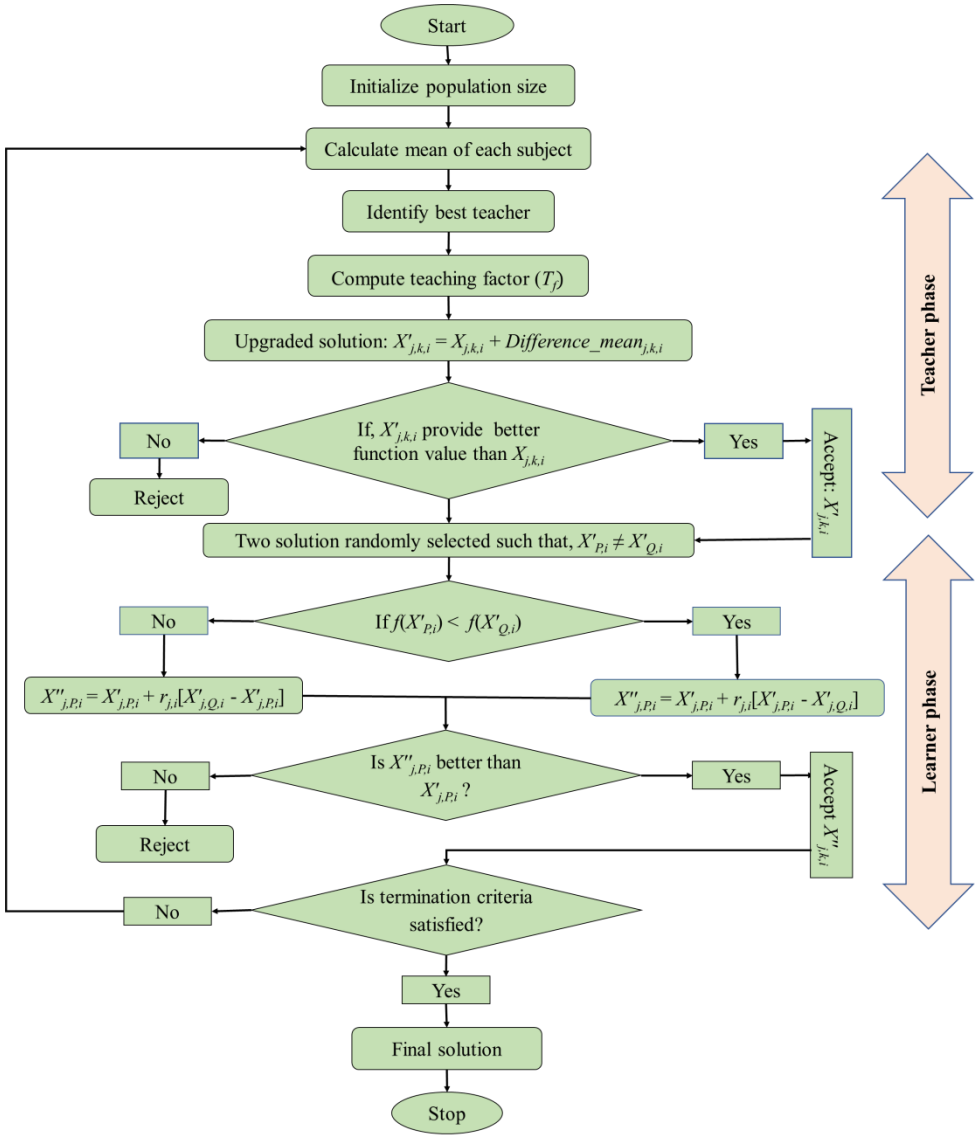

Figure 1.5 : Flowchart of TLBO algorithm

$$T_f = round[1 + rand(0,1)\{2 - 1\}] \quad (1.9)$$

Further, the solution of the $Difference\_mean_{j,k,j}$ is modified as

$$X'_{j,k,i} = X_{j,k,i} + Difference\_mean_{j,k,i} \quad (1.10)$$

where, $X'_{j,k,i}$ becomes a new upgraded and $X_{j,k,i}$ is an old value. If the $X'_{j,k,}$ provides an improved value then it becomes acceptable and retained. All these current values from the teaching phase will now serve as the inputs to the learning phase.

Learning Phase

In this learning phase, individual learner improves their knowledge through joint collaboration with fellow learners if they have more knowledge than them. In this algorithm, an individual learner is arbitrarily compared with other learners. Let's assume P

and Q are two learners for a population size of *n*. The upgraded score of 'P' and 'Q' are $X'_{P,i}$ and $X'_{Q,}$, respectively for $X'_{P,i} \neq X'_{Q,}$ at the final stage.

$$X''_{j,P,i} = X'_{j,P,i} + r_{j,i}[X'_{j,P,i} - X'_{j,Q,i}], \text{ if } f(X'_{P,i}) < f(X'_{Q,i}) \quad (1.11)$$

$$X''_{j,P,i} = X'_{j,P,i} + r_{j,i}[X'_{j,Q,i} - X'_{j,P,i}], \text{ if } f(X'_{Q,i}) < f(X'_{P,i}) \quad (1.12)$$

Finally, $X''_{j,k,I}$ is accepted if it provides improved cases. All the improved values are restored in the learning phase or procreated as input in the subsequent iteration of the teaching phase.

1.5.v Ant colony optimization

Ant colony optimization (ACO) is a metaheuristic optimization algorithm proposed by Dorigo and Di Caro [14] that draws inspiration from how ants navigate to the nearest food source from their nest. Pheromones, chemicals that ants use to communicate with one another, form the foundation of the ACO algorithm. A colony of artificial ants is employed in the ACO algorithm to look for the best answer to an optimization problem. Pheromone trails, which represent the calibre of the solutions so far, direct the artificial ants. The algorithm operates by building solutions iteratively and updating the pheromone trails depending on the efficacy of the solutions.

The ACO algorithm primarily follows initializing the pheromone trails, Construction of solutions, Evaluation of solutions, Update of pheromone trails, and termination when a stopping criterion is reached.

The mathematical model used to address any optimization problems is as follows:

$$p\left(\frac{c_i}{s_p}\right) = \frac{[\tau_i]^{\alpha}[\eta(c_i)]^{\beta}}{\sum c_j \in N(s_p)[\tau_j]^{\alpha}[\eta(c_j)]^{\beta}}, \quad \forall c_i \in N(s_p) \quad (1.13)$$

τ_i =pheromone deposition density at ith iteration, η =weight function, c_j = feasible solution, α and β =relative influence of trails.

The detailed flow chart of the ACO algorithm is provided in Figure 1.6.

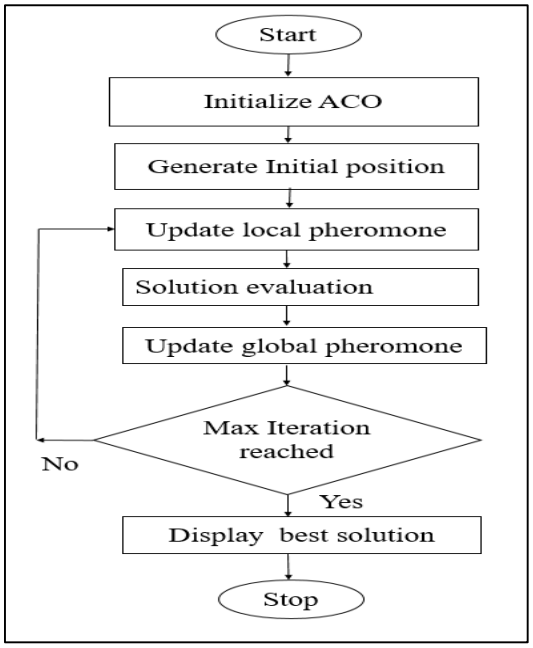

Figure 1.6 : Flow chart of ACO algorithm

1.5.vi Grass-hopper optimization algorithm

The grass-hopper optimization algorithm **(**GOA) is one of the modern metaheuristic algorithms proposed by Saremi et al. [15] in 2017, and it is applied to solve various optimization problems. It is inspired by the foraging and swarming behaviours of grasshoppers (commonly known as locusts). The grasshoppers have two phases in their life cycle, i.e., nymph and adulthood. They have different behaviours in these two phases. In the nymph phase, they move slowly with small steps, whereas in adulthood, they move brusquely with long-range. This behaviour of grasshoppers has been scientifically applied in GOA metaheuristic algorithms.

The mathematical model used to address any optimization problems is as follows:

$$X_i^d = c\left(\sum_{j=1}^{n} c\frac{ub_d - lb_d}{2} s\left(\left|x_j^d - x_i^d\right|\right)\frac{x_j - x_i}{d_{ij}}\right) + \hat{T}_d \tag{1.14}$$

$$c = c_{\max} - l\frac{c_{\max} - c_{\min}}{L} \tag{1.15}$$

where, ub_d and lb_d is higher and lower bound in d_{th} solution, T_d represents current best solution, c represents degree of comfort, and s represent social power.

The detailed flow chart of GOA algorithm is provided Figure 1.7.

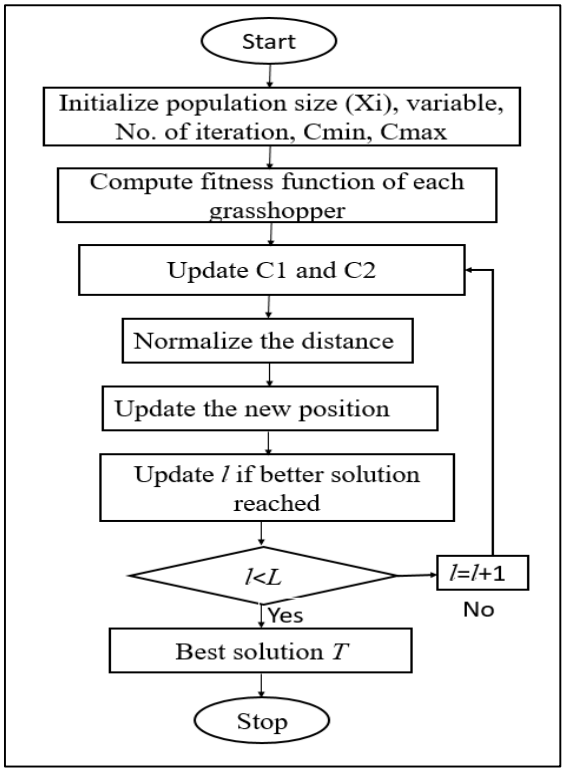

Figure 1.7 :Flow chart of GOA algorithm.

1.5.vii Whale optimization algorithm

The whale optimization algorithm (WOA) is a metaheuristic optimization algorithm proposed by Mirjalili et. al [16] in 2016. It is inspired by the bubble net attacking method, a hunting strategy of humpback whales. This is a unique method used by only humpback whales to hunt a school of small fish. In this method, whales initially dive around 12 m down from the water's surface and then start creating bubbles around the prey in a spiral shape, and then swim upward to catch the fish.

The mathematical model used to address any optimization problems is as follows:

$$\vec{x}(t+1) = \begin{cases} \vec{x}^*(t) - \vec{A}.\vec{D}, if p \leq 0.5 \\ \vec{D}'.e^{cr}.cos(2\pi r) + \vec{x}^*(t), if p \geq 0.5 \end{cases} \quad (1.16)$$

r = random number between [-1,1], c=constant for defining the shape of a spiral, $\vec{D}'$is the distance of ith whale from the target, p=probability of success, $\vec{A}$ is variation vector, x= position vector.

The detailed flow chart of the WOA algorithm is provided in Figure 1.8.

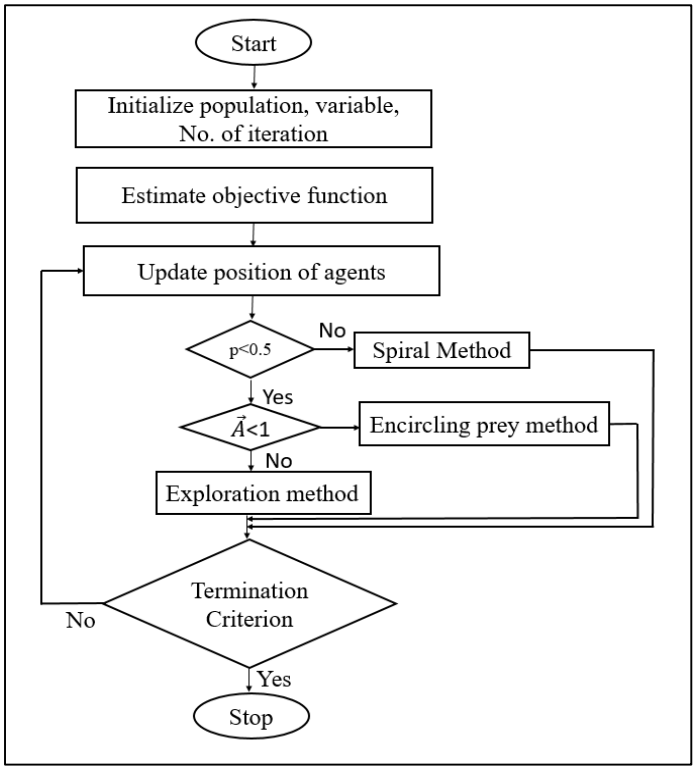

Figure 1.8 Flow chart of WOA algorithm

1.5.viii Grey wolf optimization

Scientifically called Canis Lupus (Grey Wolf) belongs to the Canidae family, considered as apex predator in the food chain. A group of grey wolves consists of four social hierarchies. Group hunting is the main process of collecting their food. The grey wolf optimization **(**GWO) optimization method is motivated by the social hierarchy and hunting techniques of the grey wolf and is mathematically modeled as follows [17]: Social hierarchy: GWO optimization is guided by Alfa, supported by Beta, and Delta, and followed by Omega. Alfa is considered the first best solution followed by Beta, and Delta.

Encircling of prey: Encircling of prey is the first phase in the hunting process. The Encircling of prey can be modeled as follows:

$$\vec{m} = \left|\vec{C} - \overrightarrow{X_p}(t) - \overrightarrow{X_w}(t)\right| \quad (1.17)$$

$$\overrightarrow{X_w}(t+1) = \left|\overrightarrow{X_p}(t) - \vec{k} \cdot \vec{m}\right| \quad (1.18)$$

$$\vec{k} = 2\vec{a} \cdot \overrightarrow{r_1} - \vec{a} \quad (1.19)$$

$$\vec{C} = 2 - \overrightarrow{r_2} \quad (1.20)$$

Where, t =current iteration, $\vec{k}$ and $\vec{m}$ = coefficient vector, $\overrightarrow{X_p}$ =position vector of prey, $\overrightarrow{X_w}$ = position vector of Grey wolf, $\vec{a}$ =linearly decrease from 2 to 0, and r1, r2 are random vector (0,1).

Hunting: the hunting model can be considered as follows

$$\overrightarrow{m_\alpha} = \left|\overrightarrow{C_1} - \overrightarrow{X_\alpha} - \overrightarrow{X_w}\right|, \overrightarrow{m_\beta} = \left|\overrightarrow{C_1} - \overrightarrow{X_\beta} - \overrightarrow{X_w}\right|, \overrightarrow{m_\delta} = \left|\overrightarrow{C_1} - \overrightarrow{X_\delta} - \overrightarrow{X_w}\right| \quad (1.21)$$

$$\overrightarrow{X_1} = \overrightarrow{X_\alpha} - \overrightarrow{k_1} \cdot \overrightarrow{m_\alpha}\,, \overrightarrow{X_2} = \overrightarrow{X_\beta} - \overrightarrow{k_2} \cdot \overrightarrow{m_\beta}\,, \overrightarrow{X_3} = \overrightarrow{X_\delta} - \overrightarrow{k_3} \cdot \overrightarrow{m_\delta} \quad (1.22)$$

$$\overrightarrow{X_w}\,(t+1) = \frac{\overrightarrow{X_1}+\overrightarrow{X_2}+\overrightarrow{X_3}}{3} \quad (1.23)$$

Attacking (Exploitation): In the mathematical model, as $\vec{a}$ linearly decreased from 2 to 0 in each search, simultaneously $\vec{k}$ decreases with $\vec{a}$. Once the random value of $\vec{k}$ lies between -1 to 1, the subsequent location of search agent lies between the present location and location of prey.

Exploration: The global search in all the possible regions comes under the exploration phase, and it is done once the result is stuck in local optima. When the value of $\vec{k} > 1$, or $\vec{k} < -1$, the search agent diverges from the prey, and if $\vec{k} < 1$, the search agent converges with the prey and finally comes up with a final solution. A flow diagram of the GWO algorithm, as discussed, is presented in Figure 1.9.

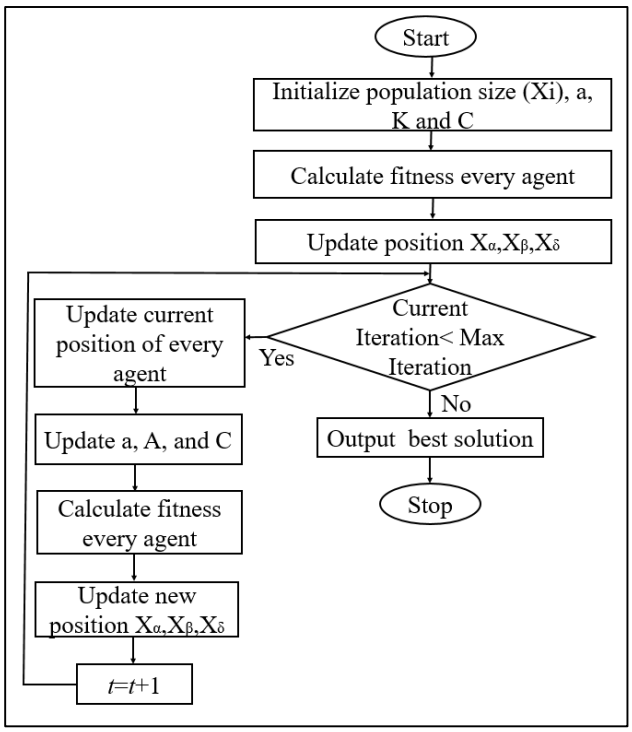

Figure 1.9 : Flow chart of GWO algorithm

1.5.ix Dragonfly algorithm

Scientifically called Odonata (Dragonflies) is an insect having more than 3000 varieties in the world. The dragonfly algorithm **(**DA) is inspired by the swarming behaviour of dragonflies and consists of two types i.e., static and dynamic. Static behaviour is considered under the exploration phase, in which a group of dragonflies fly around different locations. A large number of dragonflies move in specific directions in search of food, which is considered to be under the exploitation phase of the metaheuristic algorithm. To mimic the flying motions of dragonfly separation motion (S_i), Alignment motion (A_i), cohesion motion (C_i), Attraction towards food (F_i), and distraction to predator(P_i) can be mathematically modelled as follows [18]:

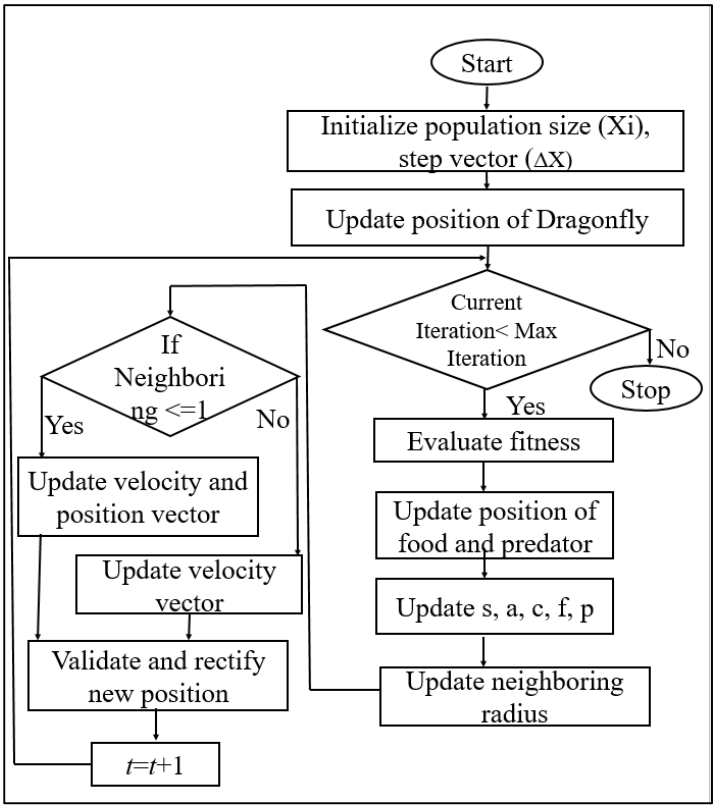

Figure 1.10 : Flow chart of DA algorithm

Separation, $S_i = -\sum_{j=1}^{n} X - X_j$ (1.24)

Alignment, $A_i = \frac{\sum_{j=1}^{n} V_j}{n}$ (1.25)

Cohesion, $C_i = \frac{\sum_{j=1}^{n} X_j}{n} - X$ (1.26)

Attraction towards food, $F_i = X^+ - X$ (1.27)

Distraction from predators, $P_i = X^- + X$ (1.28)

where X is the location of the individual, X_j is the location of the j^{th} dragonfly, n is the number of the total number of neighbouring individuals, X^+ is the position of food, and X^- is the predator's position. Step vector (ΔX) and location vector (X) are two major parameters to update the current location and are calculated using the following equations:

$$\Delta X_{(t+1)} = (sS_i + aA_i + cC_i + fF_i + pP_i) + \omega \nabla X_t \quad (1.29)$$

$$X_{(t+1)} = X_t + \Delta X_{(t+1)} \quad (1.30)$$

where s, a, c, *f*, and p are the weight of each motion, ω is inertia weight, t= iteration number, and t+1 is the current iteration. As discussed above, a flow diagram of the DA algorithm is provided in Figure 1.10.

1.6 Motivation

Earth is facing global warming and climate change due to the vast use of fossil fuels. Also, the energy crisis is drastically increasing because of vast industrialization and improvements in the standard of living. So, the world is focusing on the maximizing the use of renewable energy resources to mitigated the environmental issues and fulfil the energy demand. Scientists are deliberately working on the development of efficient energy devices and energy conversion processes for renewable energy with minimal carbon footprint. A solar air heater emerged as a solar thermal capturing device that heat air by capturing solar thermal energy, and heated air further utilized for various processes such as space heating, crop drying, wood drying, etc. But, solar air heaters bear a major drawback of low thermal efficiency because of the formation of laminar sub-layers and the low thermal conductivity of air. Researchers have suggested various techniques for the higher thermo-hydraulic performance of solar air heaters; one of the prominent methods is the use of artificial roughness in the form of different geometrical shapes and sizes over the absorber plate. The artificial roughness helps in breaking the laminar sub-layer, which creates more eddies/ turbulence in flowing air, which leads to higher convective heat transfer. The artificial roughness as protrusions/dimples has emerged as prominence ways to improve the thermo-hydraulic performance of solar air heaters. However, the application of artificial roughness impacts the overall thermo-hydraulic performance of solar air heater by increasing the friction losses. So, this research works took attempt to investigate the performance of solar heater having different dimples and protrusions with varying patterns.

The optimizations of flow and geometric parameters are the another challenge, which is addressed by adopting different metaheuristic optimization techniques.

1.7 Research objectives

Based on the stated research gaps, the following research objectives are drawn:

- To analyse the thermo-hydraulic performance of a solar air heater with various shapes, sizes, and patterns of the protrusions/dimples as artificial roughness on the absorber plates.
- To develop a statistical correlation for the Nusselt number and the friction factor.
- Apply metaheuristic algorithms to determine appropriate parametric settings to achieve optimal performance of solar air heaters.
- To conduct comparative performance analyses of selected metaheuristic algorithms.

1.8 Thesis Organization

This thesis organized into six chapters. Chapter 1 provides an overview of energy scenarios, solar energy, solar air heaters, limitations of solar air heaters, methods to improve the limitations, different forms of roughness, the role of protrusions/ dimples, the importance of optimization of influencing parameters, different optimization techniques, the importance of metaheuristic optimization, brief details of some of the metaheuristic algorithms, motivation, and objectives of this research. Chapter 2 provides comprehensive literature survey related with the use of artificial roughness as dimples and protrusions in solar air heaters. This literature survey also comprises the applications of various optimization techniques used in the parametric optimization of solar air heaters. The applications of metaheuristic optimization algorithms are the center of interest. Chapter 3 focused on the parametric optimization of solar air heater having dimples in zig-zag and straight-line patterns using four metaheuristics algorithms, i.e. FA, PSO, DE, and TLBO. Chapter 4 focused on experimental and metaheuristic optimization analysis of a solar air heater having hemispherical protrusions in a V-notch pattern on the absorber plate. This chapter describe the experimental setup, methodology, data validation, and uncertainty analyses, influence of flow and geometric parameters, and development of statistical correlation for the Nusselt number and friction factor. Further, the parametric optimization

using five metaheuristic algorithms, i.e., ACO, WOA, GOA, GWO, and DA have been performed. Chapter 5 focused on the thermo-hydraulic performance of solar air heater having semi-capsule protrusions in a staggered pattern. The performance of SAH has been examined experimentally, and optimization of flow and geometric parameters were investigated using all five metaheuristic algorithms, which are applied in chapter 4. Chapter 6 summarized the overall conclusions, comprehensive comparison across the considered solar air heaters, limitations and scope for future work of this research.

CHAPTER 2

LITERATURE SURVEY

Preface

The objectives of this thesis are derived after a thorough assessment of the literature. This literature survey comprises different methodologies used to enhance the performance of solar air heaters. The utmost focus is given to applications of artificial roughness as protrusions and dimples. This literature survey also comprises the applications of various optimization techniques used in the parametric optimization of solar air heaters. The applications of metaheuristic optimization algorithms are the center of interest

2.1 Application of Artificial Roughness

A solar air heater is characterized by its cost-effectiveness and low maintenance requirements. Nevertheless, it demonstrates suboptimal thermo-hydraulic performance (THP), which can be attributed to the poor thermo-physical properties of air and the development of a laminar sub-layer in closeness to the heated surface [19]. The laminar sub-layer restricts heat transfer between the absorber plate and the medium. Due to the widespread use of solar air heaters, researchers are consistently working to improve their efficiency. One effective approach to tackle this problem is the addition of artificial roughness to the absorber plate of solar air heaters (SAHs). Many studies have been conducted to assess the performance of SAHs featuring different shapes and patterns of roughness on the absorber plate [20],[21]. The roughness has been used in the form of winglets [22][23], ribs [23][24][25], perforated blocks/wings [8], turbulators [26], and Fins [27] etc.

The addition of artificial roughness externally has several disadvantages, such as considerable pressure drops, high friction losses, difficulties in manufacturing, bulkiness, and greater maintenance needs. As a result, these types of absorber plates are not widely adopted for commercial applications. Recently, the addition of protrusions/dimples to absorber plates has been recognized as a promising method to improve the thermal

efficiency of SAHs. Protruded/ Dimpled SAHs have shown a significant enhancement in THP compared to other roughness types, while keeping pressure drop and frictional losses to a minimum. Moreover, the dimples are formed using a punch-and-die process, which does not increase the weight of the absorber plate. Various studies have investigated protrusion/ dimple roughness, yielding positive outcomes in comparison to traditional artificial roughness. Kumar et al. [28] reported THP enhancement by 7% using dimples in a V-pattern. Sevik et al. [29] observed an enhancement in energy efficiency by 37.9% and 53.5% for backwards and forward-pass solar air heater while applying convex dimples in a staggered pattern. The enhancement was due to the enlargement in surface area and high turbulence generation. Salman et al. [30] observed THP improvements by 3.86 times of conventional SAH using an impinged jet on a dimpled absorber plate. Saini and Verma [31] investigated the correlations between heat transfer and friction factors for an absorber plate with dimpled roughness. Reynolds number, relative pitch, and relative height are the major factors impacting the friction factor and Nusselt number. The maximum and minimum values of the Nusselt number and friction factor were observed at e/D=0.037, p/e=10, and e/D=0.0289, p/e=10, respectively.

Hwang et al. [32] investigated heat transfer characteristics with different dimples/protrusions. The performance enhancement was found to be 14 and 7 times with dual protrusion and dimple. Sethi and Thakur [33] experimented with spherical dimples in an arc-shaped pattern. They reported the highest heat transfer at P/e of 10. Luo et al. [34] numerically considered the effect of dimple arrangement on the flow arrangement with delta winglet vortex generators. It was found that the adoption of dimples considerably interacts with the vortex generated, and that became an advantage for heat intensification because of the penetration of vortex fluid into the dimpled surface. Investigated by Kumar [35] on exergy analysis of solar air heaters with one and 3-side concave dimples reveals an improvement in exergetic efficiency from 0.0172 to 0.023 concerning different p/e, e/Dh, and e/d values. Kumar et al. [36] inspected the influence of roughness in the form of alternate protrusion and dimples on the absorber plate. They reported an increment in heat augmentation in the leading end of dimples due to higher flow separation and reattachment of flowing air. The maximum increment in thermal augmentation and overall performance was found to be 2.1 and 1.95 times over the smooth absorber plate. Bhushan et al. [37] have investigated the effects of spherical dimples on roughness in solar air heaters. The THP parameters were found 2.2-3.8 times higher than the plane surface. Salman et al. [38]

have reported an improved thermal efficiency by 18%-29% using jet-impinged dimpled roughness on absorber plates. Panda and Kumar [39] wrote an experimental investigation on the effects of solar intensity and air flow on Inline spherical dimples. The Nusselt number and friction factor were reported to be improved by 1.83 and 2.76 times higher that of conventional absorber plate. Shaik et al. [40] performed CFD analysis on alternate dimples and protrusion inclusions on the absorber plate. The maximum heat augmentation was found to be 8.27% more than the smooth duct, and the maximum THP was found to be 2.01%.

Aryan et al. [41] examined the performance of SAHs with different miniatures combined with dimples. The highest thermohydraulic performance was 1.63, corresponding to an angle of attack of 45°, l/d of 20, and w/D_h of 0.18. Prakash and Saini [42] experimented using spherical and inclined ribs as roughness. They noted an enrichment in THP parameters by 2.88 and 1.58 times. The maximum THP index was observed to be 3.66. Raju et al. [43] performed a computational analysis to examine the effects of alternate intrusion and protrusion in the triangular ducts. They found the highest performance at a relative roughness pitch of 14 and a relative transverse distance of 18. Moon et al. [44] observed the effect of channel height for a dimpled surface rectangular duct. The improvements in heat transfer coefficient were found to be 2.0 times, and the pressure drop was 16.-2.0 times more than the smooth surface. Chyu et al. [45] testified appreciable enhancement in heat transfer coefficient with hemispherical and teardrop dimples as compared to a smooth wall. The heat transfer rate was 2.5 times higher, and the pressure drop caused by friction was approximately 0.5. Schukin et al. [46] investigated the effect of the hemispherical cavity on heat transfer augmentation. They reported an improvement in heat transfer as compared to plane wall. Also, It was reported that the reason of laminar boundary layer reduces due to the cavity. Moon and Lau [47] experimented and came to the finding that the overall heat transfer rate increases by 1.7 times with concave and cylindrical dimple protrusions. Khalatov et al. [48] conducted an investigation on flow characteristics over spherical and cylindrical dimples at low Reynolds numbers. They observed different flow features for this case and reported that the Reynolds number, shapes of dimple, and the existence of neighboring dimples played important roles for flow pattern formation. Bhushan and Singh [49] performed an examination on the cause of spherical protrusions, they found the maximum thermal and hydraulic performance at P_S/e of 31.25 and P_L/e of 31.25 each. Nadda et. al. [50] discussed

and determined the flow of air with an impingement jets on multi arcs protrusions. Experiments were conducted at a range of Re =5000-19000. The findings show the maximum rise in the Nusselt number was at W/d of 5.0 and the highest friction factor corresponded to a relative width ratio of 6.0. the biggest improvement in Nu and *f* was found to correspond to a relative pitch ratio of 9.5. Singh et al. [51] experimented with the effect of multiple arc shape roughness. The highest improvement in Nu and *f* was reported as 5.07 and 3.71 times, respectively. Elyyan et al. [52] have reported that the dimpled surface of a heat exchanger provides enhanced results in heat transfer due to the better augmentation of heat. Lin et al. [53] have studied the 3D flow characteristics for the hemispherical dimpled surface. The results show an improved performance than a smooth surface. Ligrani et al. [54] have investigated shallow dimple channels and reported that the dimpled reason provides maximum value for Nu and f increase and increase in turbulence intensity. Acharya et al. [55] have investigated the effect of dimples using the Naphthalene sublimation method. They considered different shapes of the dimples in their study, and they reported that the teardrop-shaped dimples showed better results.

2.2 Parametric Optimization of Solar Air Heaters

A significant improvement in the performance of SAH has been reported because of the provision of dimples on absorber plates. The implication of dimples helped break the laminar sub-layer and hindered the flow characteristic with minimal frictional losses. However, dimples' shape, size, and pattern play an important role in overall performance improvement. Hence, careful consideration should be given when selecting these parameters to achieve maximum heat transfer with minimum friction loss. Several parametric optimization techniques have been employed to optimize the geometric and flow parameters parameters. Varun [56] applied a Genetic algorithm (GA) to identify the optimal parametric values of flat plate SAH without roughness. Ansari and Bazargan [57] investigated the performance of SAH with ribbed surfaces. They applied GA to determine the optimal combination of control parameters to achieve maximum thermal efficiency and the desired inlet and outlet airflow temperature difference. Hu et al. [58] applied the orthogonal numerical technique to optimize various design parameters of an SAH with roughness as a hole baffle. Kumar et al. [59] performed experiments for discrete multiple-arc-shaped ribs with roughness fixed underside an absorber plate of a SAH. Response surface methodology (RSM) was later applied to identify the optimal roughness parameters, showing a remarkable thermal performance improvement. Qader et al. [60]

used the RSM approach to investigate the optimal design parameters of an SAH for enhancing the thermo-hydraulic performance by inclined fins roughness. Applying Non Dominated Sorting Genetic Algorithm (NSGA-II), Gholami et al. [61] select the best-influencing parameters for arcuate-shaped obstacles in a SAH. Chauhan and Kim [62]applied the entropy-VIKOR method to discover the optimal control parameters for solar air heaters' roughness as dimples/protrusions. The best performance was found at an arc angle of 60º. Mohanty et al. [63] used an integrated RSM and PSO algorithm to identify a three-sided roughened absorber plate's optimal Nusselt number and thermal efficiency. To enhance the exergy efficiency of a SAH having arc-shaped roughness with fins and baffles, Kumar et al. [64] adopted GA to identify the optimal design and operating parametric condition. Dezan et al. [65] combined the anisotropic kriging model and NSGA-II to obtain the optimal performance condition of a SAH with three rows of delta winglet roughness. Considering rib geometry and flow parameters as input parameters. The results show that the non-periodically arranged vortex generators are able to produce the highest performance. Korpale et al. [66] applied RSM to maximize the thermo-hydraulic performance of SAH with an absorber plate having rectangular ribs. Bezbaruah et al. [67] investigated the influence of truncated half-conical bumpiness on absorber plates of a SAH and applied grey relational analysis (GRA) to identify the best configuration of input parameters. Kumar and Layek [68] studied the performance of twisted rib solar heaters. They used PSO and TLBO metaheuristic algorithms to determine the optimal solutions.

Luo et al. [69] applied the NSGA-II optimization algorithm for the optimization of process parameters of solar collectors having dimples/protrusions on the absorber plate. The optimal combination of parameters showed an improvement in thermal performance by 72%. Sharma et al. [70] adopted hybrid ENTROPY-VIKOR, an multi-criteria decision making (MCDM) approach, to determine the optimal parameter setting for solar air heaters having secret V-obstacles as an artificial roughness. The maximum improvement in thermal, hydraulic, and collector efficiency was reported as 6.2%, 8.4%, and 1.47%, respectively. Acır et al. [71] adopted GRA to ascertain the optimum parametric settings, and it delivered a satisfactory result. Kumar et. al [72] conducted parametric optimization of SAH using inter-criteria correlation (CRITIC) and complex proportional assessment (COPRAS) hybrid techniques. The optimal thermos-hydraulic performance was discovered to be 4.1, corresponding to the best parametric setting. Pramod et al. [73]

evaluated bonobo optimization (BO), PSO and TLBO for different types of roughness used in SAHs. The results show that the BO algorithms outperformed over others. Mishra et al. [74] applied the APH-TOPSIS method to optimize the parameters of multi-arc protrusions. The results recommended that a relative width of 3, height of 1, pitch of 9.5, arc angle of 55, and Reynolds number of 19,00 are suitable parameters for optimal performance of impingement jet solar air heater.

2.3 Research Gap

The extensive literature survey reveals that using roughness as protrusions or dimples becomes attractive for researchers as its embossing in the absorber plate is easy and without extra weight. Also, flow over the protrusion and dimples is easy with minimum friction. These features motivated the authors to investigate roughness as protrusions/dimples. Several studies have investigated the influence of artificial roughness used as protrusions/dimples with different shapes and patterns. However, no studies have reported on hemispherical protrusions as artificial roughness in a single V-notch pattern with the entry of cold air from the V-apex side. These patterns make this roughness unique, and it assumes that the given patterns reduce the frictional resistance at the entrance and help to develop a strong secondary flow downstream that will improve heat augmentation. Also, the authors found limited studies on roughness in the form of semi-capsule-shaped protrusions with successively altered orientations engraved on the absorber plate. This roughness would be able to increase secondary flow and vortices generation and may improve thermohydraulic performance. So, the authors emphasize these research gaps for further investigations.

Further, the literature review also discloses that various analytical and metaheuristic optimization techniques have been explored by researchers for determining the best parametric settings for optimal performance of SAHs. It was observed that the analytical optimization techniques face difficulties in optimization of complex problems. However, the metaheuristic algorithms based optimization techniques supersede in optimization problems having multi, non-linear, distinct, and unceasing variables with fewer information, and more computational effort [75]. But, each metaheuristic algorithms having unique behavior while solving the problems due it their stochastic natures. So, a comparative performance investigation is outmost required for a particular optimization problem. To the best of the author's knowledge, very few comparative optimization performance analysis of different metaheuristic algorithms has been reported in the domain

of SAH having artificial roughness in the form of protrusions/dimples. Hence, this research work also emphasizes the application of metaheuristic algorithms, namely, firefly algorithm (FA), particle swarm optimization (PSO), differential evolution (DE), and teaching-learning-based optimization (TLBO), Ant colony optimization (ACO), Whale optimization algorithm (WOA), and Grass-hopper optimization algorithm (GOA), Grey Wolf optimization (GWO), Dragonfly algorithm (DA) to identify suitable flow and geometric parameters for optimal performance of SAHs having distinct patterns of protrusion/dimple roughness on the absorber plate. The inspiration behind the selection of these metaheuristic algorithms is to compare the optimization performance of Bio-inspired, Swarm intelligence-inspired, evolution-inspired, and human-inspired algorithms in solving the same problem.

CHAPTER 3

DIMPLES IN ZIG-ZAG AND STRAIGHT-LINE PATTERN

Preface

In this chapter, a single and multi-objectives parametric optimization of solar air heaters using four metaheuristics algorithms, i.e., Firefly algorithm (FA), Particle swarm optimization (PSO), Differential evolution (DE), and Teaching learning-based optimization (TLBO) are performed. Two different types of artificially roughened solar air heaters (SAHs) having dimples in zig-zag patterns and straight-line patterns are investigated.

3.1 Introduction

The performance optimization of artificially roughened solar air heater becomes complex using analytical optimization techniques. Metaheuristic algorithms can be used as an optimization methodology to solve complex engineering problems with minimal computational efforts and high accuracy. However, due to their stochastic nature, every metaheuristic algorithm is unsuitable for solving a specific problem. Hence, there is a need to perform a comparative performance analysis of different metaheuristic algorithms in optimizing solar air heater (SAH). This chapter presents a comparative performance analysis of four metaheuristics algorithms, i.e., FA, PSO, DE, and TLBO in optimizing the geometric and flow parameters of SAH. Two types of artificially roughened SAH absorber plate design patterns have been considered, namely, dimpled plate in zig-zag pattern and straight-line pattern. Both single and multi-objective optimization processes have been performed while considering the maximization of Nusselt number (Nu) and minimization of friction factor (F_f) are two objective functions in single-objective optimization.

The performance comparison of different metaheuristic algorithms is complex in terms of delivering optimal solutions and convergence due to its stochastic nature. Each algorithm may not be suited for a particular problem and requires modification for optimal results. So, there is a need to perform a comparative performance analysis of different

metaheuristic algorithms in optimizing SAH. To the best of the author's knowledge, no such comparative optimization performance analysis of different metaheuristic algorithms has been reported in the domain of SAH having artificial roughness in the form of dimples. Hence, this research work emphasizes the application of four metaheuristic algorithms to identify suitable geometric and flow parameters for optimal performance of two different SAH having distinct patterns of dimpled roughness on the absorber plate. Out of two considered SAHs, one has artificial roughness as dimples in a zig-zag pattern, while the other has in a straight-line pattern. The inspiration behind selecting these metaheuristic algorithms is to compare the optimization performance of Bio-inspired, Swarm intelligence-inspired, evolution-inspired, and human-inspired algorithms in solving the same problem. This is of utmost importance to identify the best metaheuristic algorithm that can help design and develop high-end performing SAH.

3.2 Application of metaheuristic algorithms

This section provides an overview of the application of four popular metaheuristic algorithms, which are FA, DE, PSO, and TLBO techniques, to obtain the optimal geometric and flow parameters parametric selection for two SAHs having different patterns of dimples such as (i) dimples in a zig-zag pattern, and (ii) dimples in a straight-line pattern in absorber plate. To perform the optimization process, a MATLAB code is developed based on the mathematical model of FA, DE, PSO, and TLBO as discussed in chapter 1. The MATLAB code of respective algorithms is run on MATLAB software version-R2011a, which was installed in a PC having a 32-bit operating system, 2.30 GHz processor, and 4.00 GB RAM. The empirical correlations developed by Bhusan et al. [37] and Saini and Verma [31] have been considered as example 1 and example 2. Maximization of Nu and minimization of F_f were two objective functions in both examples and optimization methodology was executed as per the upper and lower range of parameters. The application of these four algorithms involves the setting of dissimilar algorithmic processes. The total iterations and number of search agents were considered as 100 and 200, respectively.

3.3 Example 1-Dimples in a Zig-Zag Pattern

To analyze and optimize the performance of SAH having spherical dimples as roughness geometry provided in a zig-zag pattern, experimental results of Bhusan et al. [37] have been selected in example 1. For the solar heat collector, a rectangular duct was used with an internal cross-section of 0.30m×0.03m and length of 2.4m and entry, test, and exit sections of 0.9m, 1m, and 0.5m, respectively, and a thickness of 12 mm. The mean hydraulic diameter (D) of the rectangular duct was 0.054m. For smooth entry and exit of air, the minimum length of entry and exit section is $5\sqrt{wH}$ and $2.5\sqrt{wH}$ as recommended by ASHRAE standard [76]. For the absorber plate, a galvanized iron sheet of size 2400mm×335mm was used. A pictorial view of the absorber plate with dimples formed in a zig-zag pattern is provided in Figure 3.1. The duct was insulated using glass wool to minimize heat loss. An electric heater provided heat flux. Air is forced into the duct using a suction blower. Ranges of various systems and operating parameters of experimentation are provided in Table 3.1. To study the influence of artificial roughened dimpled absorber plates on heat transfer characteristics and friction in the duct, Bhusan et al. [37] examined the effect of various systems and operating parameters on *Nu* and F_f. Of the two, *Nu* is of higher-the-better quality characteristics in which higher values are desired. On the other hand, the friction factor is off the lower-the-better type in which lower values are preferred. The functional correlation for the Nusselt number and friction factor is given as follows:

Table 3.1 : Geometric and flow parameters for example 1.

Sl. No.	Parameter	Range
1	Reynolds number (*Re*)	4000–20,000
2	Relative lateral pitch (P_S/e)	18.75–37.50
3	Relative longitudinal pitch (P_L/e)	25.00–37.50
4	Relative print diameter (d/D)	0.147–0.367
5	Relative roughness height (e/D)	0.03

$$Nu = f_1(Re, P_S/e, P_L/e, d/D) \tag{3.1}$$

$$F_f = f_2\,(Re, P_S/e, P_L/e, d/D) \tag{3.2}$$

where *Re* is the Reynolds number, P_S/e is relative lateral pitch, P_L/e is relative longitudinal pitch, and d/D is the relative print diameter.

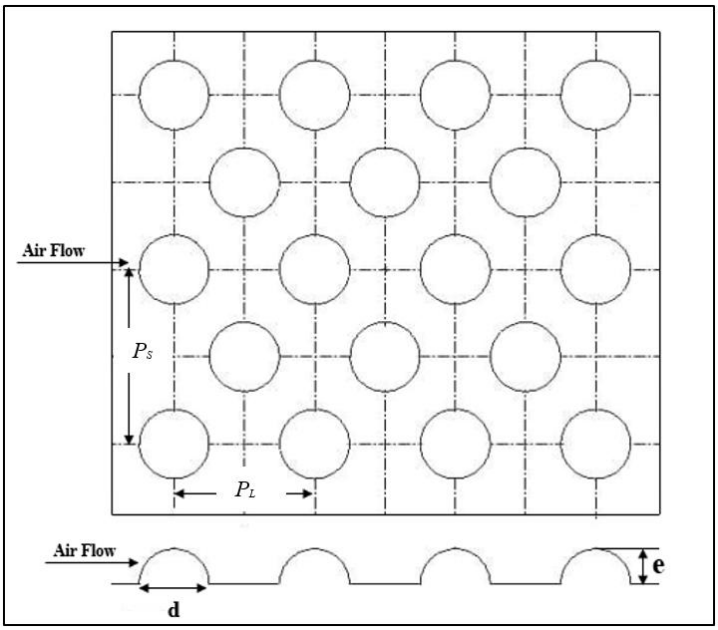

Figure 3.1 : Layout of dimpled surface for example 1.

Based on a series of experiments, Bhusan et al. [37] developed the correlation equations for *Nu* and F_f with various geometric and flow parameters as given in Eqs. (3.3) and (3.4), respectively.

$$Y(Nu) = 2.1\times10^{-88}\times \mathrm{Re}^{1.452}\times(P_S/e)^{12.94}\times(P_L/e)^{99.2}\times(d/D)^{-3.9}\times\exp[(-10.4)\{\log(P_S/e)\}^2]$$
$$\times\exp[(-77.2)\{\log(P_L/e)\}^2]\times\exp[(-7.83)\{\log(d/D)\}^2] \quad (3.3)$$

$$Y(F_f) = 2.32\times \mathrm{Re}^{-0.201}\times(P_S/e)^{-0.383}\times(P_L/e)^{-0.484}\times(d/D)^{0.133} \quad (3.4)$$

3.3.i Single-objective optimization

The developed correlation equations for *Nu* and F_f *as* presented in Eqs.(3.3) and (3.4) respectively, are solved using the metaheuristic algorithms for single-objective optimization. The objective is to maximize *Nu* and minimize F_f corresponding to the control parameter. These equations are solved considering the set of constraints as $4000\leq Re\leq 20000$, $18.75\leq P_S/e\leq 37.50$, $25\leq P_L/e\leq 37.50$, and $0.147\leq d/D\leq 0.367$. The results obtained using the considered metaheuristic algorithms for single-objective optimization are given in Table 3.2, and it revealed that the *Nu* identified by TLBO is maximum that is higher by 7.54%, 0.27%, and 0.34% as determined by FA, DE, and PSO, respectively. Similarly, for F_f, TLBO provides a minimum value of less than 11.06%, 2.24%, and 6.64% compared to FA, DE, and PSO, respectively. Further, to show the efficacy of each of these optimization algorithms, the convergence diagram is shown in Figure 3.2. The

convergence diagram represents the output of algorithm in each iteration until it converges toward a best optimal solution. It shows that the TLBO algorithm can attain the optimal result with less computational effort in terms of both time and speed. On the other hand, the corresponding box plots presented in Figure 3.3, developed for the considered metaheuristic algorithms, also show that the TLBO algorithm generates more steady optimal solutions with minimum variability compared to others. Hence, it is concluded that the TLBO algorithm outperforms FA, DE, and PSO in identifying better values of *Nu* and F_f with higher accuracy.

Table 3.2 : Results of single-objective optimization for Example1.

Response	Method	Optimal output	Operating parameter			
			Re	P_S/e	P_I/e	*d/D*
Nu	TLBO	214.2550	20000	27.0691	30.1565	0.2670
	FA	199.2344	19336	28.1511	31.1753	0.2823
	DE	213.6643	20000	26.2012	30.3613	0.2663
	PSO	213.5242	19997	28.1098	30.1926	0.2714
F_f	TLBO	0.010606	20000	37.5000	37.5000	0.1470
	FA	0.011925	18109	33.2209	34.2640	0.1552
	DE	0.010849	19998	36.5119	37.4982	0.1613
	PSO	0.011361	19948	33.9813	35.2090	0.1470

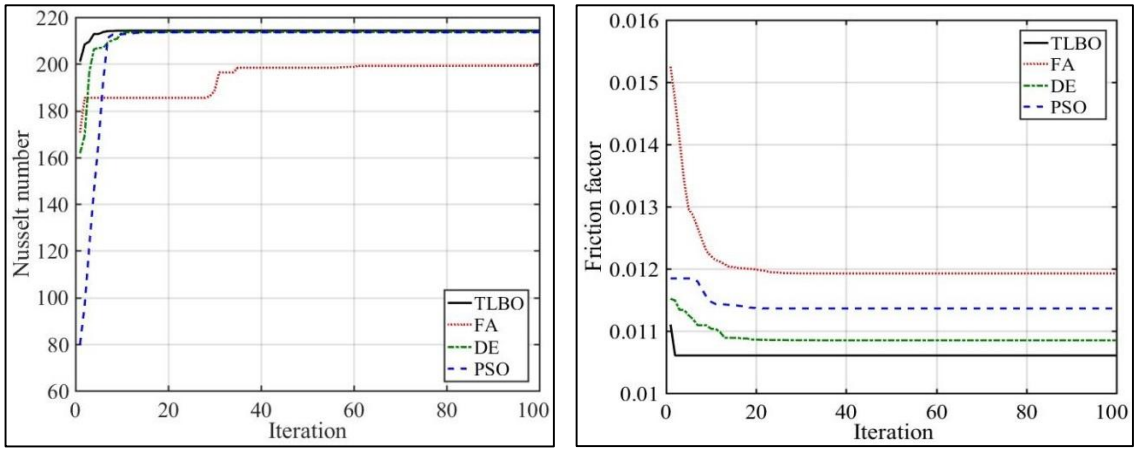

(a) Convergence diagram for *Nu* (b)Convergence diagram for F_f

Figure 3.2 : Convergence diagram for the metaheuristic algorithms for example 1.

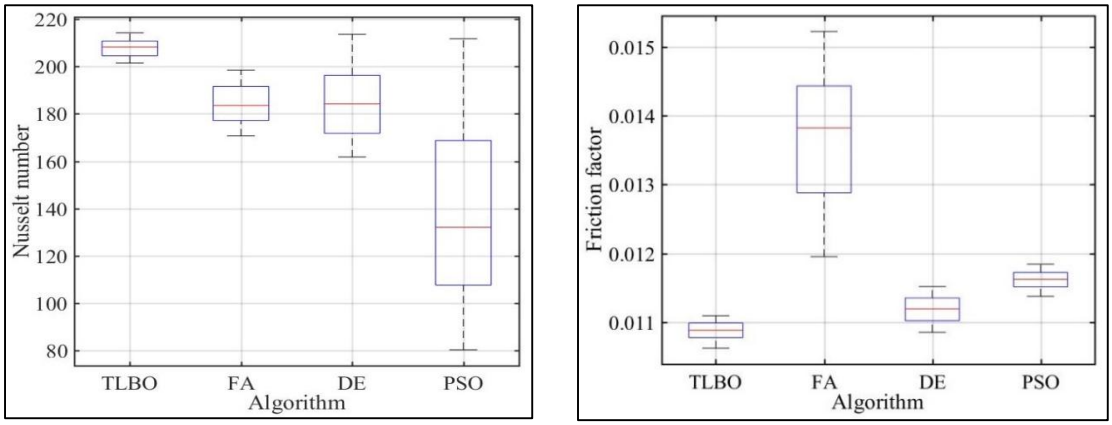

(a) Box plot for *Nu* (b) Box plot for F_f

Figure 3.3 : Box plot for the metaheuristic algorithms for example 1.

3.3.ii Multi-objective optimization

The parametric combinations obtained are different for single-objective optimization based on the applications of four metaheuristic algorithms for maximizing and minimizing F_f. However, in actual practice, it is impossible to consider different parametric combinations simultaneously to achieve better values of *Nu* and F_f. Thus, it is required to identify a unique combination of operating parameters to optimize both *Nu* and F_f simultaneously. Hence, a multi-objective mathematical model is developed as given below, considering both *Nu* and F_f, and it is further solved using the four considered metaheuristic algorithms. The multi-objective function, Z, is expressed as:

$$Minimize \quad Z = \frac{w_1 Y(Nu)}{Nu_{\max}} + \frac{w_2 Y(F_f)}{F_{f\min}} \tag{3.5}$$

where w_1 and w_2 are the weights allotted to *Nu* and F_f, respectively, $Nu_{\max}$ and F_{fmin} are the maximum and minimum values of *Nu* and F_f, respectively. Equal weights are considered for both *Nu* and F_f. These weights are allotted to fulfil the condition $w_1 + w_2 = 1$. The results obtained by solving this multi-objective optimization problem using the four considered metaheuristic algorithms are provided in Table 3.3. From the table, it is observed that TLBO exhibits a higher value of *Nu* by 3.61%, 3.26%, and 1.84% and a lower value of F_f by 1.47%, 1.47%, and 2.89% as compared to FA, DE, and PSO respectively. The TLBO algorithm again outperforms the other three considered algorithms in identifying better values of *Nu* and F_f concerning its consistency and accuracy. Hence, to enhance the quality of heat transfer and to decrease the friction resistance of the considered dimples as roughness geometry, it is recommended to operate the SAH with operating parameters as $Re = 20000$, $P_S/e = 30.83$, $P_L/e = 30.83$, and $d/D = 0.2515$. Thus, based on the results

obtained using the TLBO algorithm, it can be concluded that a higher value of *Re* and a moderate value of P_S/e, P_L/e, and d/D will produce optimum values of *Nu* and F_f subsequently enhancing the performance of considered SAH.

Table 3.3 : Results of multi-objective optimization for example 1.

Method	Response	Mean	SD	Optimal output	Z	Parameters			
						Re	P_S/e	P_L/e	*d/D*
TLBO	*Nu* F_f	0.15943	0.000609	204.7034 0.0134	0.1590	20000	30.83	30.83	0.2515
FA	*Nu* F_f	0.195468	0.0032	197.5778 0.0136	0.1797	19584	31.69	30.49	0.2659
DE	*Nu* F_f	0.173995	0.010233	198.2276 0.0136	0.1643	19997	31.04	31.69	0.2520
PSO	*Nu* F_f	0.199292	0.016417	201.0119 0.0138	0.1620	20000	30.86	30.83	0.2357

3.3.iii Hypothesis Testing: *t*-test

To evaluate the statistical significance of results obtained from different algorithms, Hypothesis testing is required. To perform hypothesis testing, the t-test method is used due to its capability to produce a more accurate confidence interval for a small size [77]. This statistical technique assesses whether the mean difference between two populations is equal to zero. It offers a hypothesis test for evaluating the disparity between the means of two sample sets under the assumption that their variances follow a normal distribution.

To assess the outstanding efficacy of the TLBO algorithm and to discern any notable disparities in the optimization capabilities among the examined metaheuristic algorithms, a paired t-test was performed based on the following hypotheses: Null hypothesis (h_n) ($m_1=m_2$, equal population means) and Alternate hypothesis ($h\alpha$) ($m_1 \neq m_2$, unequal population means). For paired *t*-test, the population means in the hypothesis indicates the average value of responses derived after 100 iterations for each algorithm. The t-test result is provided in Table 3.4. The null hypotheses are rejected as the absolute values of all responses are more significant than the critical *t*-test value of 0.05. The t-test results justify the exceptionality of the TLBO algorithm over other considered algorithms in finding the best single and multi-objective optimization solutions.

Table 3.4 : Outcomes of t-test .

Optimization	Response	FA	DE	PSO
Single-objective	*Nu*	32.56	3.15	2.66
	F_f	-29.95	-499.22	-186.35
Multi-objective	Z	-23.69	-8.48	-3.39

3.3.iv Results and Discussion

Based on the derived optimal solutions identified by the TLBO algorithm and to understand the effect of different operating parameters, the corresponding response graphs are developed for *Nu* and F_f, as provided in Figure 3.4 and Figure 3.5. Figure 3.4 (a) shows that the *Nu* rapidly increases with an increase in *Re*. The convective heat transfer coefficient increases with an increase in *Re*. This may be due to the deceleration of flow and the development of an adverse pressure gradient, further promoting instability, eddy formation, and flow separation near the protruded surface, leading to considerable energy dissipation. It is observed from Figure 3.4 (b) that *Nu* initially increases and then decreases with an increase in S/e, as a smaller value of may create a hurdle in vortice formation, hence reducing the heat transfer coefficient.

On the other hand, if the value of P_S/e is increased after a specific limit, it may be unable to disrupt the laminar sub-layer, which limits the development of eddies and results in a reduced heat transfer coefficient. Figure 3.4 (c) shows that *Nu* initially increases with an increase in P_L/e and later decreases. This may be due to the flow separation at the leading edge of dimples and reattachments of the free shear layer between the consecutive dimples in the flow direction. The maximum value of *Nu* is obtained at the region of reattachments of the free shear layer. As seen from Figure 3.4 (d), *Nu* increases rapidly with an increase in *d/D* and then gradually decreases with higher values of *d/D*. The effect of change in *d/D* on *Nu* follows the same trend observed for P_S/e and P_L/e. Effective P_S/e and P_L/e increase with a smaller value of *d/D* that is insufficient to disrupt the laminar sub-layer. On the other hand, with higher *d/D*, the generation of vortices becomes ineffective, decreasing the *Nu*.

From Figure 3.5 (a), it is observed that F_f decreases monotonously with the increase in *Re*. This may be due to generating a fully developed turbulent flow, suppressing the laminar sub-layer formed along the flow direction. As seen in Figure 3.5 (b) and Figure 3.5(c), F_f decreases with an increase in P_S/e and P_L/e. The total number of dimples on the absorber plate decreases with a higher value of P_S/e and P_L/e. This causes a reduction in F_f.

On the other hand, F_f is minimal, with a lower value of *d/D*. An increase in *d/D* increases the diameter of dimples, causing an increase in F_f.

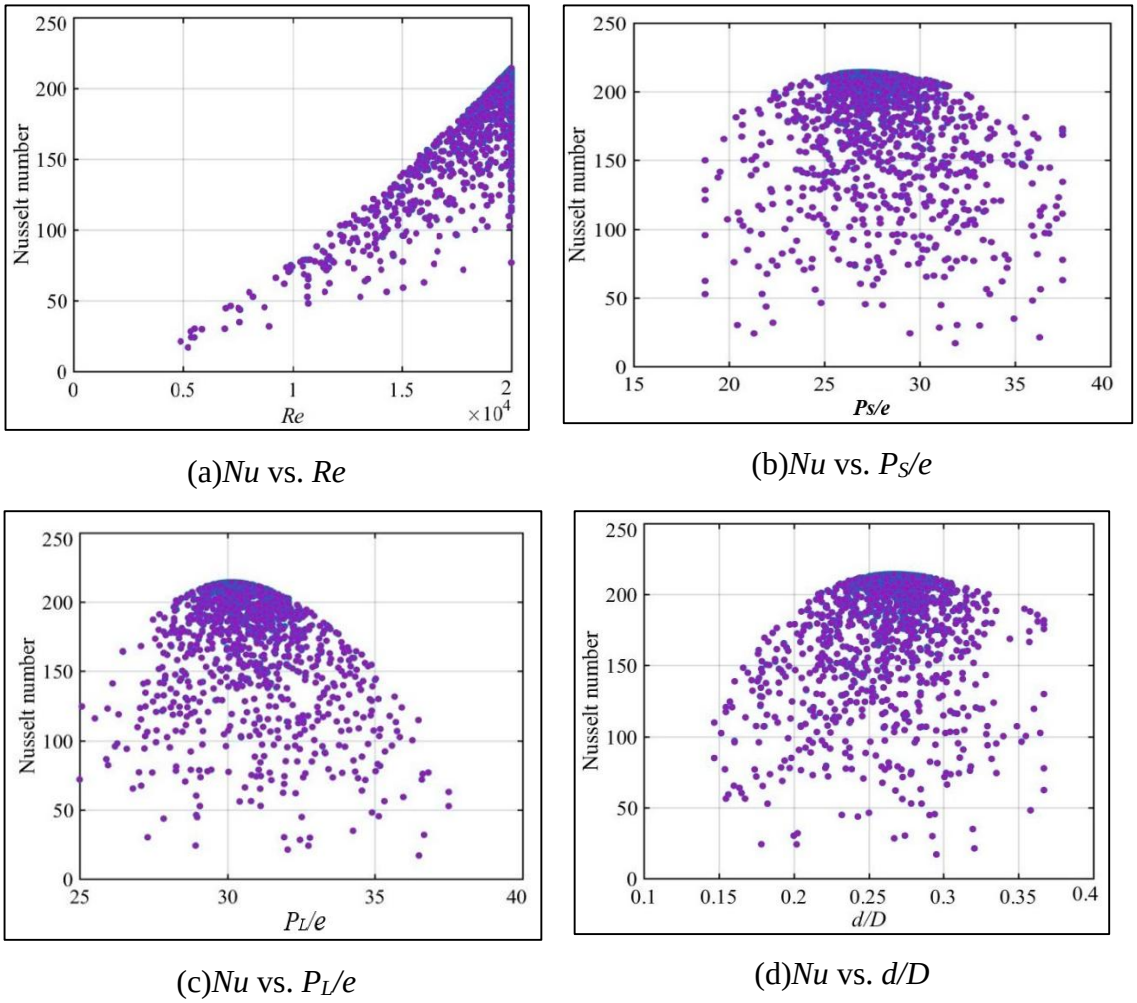

(a)*Nu* vs. *Re* (b)*Nu* vs. P_S/e

(c)*Nu* vs. P_L/e (d)*Nu* vs. *d/D*

Figure 3.4: Variations of Nusselt number to different operating parameters for example 1

3.4 Example 2- Dimples in a straight-line pattern

To examine the impact of artificial roughness, Saini and Verma [31] conducted a series of experiments in SAH having spherical dimples as roughness geometry formed in a straight-line pattern. The presented SAH contains inlet, test, and outlet section having length of 0.9m, 1m, and 0.5m, respectively. The inner cross-section of the duct was made with wooden panels having dimensions of 2400mm×300mm×25mm. For smooth entry and exit of air, the least length of entry and exit section is $5\sqrt{wH}$, and $2.5\sqrt{wH}$ respectively as recommended by ASHRAE standard [76]. A schematic diagram of the absorber plate with dimples in a straight-line pattern is shown in Figure 3.6. An electric heater was used to supply the heat source of 0-1000 W/m^2 using a variac connected throughout its length. The duct was insulated by glass wool. The absorber plate with dimple was made of galvanized iron sheet and placed at the top of the test section. A centrifugal air suction blower forces

the air through the duct. Various operating parameters such as temperature, the mass flow of air, and pressure drop across the test section were measured using a thermocouple, orifice meter, and micro-manometer, respectively. Various geometric and flow parameters, along with their range considered during the conduction of experiments, are provided in Table 3.5. Based on the experimental results [31], two correlation equations relating Nu and F_f with various geometric and flow parameters were developed.

$$Y(Nu) = 5.2\times10^{-4}\times \mathrm{Re}^{1.27}\times(e/D)^{0.033}\times(P/e)^{3.15}\times\exp[(-2.12)\{\log(P/e)\}^2] \times\exp[(-1.30)\{\log(e/D)\}^2] \quad (3.6)$$

$$Y(F_f) = 0.642\times \mathrm{Re}^{-0.423}\times(e/D)^{-0.0.214}\times(P/e)^{-0.465}\times\exp[(0.054)\{\log(P/e)\}^2] \times\exp[(0.840)\{\log(e/D)\}^2] \quad (3.7)$$

where p/e is the relative pitch length, and e/D is the relative roughness height.

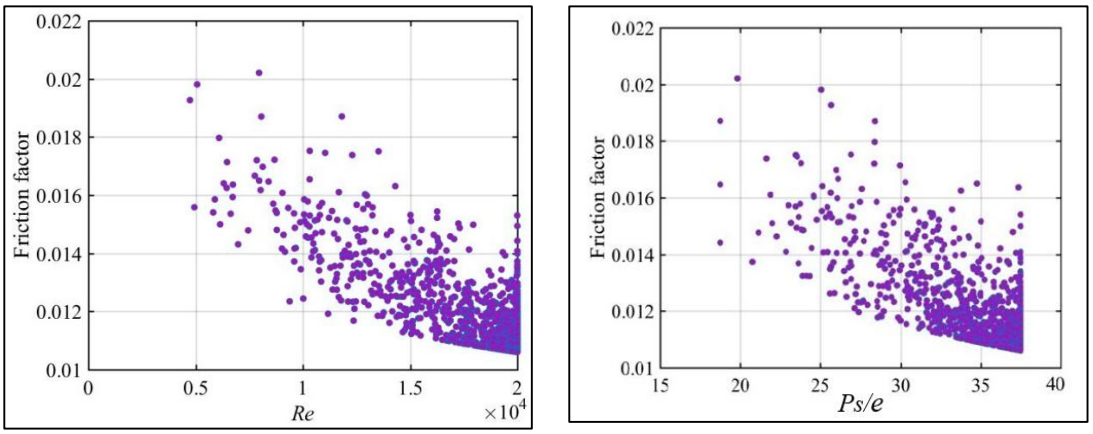

(a)F_f vs. *Re* (b)F_f vs. P_S/e

(c)F_f vs. P_L/e (d)F_f vs. *d/D*

Figure 3.5:Variations of friction factor to different operating parameters for example 1.

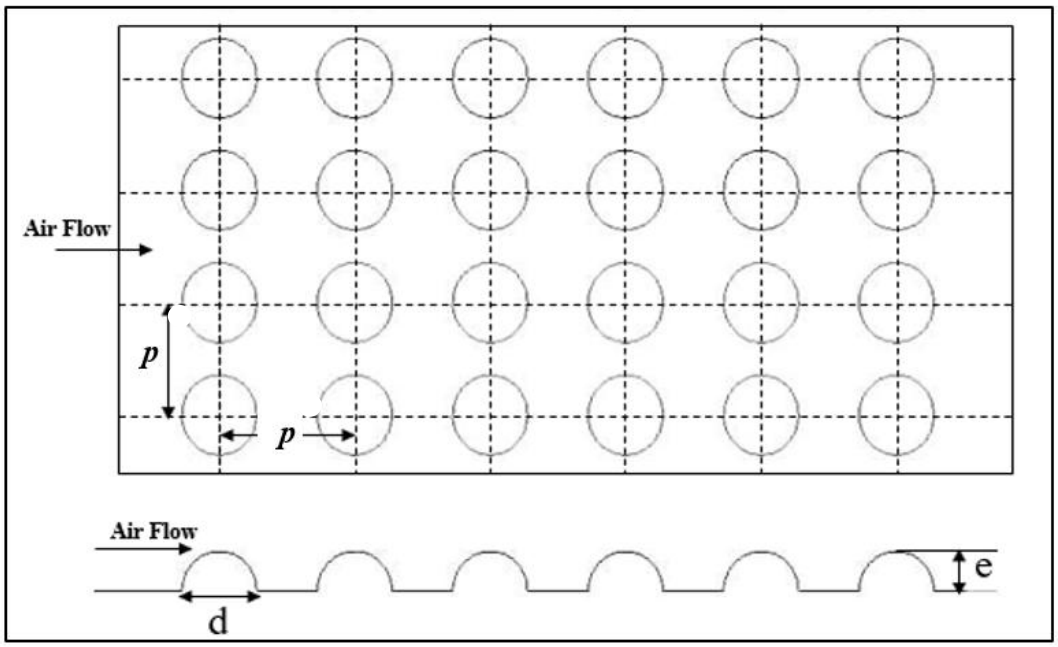

Figure 3.6: Layout of dimpled surface for example 2.

Table 3.5: Geometric and flow parameters for example 2.

Sl. no.	Parameter	Range
1	Reynolds number *(Re)*	2000-12000
2	Relative pitch length (*p/e*)	8-12
3	Relative roughness height (*e/D*)	0.0189-0.0379

3.4.i Single-objective optimization

As done for the previous case, four metaheuristic algorithms, i.e., FA, DE, PSO, and TLBO algorithms, are employed for obtaining the optimal geometric and flow parameters parametric values of the considered SAH. Various algorithmic parameters associated with these algorithms are set similarly to the previous case, with the objective being the maximization of *Nu* and the minimization of F_f—the developed correlation equations, i.e., Eqs. (3.6) and (3.7) for *Nu* and F_f respectively are first solved as single-objective optimization using four metaheuristic algorithms. The equations are solved by taking into consideration various constraints such as $12000 \geq Re \geq 2000$, $12 \geq p/e \geq 8$, and $0.0189 \geq e/D \geq 0.0379$. The computational results obtained employing the optimization techniques are presented in Table 3.6. From the table, it is observed that TLBO unveils a higher value of *Nu* by 1.30%, 1.84%, and 16.81% and a lower value of F_f by 15.65%, 3.26%, and 6.32% compared to FA, DE, and PSO, respectively. The results reveal that the TLBO algorithm again surpasses other optimization techniques concerning the consistency and accuracy of the obtained optimal solutions. This can also be confirmed by the

developed convergence diagrams and the corresponding box plots, as shown in Figure 3.7 and Figure 3.8, respectively.

Table 3.6 : Results of single-objective optimization for example 2.

Response	Method	Optimal output	Operating parameter		
			Re	*p/e*	*e/D*
Nu	TLBO	107.7515	12000	12	0.0377
	FA	106.3682	11798	12	0.0379
	DE	105.8025	11944	11.7867	0.0379
	PSO	92.1855	12000	10.8224	0.0370
F_f	TLBO	0.0237	11976	12	0.0379
	FA	0.0281	8008.8	12	0.0379
	DE	0.0245	11211	11.9734	0.0378
	PSO	0.0253	11999	10.2341	0.0379

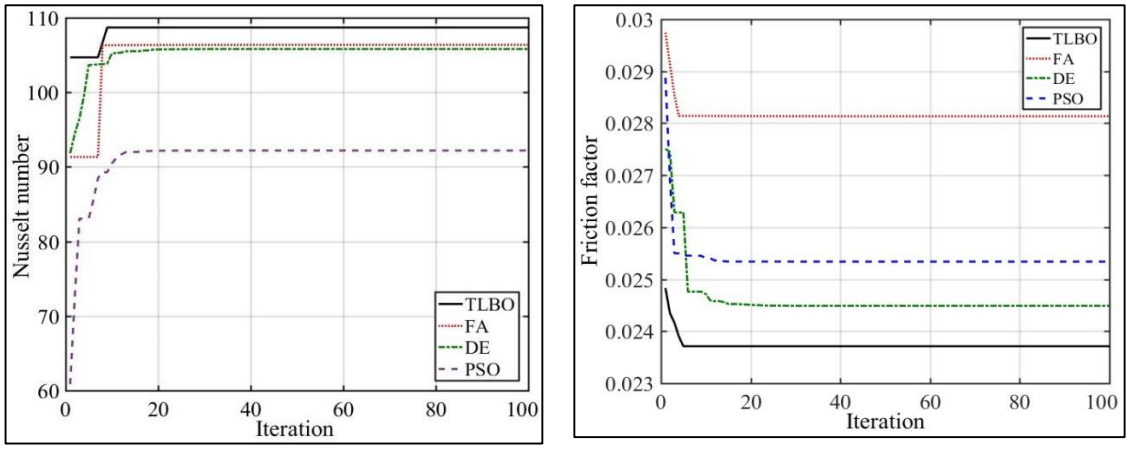

(a) (b)

Figure 3.7 :Convergence diagram for the metaheuristic algorithms for example 2.

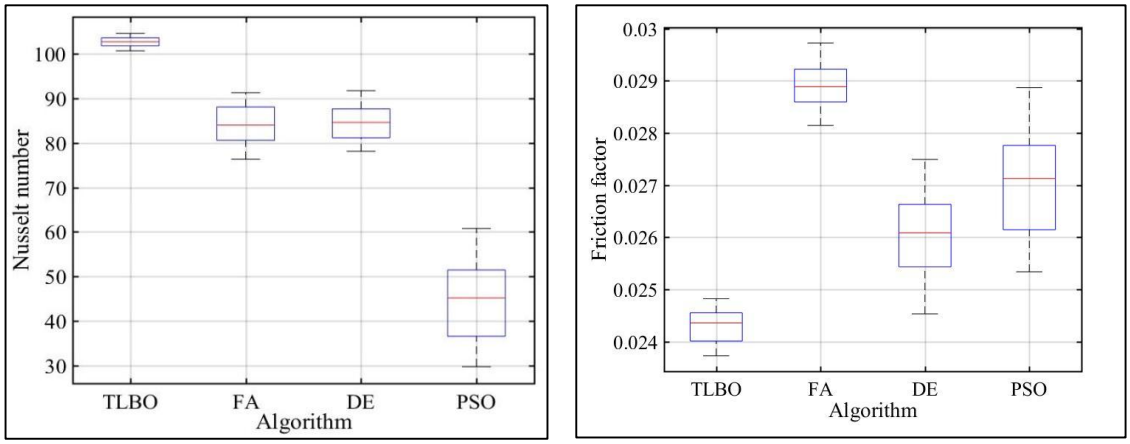

(a) (b)

Figure 3.8 : Box plot for the metaheuristic algorithms for example 2.

3.4.ii Multi-objective optimization

It understands that in actual practice, it is impossible to consider different parametric combinations simultaneously to achieve better values of *Nu* and F_f. Hence, similar to Eq. (3.5), a multi-objective mathematical model is developed to identify a unique blend of operating parameters to optimize both Nu and F_f concurrently. The developed multi-objective mathematical model is further solved using the four-mentioned metaheuristic algorithms; the results are presented in This demonstrates the superiority of the TLBO algorithm compared to various other algorithms in achieving optimal solutions for both single-objective and multi-objective optimization problems.

Table 3.7 reveals that the value of *Nu* generated by TLBO is maximum and is higher by 0.68%, 0.084%, and 0.61% as generated by FA, DE, and PSO, respectively. Similarly, for F_f, TLBO provides the minimum value, which is less by 1.65%, 0.42%, and 1.65% compared to FA, DE, and PSO, respectively. As witnessed in the previous case, in this case, the optimization performance of the TLBO algorithm is seen to have better values of *Nu* and F_f compared to those identified by the other considered optimization techniques. Thus, to obtain optimal performance of considered SAH, it is recommended to set the operating parameters as Re = 12000, p/e= 12, and e/D = 0.0379 with the values for *Nu* and F_f obtained as108.6901 and 0.0237 respectively. The two-tailed paired *t*-test has been performed, and the outcomes are provided in Table 3.8 to evaluate the exceptional performance of the TLBO algorithm in comparison to three other algorithms. As observed in earlier examples, the null hypothesis is rejected as the absolute values of all responses generated by TLBO are greater than the *t*-test values of the other three algorithms. This demonstrates the superiority of the TLBO algorithm compared to various other algorithms in achieving optimal solutions for both single-objective and multi-objective optimization problems.

Table 3.7 :Results of multi-objective optimization for example 2.

Method	Response	Mean	SD	Optimal output	Z	Control Parameter *Re*	*p/e*	*e/D*
TLBO	Nu F_f	0.00032	0.000765	108.6901 0.0237	0.00024	12000	12	0.0379
FA	Nu F_f	0.012376	0.002961	107.9544 0.0241	0.0047	11936	12	0.0379
DE	Nu F_f	0.014358	0.041415	108.5981 0.0238	0.00074	11992	12	0.0379

PSO	Nu	0.014358	0.041415	108.0244	0.0033	12000	11.98	0.0378
	F_f			0.0241				

Table 3.8: The outcomes of the paired t-test related to the TLBO algorithm for Example 2.

Optimization	Response	FA	DE	PSO
Single-objective	*Nu*	10.83	-24.7	52.95
	F_f	-42.06	-12.7	-20.12
Multi-objective	Z	-87.94	-1.98	-4.29

3.4.iii Results and Discussion

The corresponding response graphs are developed, as given in Figure 3.9 and Figure 3.10, to examine the effects of considered operating parameters on Nu and F_f. Figure 3.9 (a) illustrates that Nu increases with an increase in Re. This is due to the breakage of the laminar sub-layer significant at high-value Re, as already discussed in the previous example. Figure 3.9 (b) shows that Nu increases with an increase in p/e. The re-attachment of the free shear layer after separation at dimples increases with an increase in p/e, resulting in Nu increases. From Figure 3.9 (c), a similar behavior is noticed for Nu as it grows with an increase in e/D. As discussed in the earlier example, F_f decreases monotonously with an increase in Re due to generating a fully developed turbulent flow that suppresses the laminar sub-layer formed along the flow direction, as seen in Figure 3.10 (a). Similarly, as observed in Figure 3.10 (b), an increase in p/e and e/D increases the pitch between dimples resulting in a decrease of F_f. On the other hand, F_f is minimal, with a lower value of e/D. An increase in e/D increases the height of dimples, causing an increase in F_f as shown in Figure 3.10 (c).

3.5 Performance Comparison

A comparative performance analysis of different metaheuristic algorithms is presented in

Table **3.9**. It can be seen that the TLBO algorithms had shown better performance than PSO, Genetic Algorithms (GA), and Simulated Annealing (SA) in the case of smooth flat plate and twisted rib roughened solar air heaters. Also, in the present study, the human-inspired based TLBO metaheuristic algorithm also outperforms over Bio-inspired (i.e. FA), evolution-inspired (i.e. DE), and swarm-intelligence-inspired (i.e. PSO) based metaheuristic algorithms. The efficacy of TLBO have been validated from convergence

plot, box plot and t-test. The faster convergence with less computational effort and more consistent optimal solutions with minimum variability were obtained due to its capability to handle parametric constraint free structure and balanced approach to exploration and exploitation. So, the TLBO algorithms can be an effective optimization tool to deal with the optimization problems of SAH.

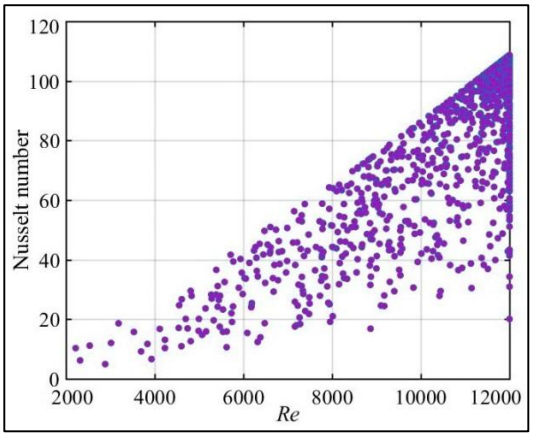

(a) *Nu* vs. *Re*

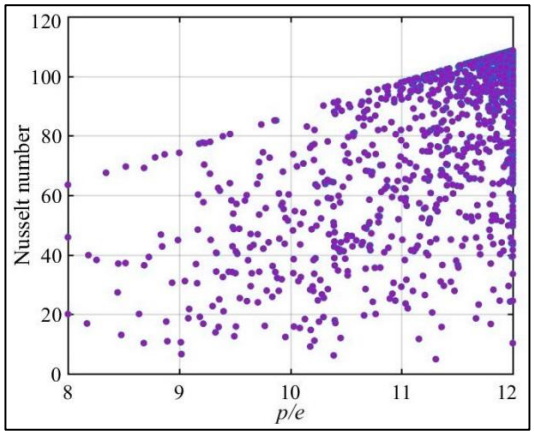

(b) *Nu* vs. *p/e*

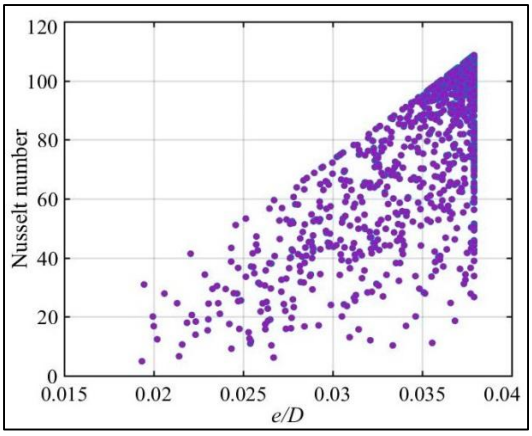

(c) *Nu* vs. *e/D*

Figure 3.9: Variations of Nusselt number with respect to different operating parameters for example 2.

3.6 Conclusions

An extensive investigation of single and multi-objective optimization of the geometric and flow parameters of SAH with spherical-shaped dimples as roughness on absorber plates using four different metaheuristics algorithms such as FA, DE, PSO, and TLBO has been presented in this paper. The geometric and flow parameters are optimized for the global solution, and their performance is compared. The following conclusions are drawn from this chapter.

i. In single objective optimization of solar air heater having dimples in a zig-zag pattern, the TLBO metaheuristics algorithm exhibited better results than the other three algorithms. The maximum value of Nu was obtained to be 214.2550 concerning Re=20000, P_S/e =27.0691, P_L/e =30.1565, and d/D=0.2670, and the minimum value of F_f was obtained to be 0.010606 at Re=20000, P_S/e=37.50, P_L/e =37.50, and d/D=0.1470. In multi-objective optimization, the suitable geometric and flow parameters parameter were found to be Re = 20000, P_S/e= 30.83, P_L/e = 30.83, and d/D = 0.2515 for the optimal value of Nu and F_f of 204.7034 and 0.0134 respectively.

ii. In single objective optimization of solar air heater having dimples in straight-line pattern, the TLBO metaheuristics algorithm demonstrated better results than the other three algorithms. The maximum value of Nu was obtained to be 107.7515 at Re=20000, p/e =12, e/D =0.0377, and the minimum value of F_f was obtained to be 0.0237 at Re=11976, p/e =12, e/D =0.0379. In multi-objective optimization, the suitable geometric and flow parameters were Re = 12000, p/e= 12, and e/D = 0.0379 for the optimal values for Nu and F_f as108.6901 and 0.0237 respectively.

iii. The TLBO metaheuristics algorithm outperformed the other three metaheuristics algorithms in terms of accuracy with low variability and minimal computational effort, as observed from the t-test and convergent diagram.

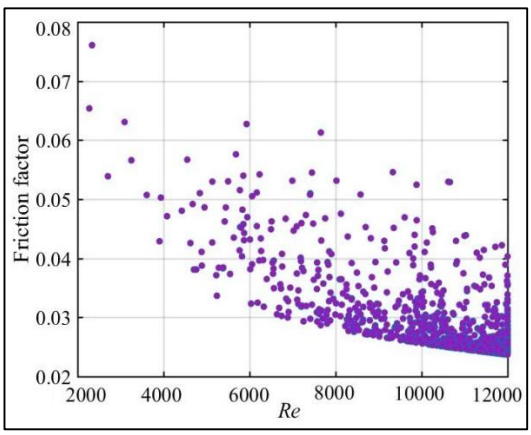

(a) F_f vs. Re

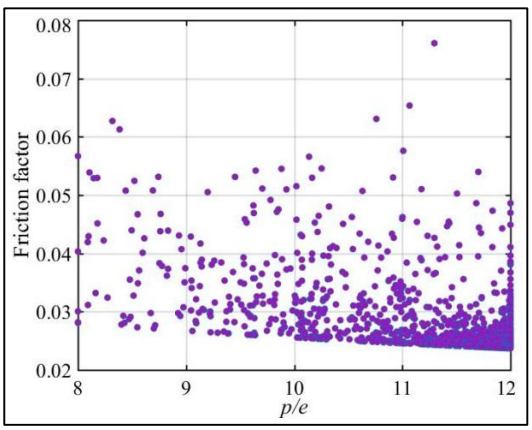

(b) F_f vs. p/e

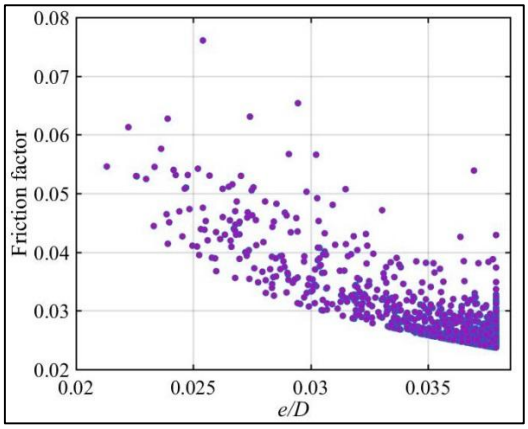

(c) F_f vs. e/D

Figure 3.10 :Variations of friction factor to different operating parameters for example 2.

Table 3.9 : Comparisons of different studies.

Authors	Type of Absorber plate	Metaheuristic algorithm(s)	Optimal Geometric and flow parameters	Best Results delivered by
Rao[78]	smooth flat plate	TLBO, GA, PSO, SA ETLBO	Re=20,000 α=59.5832º I=600W/m^2	TLBO and ETLBO algorithms
Rao and Waghmare [79]	smooth flat plate	GA, SA, PSO, TLBO	Re=20,000 α=59.5832º I=600W/m^2	TLBO algorithm
Kumar and Layek [68]	twisted rib roughness	PSO and TLBO	Re=21,000 p/e=8 α=60º y/e=3	TLBO algorithm
Present Study	Dimples in a zig-zag pattern	FA, DE PSO, TLBO	Re=20,000 P_S/e =30.83 P_L/e =30.83 d/D=0.2515 e/D=0.03	TLBO algorithm
	Dimples in a straight line pattern	FA, DE PSO, TLBO	Re=12000 p/e=12 e/D=0.0379	TLBO algorithm

3.7 Summary

In this research work, single and multi-objective parametric optimization of solar air heaters using four metaheuristics algorithms, i.e., Firefly algorithm (FA), Particle swarm optimization (PSO), Differential evolution (DE), and Teaching learning-based

optimization (TLBO) have been investigated. The parametric optimization of two different types of artificially roughened SAHs with dimples in zig-zag and straight-line patterns was performed. The outcomes of this research work concluded that the TLBO metaheuristic algorithm can be employed as an effective optimization tool in the parametric optimization of SAH. The classical features of TLBO, like its simplicity in application, accuracy, less computational effort, and consistency in optimal results, can help to deal with high-dimension optimization problems that involve the design and development of SAH. However, premature convergence of TLBO has been noticed that my impact the global solutions. So, it is necessary to explore the feasibility of other new generation metaheuristics algorithms in optimizing the control parameters of solar air heaters having different dimples/protrusions geometry, patterns, and a range of control parameters.

CHAPTER 4

PROTRUSIONS IN V-NOTCH PATTERN

Preface

In this chapter, the performance analysis of a solar air heater having hemispherical protrusions in a V-notch pattern has been investigated experimentally. Using experimental data, a statistical correlation for the Nusselt number and friction factor is developed. Further, five metaheuristic algorithms, i.e., Ant colony optimization (ACO), Whale optimization algorithm (WOA), Grass-hopper optimization algorithm (GOA), grey wolf optimization (GWO), and Dragonfly algorithm (DA) were employed for the parametric optimization.

4.1 Introduction

In this chapter, the thermo-hydraulic performance of a new type solar air heater with single V-notch patterns of hemispherical protrusions are investigated experimentally for different relative protrusion heights (h_p/D_h = 0.027-0.069), relative pitch (p_p/h_p = 6-14), angle of attack (α_{ap}= 15º-75º), and Reynolds number (Re =3600-21700). Also, five meta-heuristic algorithms, i.e., Ant colony optimization (ACO), Whale optimization algorithm (WOA), Grass-hopper optimization algorithm (GOA), grey wolf optimization (GWO), and Dragonfly algorithm (DA) were used for single and multi-objective optimizations.

Hemispherical protrusions as artificial roughness in a single V-notch pattern with the entry of cold air from the V-apex side make this roughness unique, and it assumes that the given patterns reduce the frictional resistance at the entrance and help to develop a strong secondary flow downstream that will improve heat augmentation. Also, optimizing flow and protrusion's geometric parameters using new-generation metaheuristic optimization algorithms is necessary for suitable parametric selections for optimal output. Despite having superior performance in optimizing other engineering problems, the applications of selected Metaheuristic optimization algorithms still need to be explored in

this field. The unique searching behaviour of ants, Whales, Grass-hopper, grey wolf, and Dragonfly inspires these metaheuristic optimization algorithms. The authors presumed that the metaheuristic algorithms based on the basic principles of movement, i.e., running, crawling, swimming, and flying, can provide a good insight into the parametric optimization of solar air heaters. Thus, this research work emphasizes investigates the thermo-hydraulic performance of a new type of solar air heater with a single V-notch pattern of hemispherical protrusions on an absorber plate. Also, a comparative performance analysis of five metaheuristic algorithms, namely ACO, WOA, GOA, GWO, and DA, have been investigated.

4.2 Experimentation test rig

An experimental test rig with a V-notch pattern on the absorber plate of a solar air heater has been designed and fabricated to study the effects of hemispherical protrusion. The collector box of the solar air heater is designed as per the ASHRAE Standard 93-77 [76] standard, and the material of choice has been chosen to ease the fabrication process and easy procurement. A wooden frame is used to fabricate the collector box. The internal dimension of the duct is 330 × 30 × 2200mm. The duct has an entry section of 800mm, a test section of 1000mm, and an exit section of 400mm. The aspect ratio of the duct is 11. Figure 4.1 shows a detailed sketch of the collector. Various samples of metal sheets (e.g., G.I., tin, and aluminium sheets) were tested for the design and fabrication of the absorber plate. Finally, aluminium sheets are selected for the absorber plate because of their high malleability and heat conductivity. A total of 5 sets of punch and die have been prepared to make the protrusion/dimple of the absorber plate. An aluminium sheet 0.4mm thick, 1000 x 330 mm, was used as an absorber plate at the test section, on which the protrusions were made in a V-notch pattern with the different punch and die combinations. The geometrical dimensions of the protrusions are provided in Table 4.1. A total of 15 absorber plates are prepared considering the suitable combination of lower, middle, and upper values of geometric parameters for the experiments. Figure 4.2 shows a picture of an absorber plate with protrusion. A thick layer of glass wool has been used to provide insulation in the duct. The pictorial presentation of the actual experimental test rig and schematic diagram of the experimental test rig is provided in Figure 4.3 and Figure 4.4.

The experiment was conducted in a controlled environment at room conditions. A 3-phase, 0.5HP centrifugal blower has been used to pass the air through the collector chamber, and an artificial source of heat (Halogen Light) has been used to mimic solar

radiation. Various measuring devices have been used for data collection, such as thermocouples, Digital Micro-Manometer, Digital anemometer, and Pyranometer. Sixteen thermocouples measure the temperature at different test points. Air velocity is measured with the help of a digital anemometer, and a Pyranometer is used to measure thermal radiation. The pressure drop was measured with the help of a digital micro-manometer. The performance parameter of the solar air heater was evaluated using the different sets of geometrics and flow parameters.

Table 4.1 : Protrusion dimensions

Die/Punch set No.	Protrusion diameter (d_p), mm	Protrusion height (h_p), mm	Relative size of protrusion (h_p/d_p)
1	5	1.50	0.30
2	6.80	2.06	0.30
3	8.80	2.80	0.30
4	10.60	3.14	0.30
5	12.56	3.87	0.30

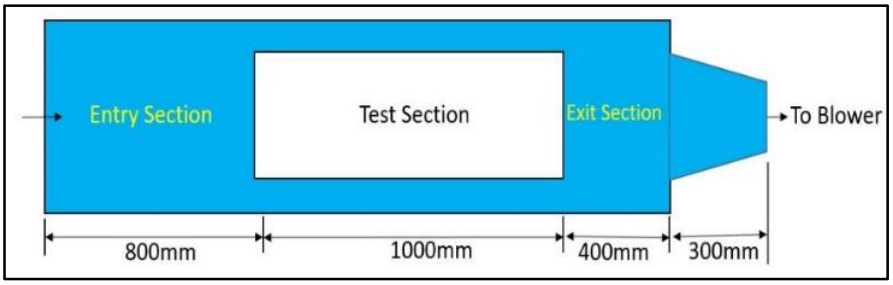

(a)

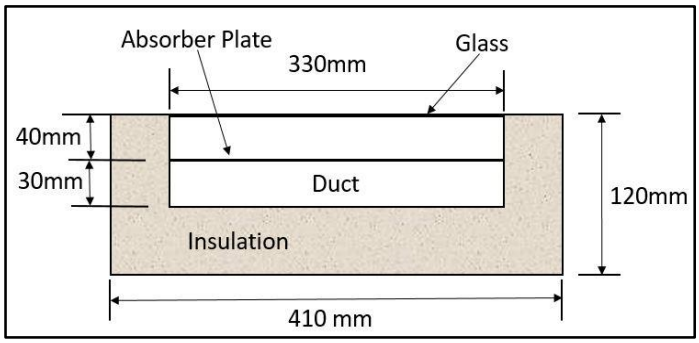

(b)

Figure 4.1: Detailed sketch of the collector: (a) Top view of the collector, and (b) Cross-section view of the collector.

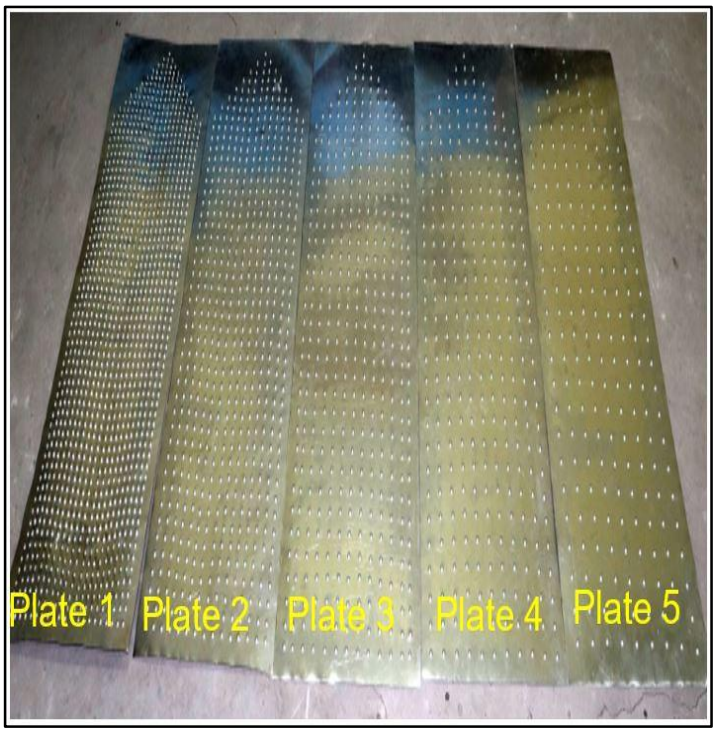

(a)

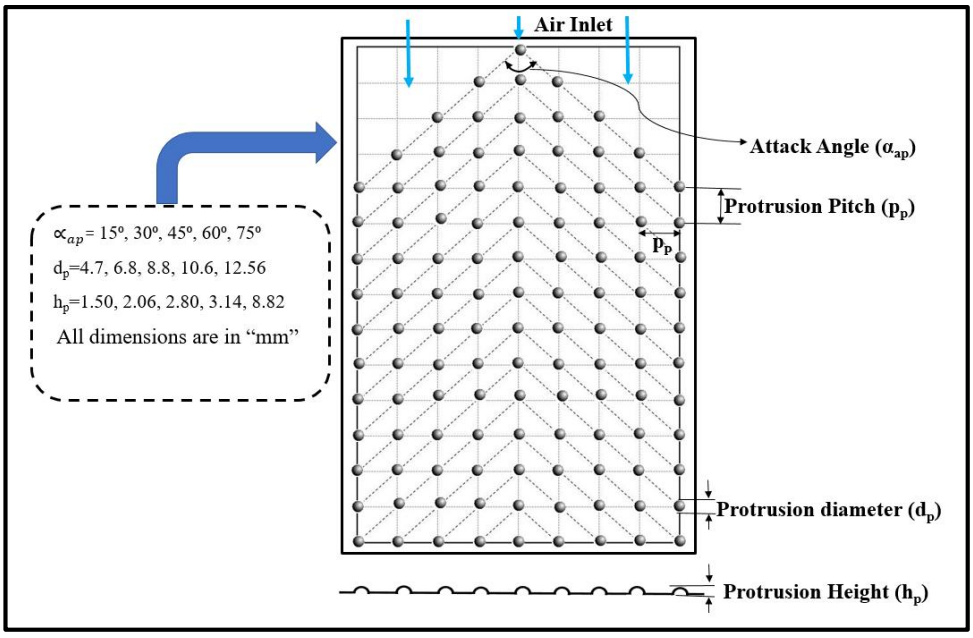

(b)

Figure 4.2: Absorber plate:- (**a**) Actual absorber plate, and (**b**) Schematic diagram of absorber plate.

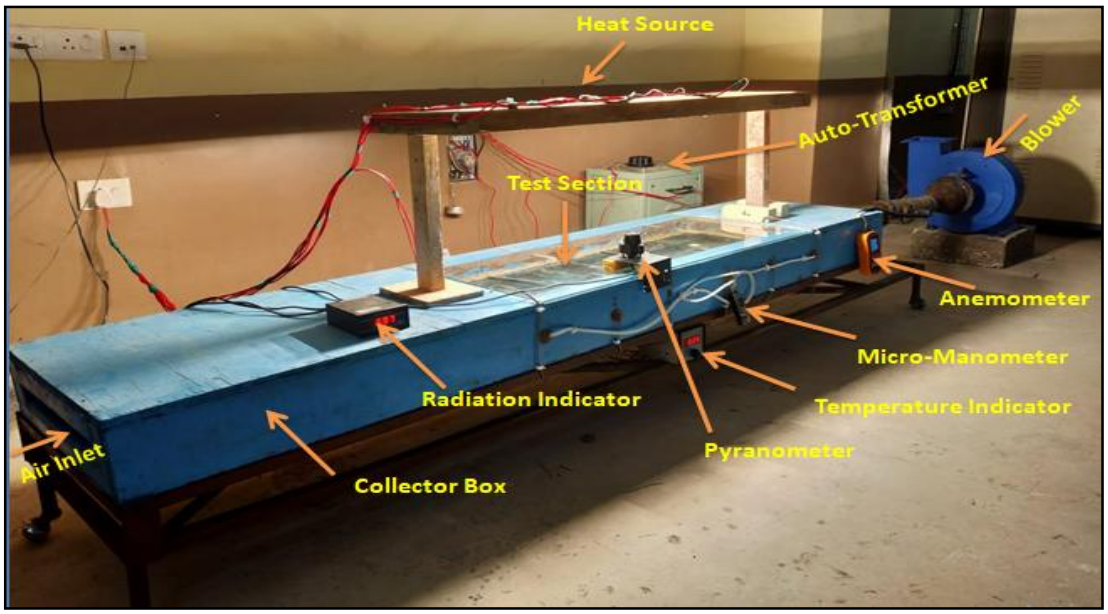

Figure 4.3 : Actual experimental test rig.

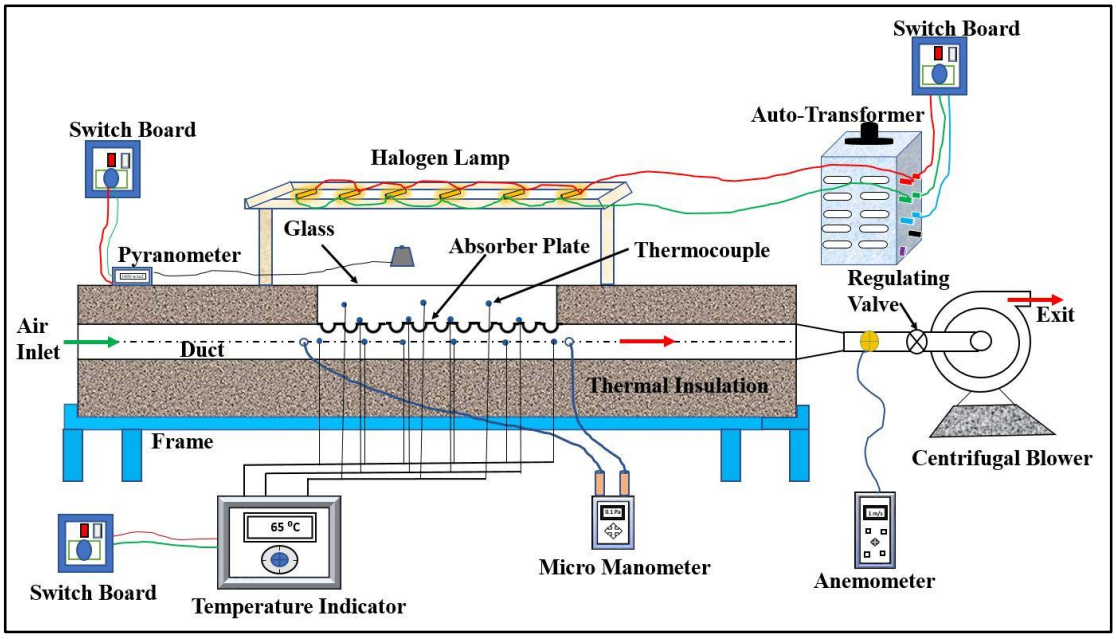

Figure 4.4 : Schematic diagram of experimental test rig.

Before experimentation, air leakage from the duct was tested using a soap solution. The proper functioning of all the instruments was calibrated and examined. Once it was found satisfactory, the power supply to the halogen lamp and the centrifugal blower were provided. A 3-phase autotransformer was used to control the power supply. The heat flux was measured using a Pyranometer, fixed to 1000W/m^2, by controlling the power supply through an autotransformer. The speed of the blower was controlled to set the mass flow of air through the duct. Also, a butterfly valve was used to control the airflow rate precisely.

Once stable airflow and heat flux were maintained, it could run until the steady state condition was reached. Then, recording data for the temperature at target points, air velocity through the duct, pressure drop across the test section, and heat flux were performed. For every alternation in airflow, the system was run to reach the steady-state condition, and then the data were recorded.

4.3 Parametric selection

Three different protrusion geometric parameters are taken into account, these are relative pitch of protrusion (p_p/h_p= 6, 8, 10, 12, and 14), relative height of protrusion (h_p/D_h= 0.027, 0.037, 0.050, 0.057, and 0.069), and protrusion angle of attack (α_{ap}=15º, 30º, 45º, 60º, and 75º), it is the angle between V legs of protrusions alignment. The flow parameter is Reynolds number (Re =3600, 7200, 10900, 14500, 18100, and 21700). The lower and upper value of the geometric and flow parameters is illustrated in Table 4.2.

Table 4.2 : Geometric and flow parameters

Sl.Nos.	Parameter	Range/Value	Type
1	Relative pitch of protrusions (p_p/h_p)	6-14	Geometric parameter
2	Relative height of protrusions (h_p/D_h)	0.027-0.069	Geometric parameter
3	Protrusion angle of attack (α_{ap})	15-75	Geometric parameter
4	Reynolds Number (Re)	3600-21700	Flow parameter

4.4 Data Reduction

Various parameters, such as temperature, velocity of air, pressure loss in test section, and irradiation, are recorded at steady-state conditions. Different thermo-physical properties of air such as density, heat capacity, viscosity, and thermal conductivity are evaluated at mean temperature of air. These data are used to calculate the heat transfer rate. Nusselt number and friction factor shall be evaluated to analyze the effect of dimple/protrusion with the variation in controlling parameters. The mass flow rate, useful heat gain, and heat transfer coefficient can be calculated using the below equations respectively [29], [39], [80]:

$$\dot{m} = \rho A_d V \tag{4.1}$$

$$Q_u = \dot{m}\, C_p (T_o - T_i) \tag{4.2}$$

$$h = \frac{Q_u}{A_p \left(T_{pm} - T_{ma}\right)} \tag{4.3}$$

where T_{pm} and T_{ma} are the mean temperature of absorber plate and air, respectively.

The Reynolds number (Re), Nusselt number (Nu) and friction factor (*f*) are calculated using Eq. (4), Eq. (5) and Eq. (6) respectively [81],[82],[34], [38], [39].

$$Re = \frac{\rho V D_h}{\mu} \tag{4.4}$$

$$Nu = \frac{hD_h}{k} \tag{4.5}$$

$$f = \frac{(\Delta P) D_h}{2\rho L V^2} \tag{4.6}$$

where D_h is the hydraulic diameter of the duct, which is calculated using Eq.(7).

$$D_h = \frac{4WH}{2(W+H)} \tag{4.7}$$

The thermo-hydraulic performance parameter (THPP) for a protruded absorber plate is computed relative to a smooth absorber plate and is calculated as [81]:

$$THPP = \frac{(Nu/Nu_S)}{(f/f_S)^{1/3}} \tag{4.8}$$

4.5 Validity test

Experimental validation has been performed by comparing the Nusselt number and friction factor values obtained using smooth absorber plates with the Dittus-Boelter and modified Blasius correlation.

$$Nu_s = 0.023\, Re^{0.8} Pr^{0.4} \quad \text{(Dittus-Boetler [83])} \tag{4.9}$$

$$f_s = = 0.085 Re^{-0.25} \quad \text{(Blasius equation [84])} \tag{4.10}$$

Figure 4.5 compares the experimental and theoretical results of the Nusselt number and friction factor. The results exhibit a good agreement between practical and theoretical results with a mean absolute deviation of around 4% and 2% for the Nusselt number and friction factor, respectively, which validates the accuracy of data collection in the experiments.

4.6 Error analysis

An error analysis is a procedure to obtain the uncertainty in the calculated values of the experimental data. Uncertainties in the observed data set may arise due to factors such as an error in specification, choice of a test device, environment condition, and accuracy in observation and reading. During the test, solar radiation, temperature, air

velocity, and pressure difference were measured with appropriate devices. The uncertainty (*Ux*) and relative error (*Ex*) are evaluated using Eqs. (4.11) and (4.12), respectively [85].

$$U_x = \left[\left(\frac{\delta x}{\partial k_1}\delta k_1\right)^2 + \left(\frac{\delta x}{\partial k_2}\delta k_2\right)^2 + \cdots + \left(\frac{\delta x}{\partial k_n}\delta k_n\right)^2\right]^{1/2} \tag{4.11}$$

$$E_x = \frac{U_x}{x} \tag{4.12}$$

The uncertainty of various measuring instruments is displayed in Table 4.1. Also, uncertainty in the measurement calculation of multiple parameters is provided in Table 4.4 and corresponding equations are given in Appendix A.

4.7 Metaheuristic optimization

Metaheuristics optimization methods have evolved at a much faster pace with the increase in the computational capability of computers. Single-based and population-based algorithms are two significant categories of metaheuristics. Single-based metaheuristic algorithms generate single solutions. On the other hand, population-based meta-heuristic algorithms generates multiple solutions. These algorithms are further divided into four types, i.e., evolutionary-based, swarm intelligence-based, event-based, and physics-based.

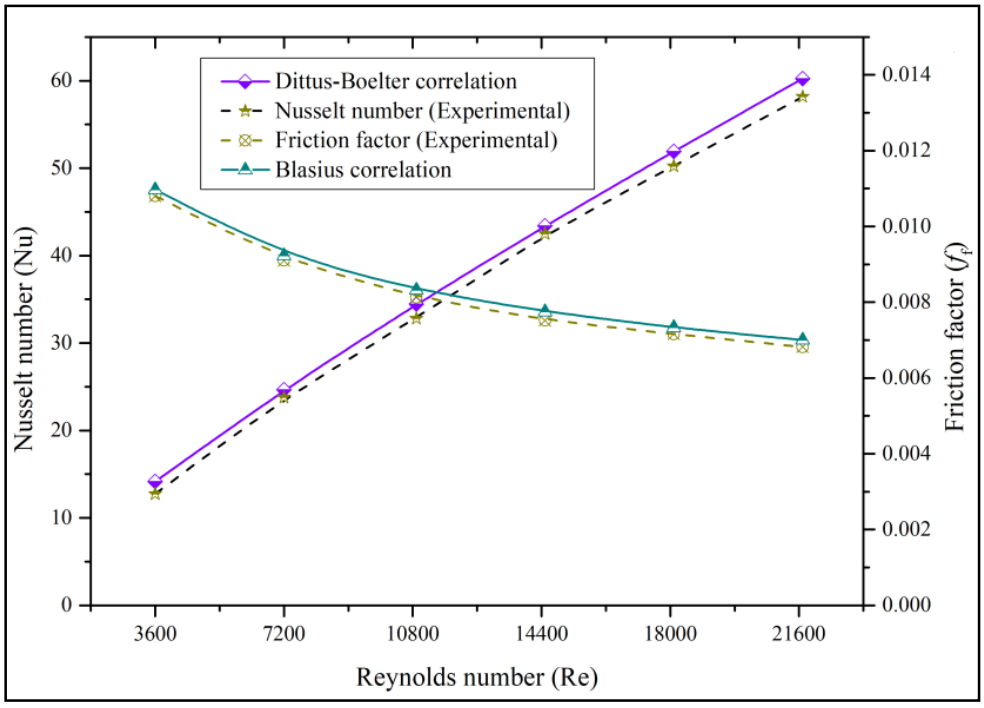

Figure 4.5: Comparison of experimental and theoretical results.

Table 4.3: Uncertainty of measuring instruments

Measurement Parameter	Instrument	Uncertainty
Geometrical Dimensions	Vernier Caliper	±0.02mm
Temperature	Thermocouple	±1ºC
Air Velocity	Anemometer	±0.1m/s
Pressure Drop	Digital Micro-Manometer	±0.1Pa
Irradiation	Pyranometer	±20W/m^2

Table 4.4 : Uncertainty of measurement of various parameters

Parameter	%Uncertainty
Cross-section area of duct(A_d)	0.069
Area of absorber Plate (A_p)	0.11
Hydraulic diameter (D_h)	0.97
Air Density (ρ)	0.17
Mass flow rate of air (m)	1.6
Reynolds Number (Re)	1.93
Useful heat gain (Q_u)	2.55
Convective coefficient (h)	2.56
Nusselt Number (Nu)	2.73
Friction factor (*f*)	1.94

In this study, the performance of five swarm intelligence-based meta-heuristic algorithms, namely ACO, WOA, GOA, GWO, and DA are considered for optimizing the geometric and flow parameters of new solar air heaters as described above. Among these metaheuristic algorithms, ACO is the oldest, and GOA is the most recent proposed algorithm. The unique swarming behaviour of Ant, Whale, Grass-hopper, Grey wolf, and Dragonfly inspire these algorithms. Hence, the performance of these algorithms can be explored in the optimization problem of solar air heaters. The detailed flow chart of ACO, WOA, GOA, GWO, and DA algorithms are provided in Chapter 1.

4.8 Results and Discussion

Figure 4.6 to Figure 4.8 represent the variation of the Nusselt number with different roughness and flow parameters. The Nusselt number shows a vital function of h_p/D_h, p_p/h_p, and α_{ap}. It also notices that the Nu monotonously increases with Reynolds number. Also, it is higher in the case of a protrusion/dimpled absorber plate than a smooth absorber plate. This observation is because of vortex generation and flow impingement in the direction of flow. The presence of protrusion as a roughness over the absorber plate creates an adverse

pressure gradient due to friction that decelerates the airflow in the duct, promoting eddy formation, instability, flow separation, and energy dissipation.

Figure 4.6 exhibits the variation of Nusselt number with different h_p/D_h for a range of Reynolds numbers, keeping p_p/h_p =10 and α_{ap} =45^0 constant. It is observed that the Nu rises with an increase in h_p/D_h and Re. This fact is due to the more extensive penetration of protrusion in the free share flow region. It creates a higher separation and reattachment of the free share layer with a hot surface, and a strong secondary flow develops due to the larger reattachment of the free share layer. The maximum Nusselt number was found to be 125.66 with h_p/D_h = 0.069.

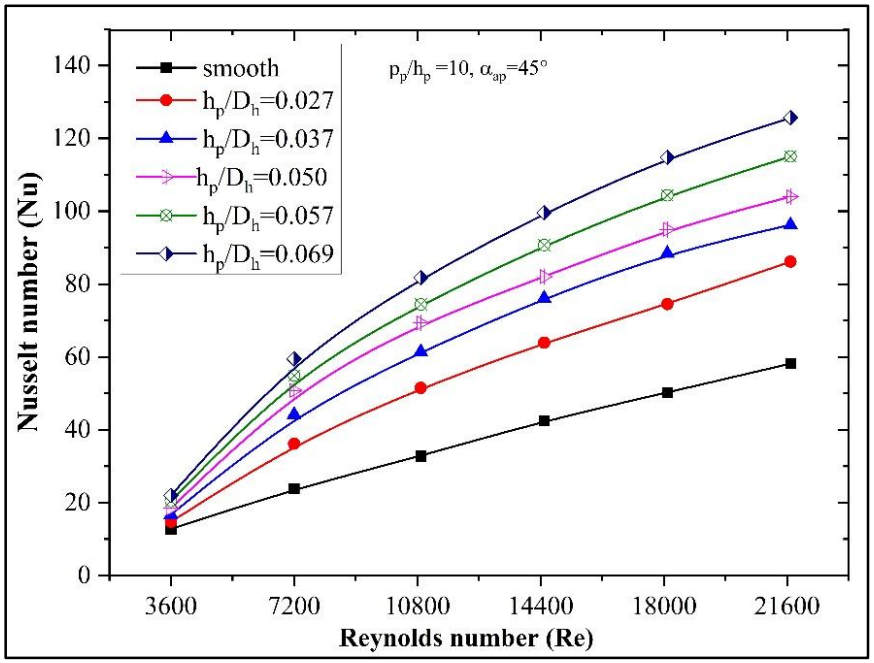

Figure 4.6: Variation of Nu with protrusion relative height.

Figure 4.7 depicts the deviation of the Nusselt number with relative protrusion pitch for a range of Reynolds numbers from 3600-21700. The p_p/h_p was varied from 6 to 14, keeping h_p/D_h and α_{ap} fixed. It can be observed that the Nusselt number increases with an increase in p_p/h_p up to 10, and it decreases with a further rise in p_p/h_p. This is may be due to maximum cross movement, eddies formation, and reattachment of air in V-downstream at p_p/h_p of 10. The reattachment of the free share layer with the lower p_p/h_p (<10) is minimal because of closer placements of successive rows of protrusions. On the other hand, having higher p_p/h_p (>10) causes a reduction in the total number of protrusions and more significant gaps between the rows that prevent vortex generation and secondary flow. The maximum value of the Nusselt number was found to be 110.50 at p_p/h_p =10.

Figure 4.8 shows the variation in Nu with varying α_{ap} for a range of Reynolds numbers. The angle of attack (α_{ap}) varied from 15-75º, keeping h_p/D_h=0.050 and p_p/h_p =10. Initially, the Nu rises with an increase in $\alpha_{ap,}$ attains the maximum value at α_{ap}=60º, and then decreases. The possible reason for this behaviour may be because there is maximum reattachment of primary flow and hindrance of air. The optimum hindrance of air in diagonal directions with V-notch results in maximum vortices generation. The maximum value of the Nusselt number was found to be 127.07 at α_{ap}=60º.The improvement in heat augmentation is expressed in terms of normalized Nusselt number (Nu/Nu_s) i.e. the ratio of Nusselt number for protrusion absorber plate (Nu) and Nusselt number for smooth absorber plate (Nu_s) is 2.56 corresponding to h_p/D_h= 0.050, p_p/h_p =10, α_{ap} = 60^0, and Re =7200, and the maximum normalized friction factor (f/f_s) is 4.30 at h_p/D_h= 0.050, p_p/h_p =10, α_{ap} = 45^0, and Re =7200.

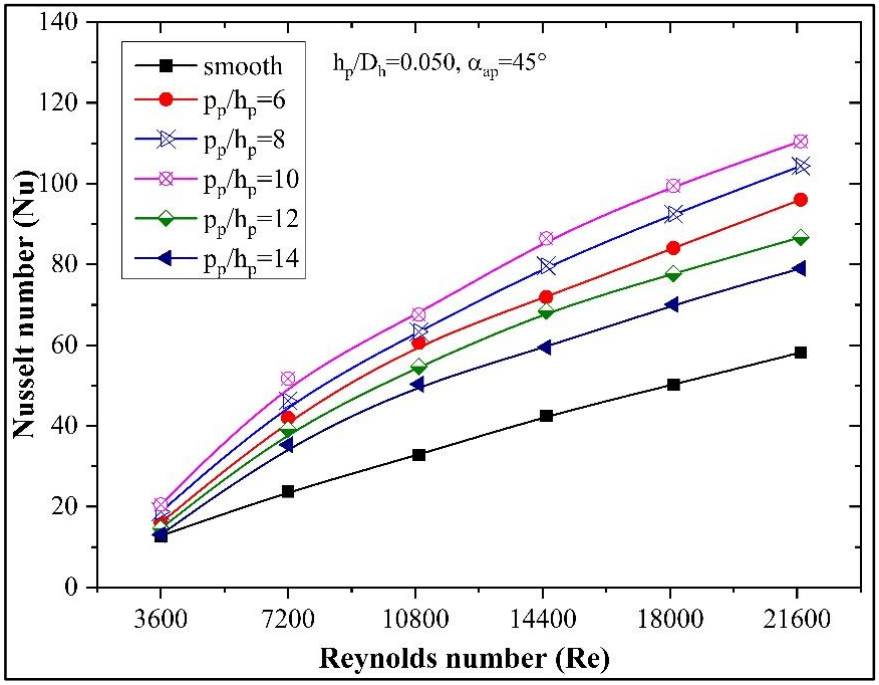

Figure 4.7: Variation of Nu with relative protrusion pitch.

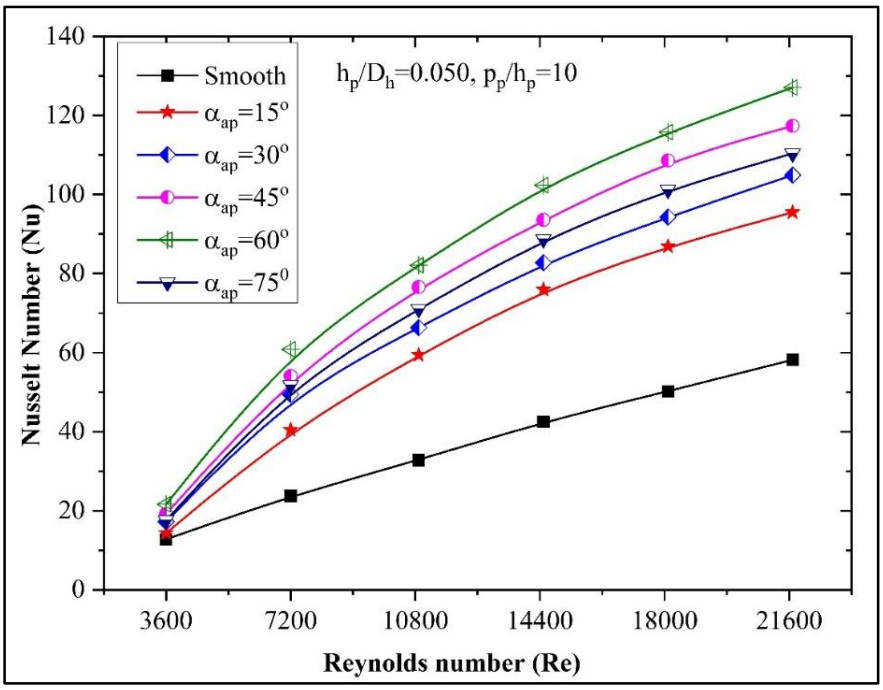

Figure 4.8: Variation of Nu with protrusion angle of attack.

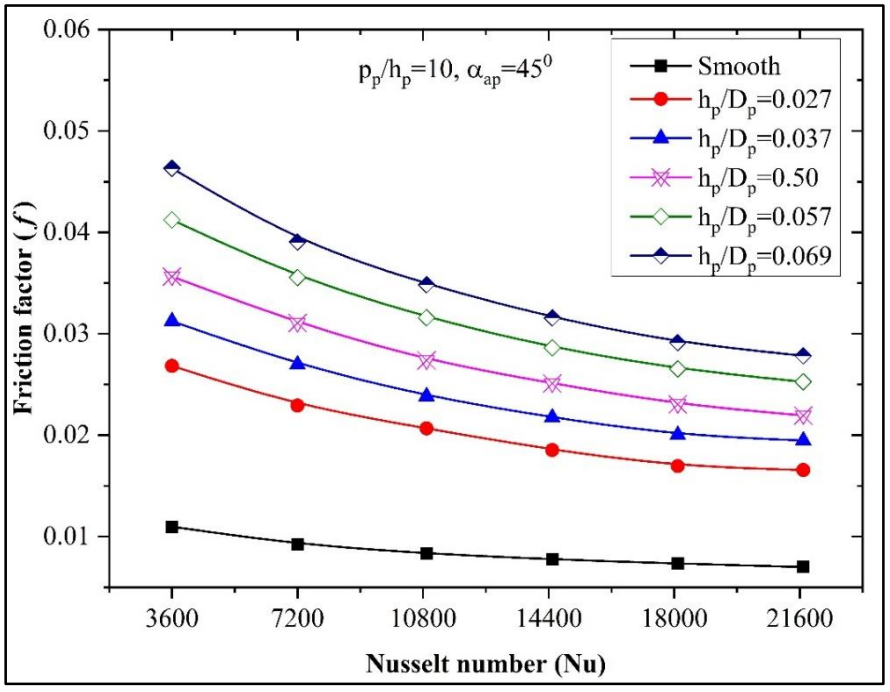

Figure 4.9 :Variation of friction factor with relative protrusion height.

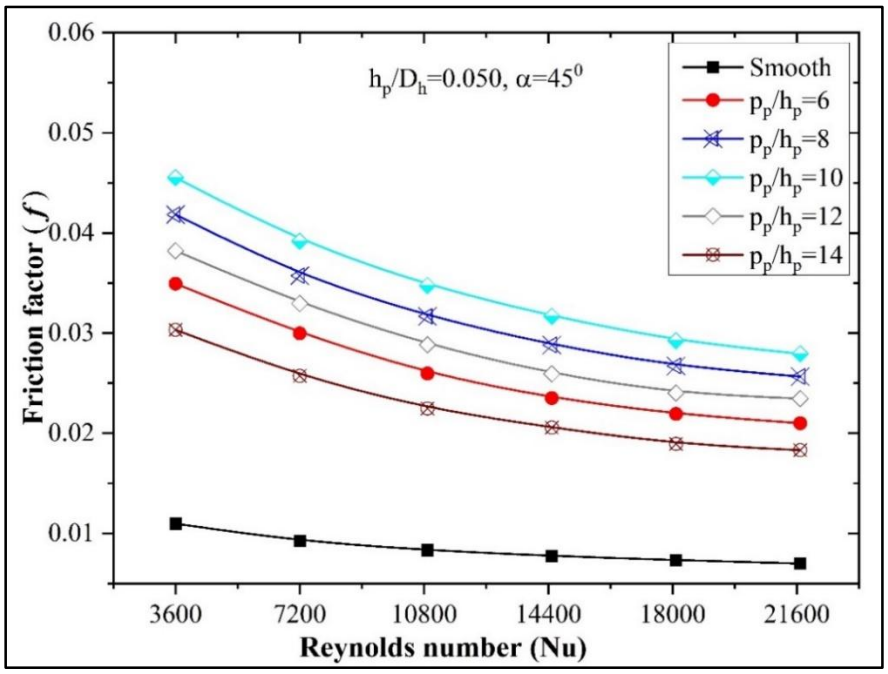

Figure 4.10 :Variation of friction factor with relative protrusion pitch.

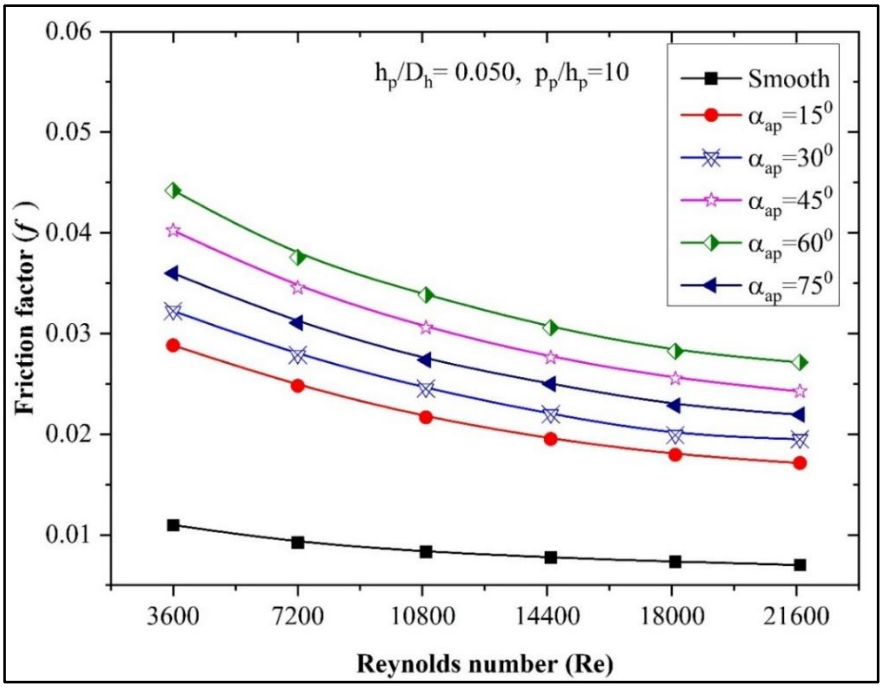

Figure 4.11 :Variation of friction factor with protrusion angle of attack.

Figure 4.9 to Figure 4.11 represent the variation of the friction factor with different roughness and flow parameters. The friction factor monotonously falls with increase in Reynolds number, possibly due to the suppression of the laminar sublayer at a higher Reynolds number.

Figure 4.9 shows the variation of friction factor with different h_p/D_h for a range of Reynolds numbers, keeping p_p/h_p =10 and α_{ap} =45^0 constant. The minimum and maximum

friction factor values have been observed with h_p/D_h= 0.027 and 0.069, respectively. The friction factor increases with an increase in h_p/D_h, and this is because of the formation of firmly secondary airflow.

Figure 4.10 illustrates the alteration of the friction factor with different values of p_p/h_p for a range of Reynolds numbers. The p_p/h_p varied from 6 to 14, keeping a fixed h_p/D_h=0.050 and $\alpha_{ap} = 45^0$. The minimum and maximum friction factor values have been observed at p_p/h_p=14 and 10, respectively. It has also been observed that the friction factor increases with an increase in p_p/h_p from 6 to 10 and then decreases. This is because the number of protrusions decreases with an increase in p_p/h_p value. There is minimum reattachment and less secondary flow generation while having lower p_p/h_p value and minimum vortice generation in more considerable p_p/h_p value; the maximum reattachment of flow at p_p/h_p=10, causing the highest friction.

Figure 4.11 depicts the variation of friction factor with different flow angle of attacks for a range of Reynolds numbers. The angle of attack value (α_{ap}) varied from 15-75º, keeping h_p/D_h=0.050 and p_p/h_p =10 constant. The results show that the friction factor increases with an increase in α_{ap} from 15º to 60º and then decreases. The minimum and maximum friction factors have been determined at α_{ap} =15º and α_{ap} = 60º, respectively. It may be a fact that a sharper V-notch angle provides lower drag from an aerodynamic point of view, and the friction increases as the V-notch angle increases. However, a much larger V-notch angle cannot provide frictional resistance. The maximum frictional resistance is obtained at α_{ap} = 60º of the protrusion angle of attack due to maximum frontal resistance. The hydraulic characteristic in terms of normalized friction factor (f/f_s), i.e. the ratio of friction factor for protrusion absorber plate (f) and friction factor for smooth absorber plate (f_s), is 4.30 at h_p/D_h= 0.050, p_p/h_p =10, $\alpha_{ap} = 45^0$, and Re =7200.

Figures 4.12, 4.13, and 4.14 illustrate the variation of thermohydraulic performance parameter (THPP) with varying geometric and flow parameters. The THPP is a non-dimension parameter used to define the overall performance of solar air heaters and calculated from Eq. (4.8). The value of THPP higher than one is considered significant heat augmentation over friction losses. The highest value of THPP was 1.60 at p_p/h_p =10, h_p/D_h=0.050, α_{ap} =60^0, and Re =7200. This is likely due to the conducive combination of geometric and flow parameters for heat augmentation and flow characteristics. Also, the maximum THPP is observed at Re =7200 in all three cases. It is a matter of fact that there is an increase in turbulence kinetic energy with an increase in Re, resulting in an increase

in Nu and a decrease in friction factor. The value of Nu/Nu_s dominated over $(f/f_s)^{1/3}$ at Re of 7200 and provided maximum THPP.

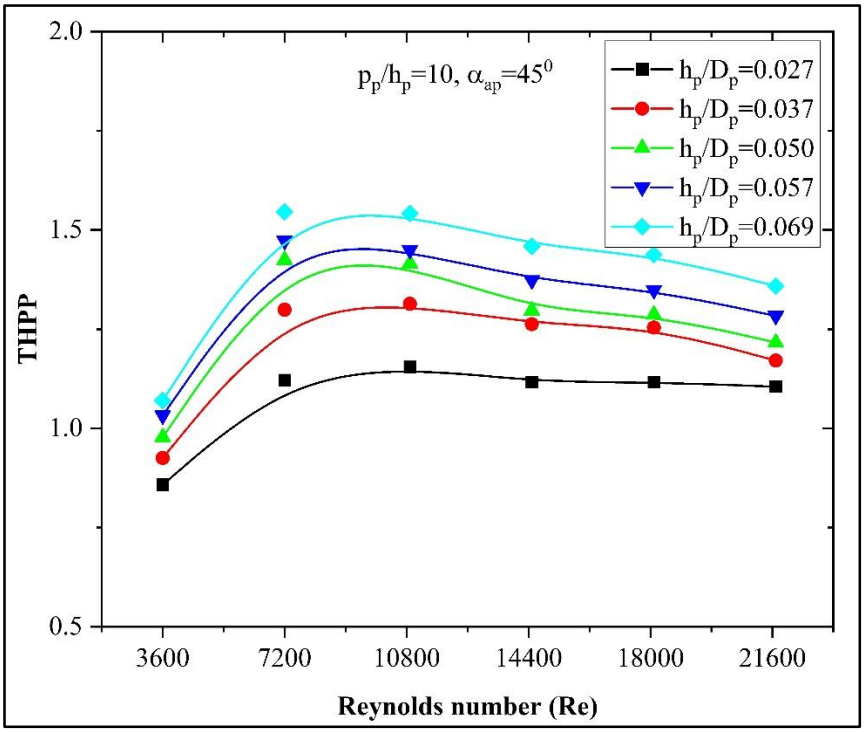

Figure 4.12 : Variation of THPP with relative protrusion height.

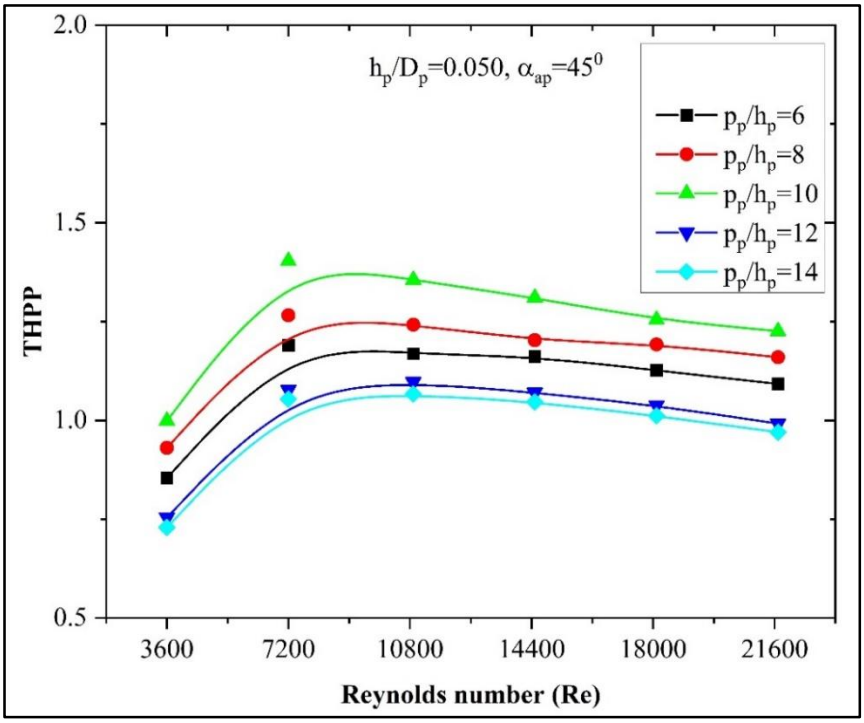

Figure 4.13 : Variation of THPP with relative protrusion pitch.

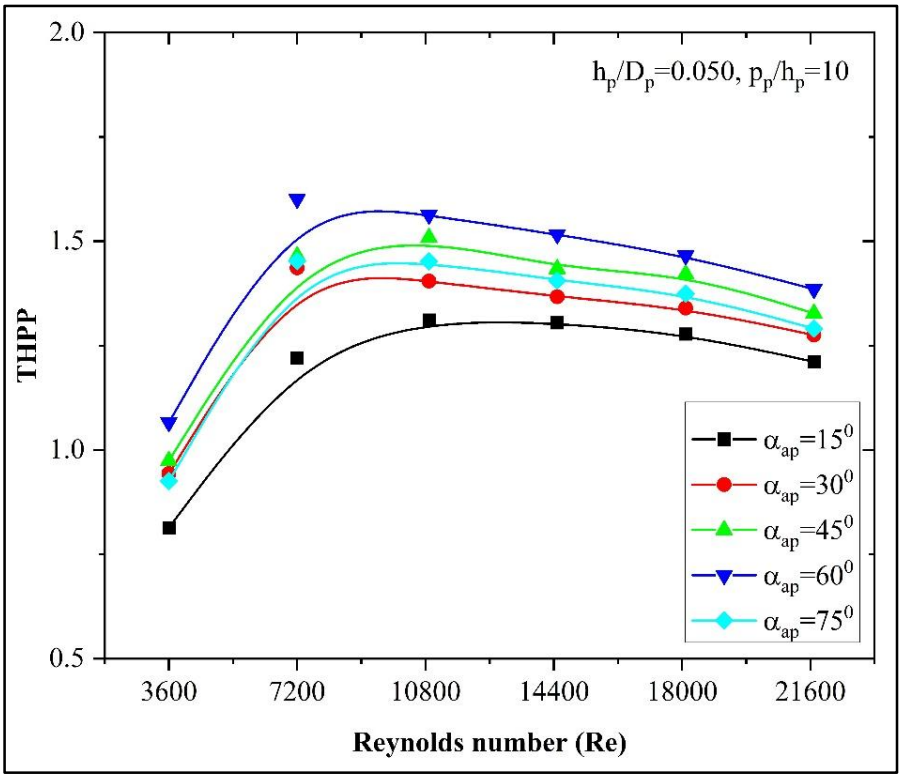

Figure 4.14 : Variation of THPP with relative protrusion angle of attack.

4.8.1 Correlations

From the experimental results, the output parameters viz. Nusselt number and friction factor have shown a vital function with p_p/h_p, h_p/D_h, α_{ap}, and Re. The functional relationship can be written as follows:

$$Nu = f(Re, p_p/h_p, h_p/D_h, \alpha_{ap}) \quad (4.13)$$

$$f = f(Re, p_p/h_p, h_p/D_h, \alpha_{ap}) \quad (4.14)$$

So, the above four dominating parameters have been considered to develop the statistical correlations.

4.8.1.i Correlation for Nusselt number (Nu)

Figure 4.15 shows the plot of all obtained Nu against the Re on a logarithmic scale. A functional relation obtained by regression analysis is represented as,

$$Nu = 0.9709\mathrm{Re} - 4.9439 \quad (4.15)$$

Taking logs on both sides,

$$Ln(Nu) = Ln(-4.9439) + 0.9709\,Ln(\mathrm{Re}) \quad (4.16)$$

Rearranging Eq. (4.16) becomes

$$\frac{Nu}{\mathrm{Re}^{0.9709}} = C_0 \tag{4.17}$$

where C_0 is constant and is a function of other influencing parameters. Considering the Relative height of protrusion (h_p/D_h) in the account, the value of C_0 is plotted against h_p/D_h in a logarithmic scale, as shown in Figure 4.16.

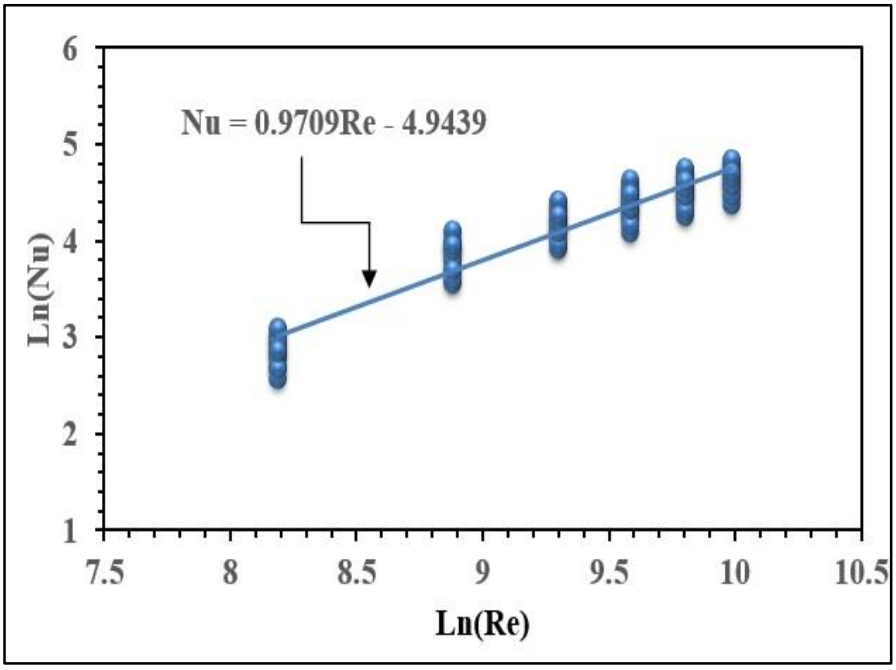

Figure 4.15 :Plot of Ln(Nu) Vs. Ln (Re)

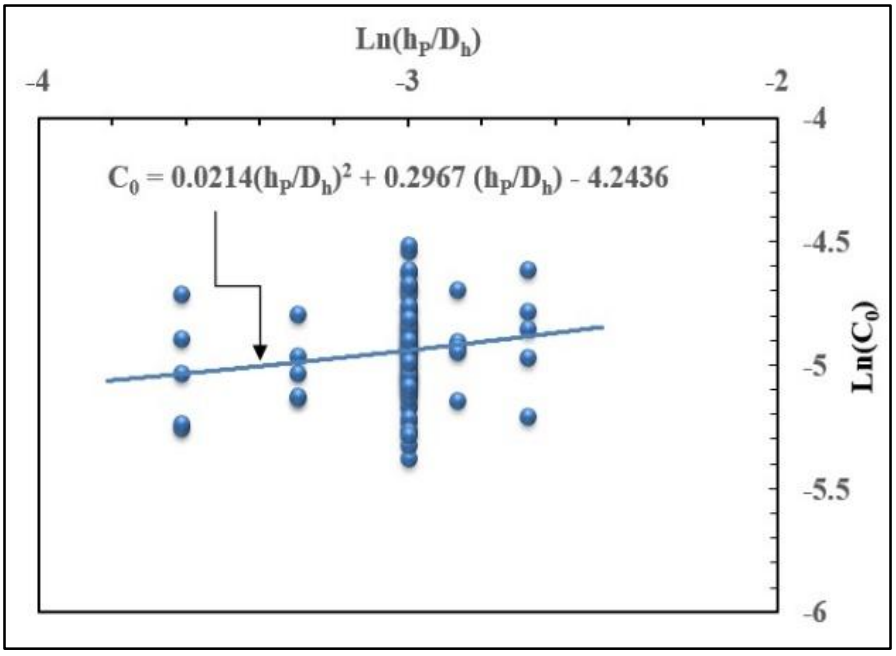

Figure 4.16 : Plot of Ln(C_0) Vs. Ln (h_p/D_h)

The regression analysis to fit the second-order polynomial is given by:

$$C_0 = 0.0214\left(\frac{h_p}{D_h}\right)^2 + 0.2967\left(\frac{h_p}{D_h}\right) - 4.2436 \tag{4.18}$$

Taking Logs on both sides provides,

$$Ln(C_0) = Ln(-4.2436) + 0.2967Ln\left(\frac{h_p}{D_h}\right) + 0.0214Ln\left(\frac{h_p}{D_h}\right)^2 \tag{4.19}$$

Rearranging the above equation yields,

$$\frac{Nu}{\mathrm{Re}^{0.9709}\left(\frac{h_p}{D_h}\right)^{0.2967}\exp\left(0.0214\times Ln\left(\frac{h_p}{D_h}\right)^2\right)} = C_1 \tag{4.20}$$

where C_1 is a constant and represents the functions of the relative pitch of protrusion (p_p/h_p). The value of C_1 and p_p/h_p is plotted in log-log scale as shown in Figure 4.17 and the regression analysis to fit second-order polynomial is given by

$$C_1 = -1.5693\left(\frac{p_p}{h_p}\right)^2 + 6.7298\left(\frac{p_p}{h_p}\right) - 11.378 \tag{4.21}$$

Taking Logs on both sides obtains

$$Ln(C_1) = Ln(-11.378) + 6.7298Ln\left(\frac{p_p}{h_p}\right) - 1.5693Ln\left(\frac{p_p}{h_p}\right)^2 \tag{4.23}$$

Rearranging the above equation converts

$$\frac{Nu}{\mathrm{Re}^{0.9709}\left(\frac{h_p}{D_h}\right)^{0.2967}\left(\frac{p_p}{h_p}\right)^{6.7298}\exp\left(0.0214\times Ln\left(\frac{h_p}{D_h}\right)^2\right)\exp\left(-1.5693\times Ln\left(\frac{p_p}{h_p}\right)^2\right)} = C_2 \tag{4.23}$$

where C_2 is constant and represents the functions of protrusion angle of attack ($\alpha_{ap}/45$). The value of C_2 and $\alpha_{ap}/45$ is plotted in log-log scale as shown in Figure 4.18 and the regression analysis to fit a second-order polynomial is as follows:

$$C_2 = 0.0032\left(\frac{\alpha_{ap}}{45}\right)^2 + 0.1482\left(\frac{\alpha_{ap}}{45}\right) - 11.372$$

(4.24)

Taking Logs on both sides to have,

$$Ln(C_2) = Ln(-11.372) + 0.1482Ln\left(\frac{\alpha_{ap}}{45}\right) + 0.0032Ln\left(\frac{\alpha_{ap}}{45}\right)^2 \tag{4.25}$$

The above equation can be rearranged as:

$$\frac{Nu}{\mathrm{Re}^{0.9709}\left(\frac{h_p}{D_h}\right)^{0.2967}\left(\frac{p_p}{h_p}\right)^{6.7298}\left(\frac{\alpha_{ap}}{45}\right)^{0.1482}\exp\left(0.0214\times Ln\left(\frac{h_p}{D_h}\right)^2\right)\exp\left(-1.5693\times Ln\left(\frac{p_p}{h_p}\right)^2\right)\exp\left(0.0032\times Ln\left(\frac{\alpha_{ap}}{45}\right)^2\right)} = C_3 \tag{4.26}$$

where, C_3 is a constant of 1.1513×10^{-5}.

Therefore, the final correlation obtained for the Nusselt number can be represented as

$$Nu = 1.1513\times10^{-5}\,\mathrm{Re}^{0.9709}\left(\frac{h_p}{D_h}\right)^{0.2967}\left(\frac{p_p}{h_p}\right)^{6.7298}\left(\frac{\alpha_{ap}}{45}\right)^{0.1482}$$
$$\exp\left(0.0214\times Ln\left(\frac{h_p}{D_h}\right)^2\right)\exp\left(-1.5693\times Ln\left(\frac{p_p}{h_p}\right)^2\right)\exp\left(0.0032\times Ln\left(\frac{\alpha_{ap}}{45}\right)^2\right) \tag{4.27}$$

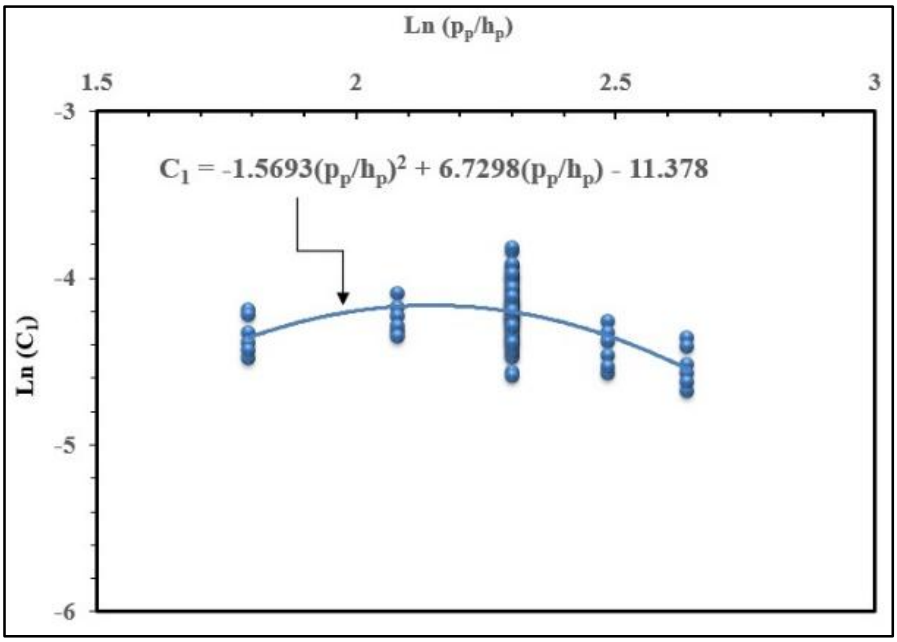

Figure 4.17 : Plot of Ln(C_1) Vs. Ln(p_p/h_p)

4.8.1.ii Correlation for friction factor

Similar steps have been used to obtain the correlation for the friction factor, and the correlations concerning different parameters are shown in Figure 4.19 to Figure 4.22. The final correlation for the friction factor is obtained as follows:

$$f = 4.39\times10^{-4}\,\mathrm{Re}^{-0.2842}\left(\frac{h_p}{D_h}\right)^{-1.9766}\left(\frac{p_p}{h_p}\right)^{3.7294}\left(\frac{\alpha_{ap}}{45}\right)^{0.1296}$$
$$\exp\left(-0.3381\times Ln\left(\frac{h_p}{D_h}\right)^2\right)\exp\left(-0.8774\times Ln\left(\frac{p_p}{h_p}\right)^2\right)\exp\left(-0.1549\times Ln\left(\frac{\alpha_{ap}}{45}\right)^2\right) \tag{4.28}$$

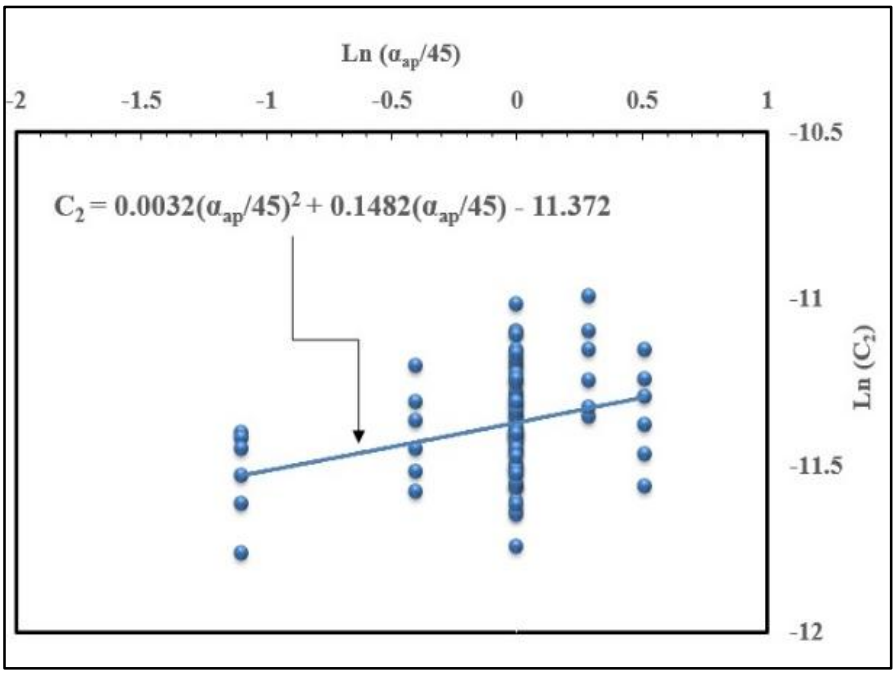

Figure 4.18 :Plot of Ln(C_2) Vs. Ln($\alpha_{ap}/45$)

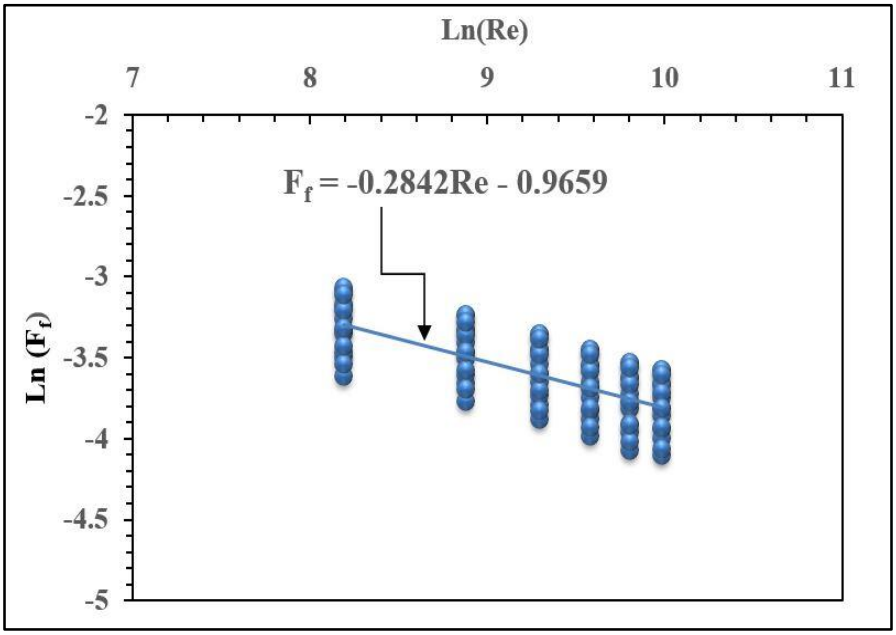

Figure 4.19 : Plot of Ln(F_f) Vs. Ln(Re).

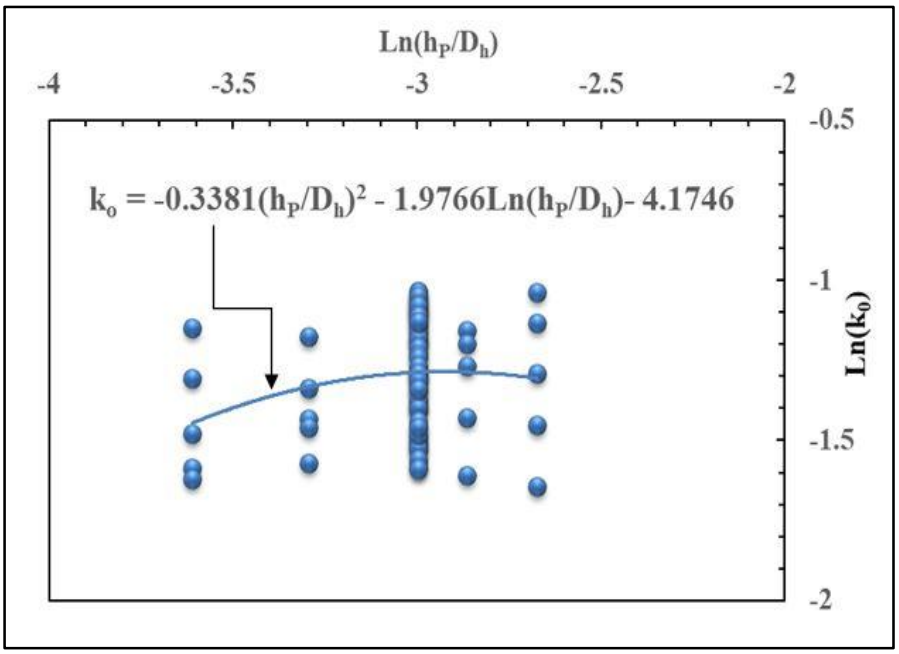

Figure 4.20 : Plot of Ln(k_0) Vs. Ln(h_p/D_h)

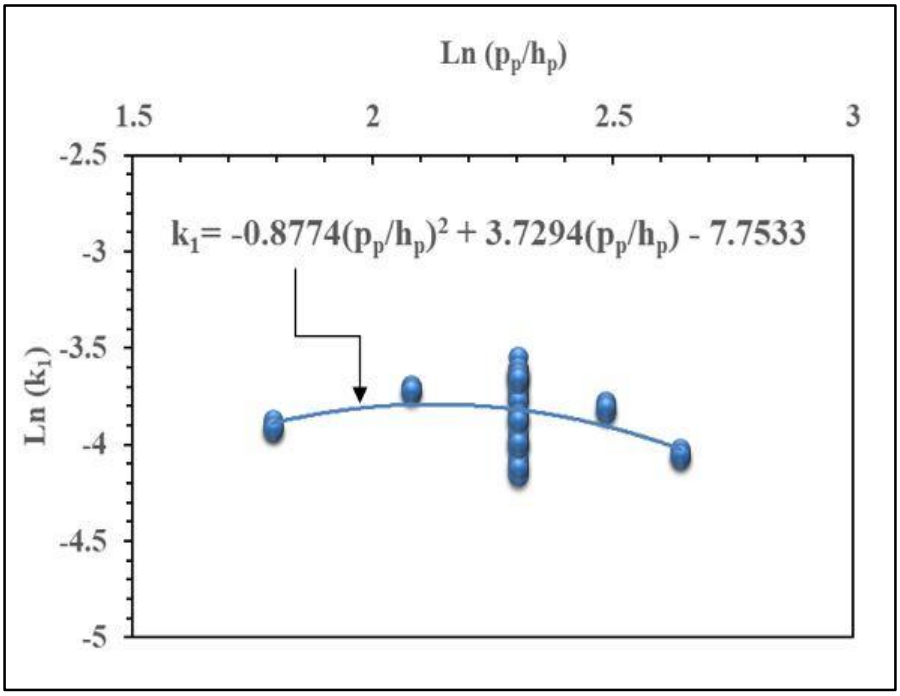

Figure 4.21 : Plot of Ln(k_1) Vs. Ln(p_p/h_p)

4.8.2 Performance comparison

The predicted value of Nu and *f* using correlation Eqs. 4.27 and 4.28 have been compared with the experimental values and plotted in Figure 4.23 and Figure 4.24. The average deviation of predicted results for Nu and *f* was observed as ±12.38% and ±10.71%, respectively, and it is considered to be within the acceptable limit [38], [31]. Also, the thermal-hydraulic performance parameter (THPP) of the presented new solar air heater has

been compared with similar studies by researchers and shown in Table 4.5. From this comparison, the proposed new solar air heater improved THPP compared to the cited literature.

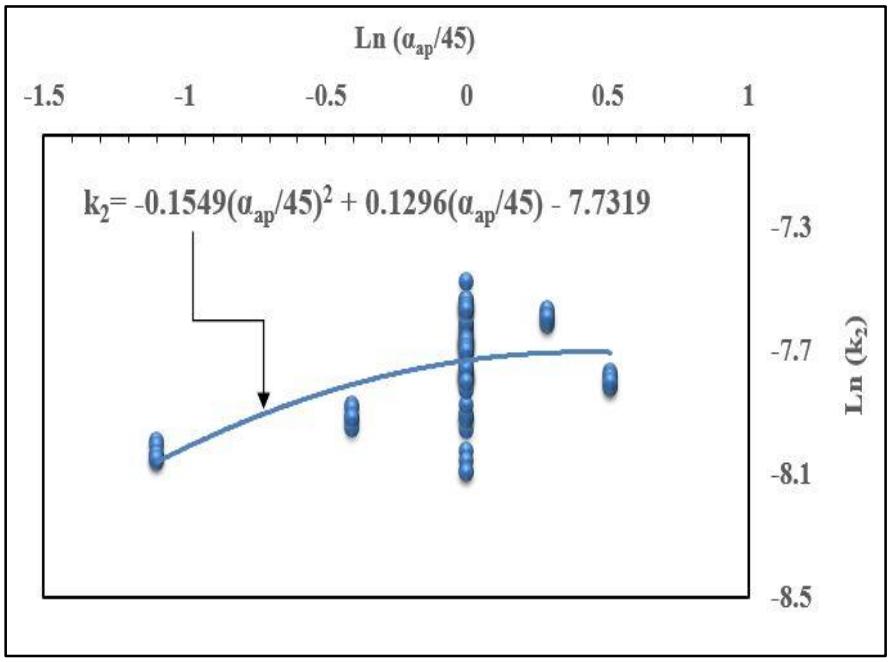

Figure 4.22 :Plot of Ln(k_2) Vs. Ln($\alpha_{ap}/45$)

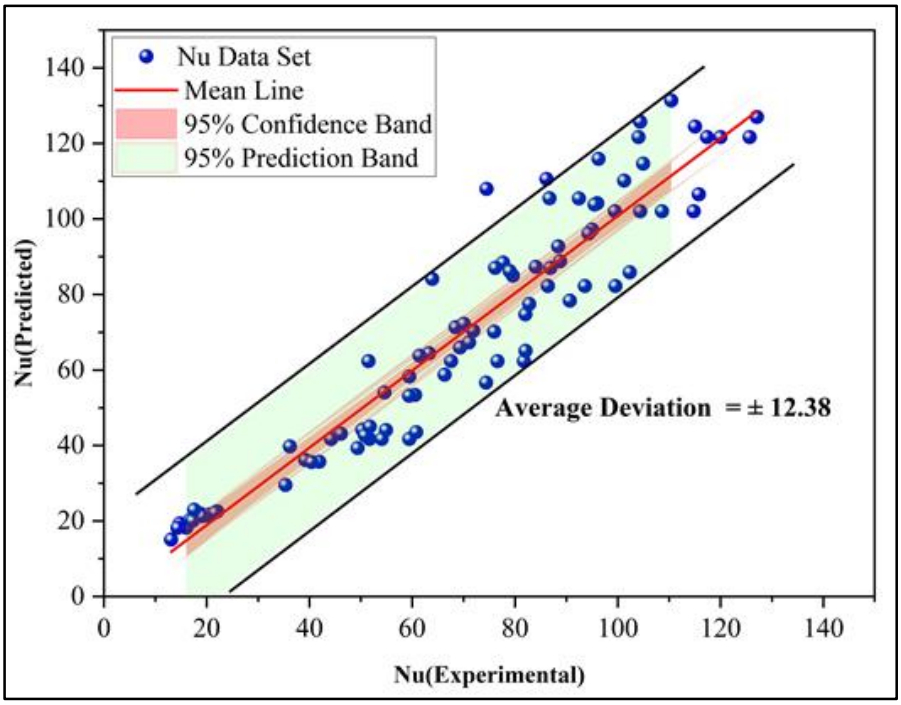

Figure 4.23 :Comparison of Nu (predicted) and Nu (Experimental).

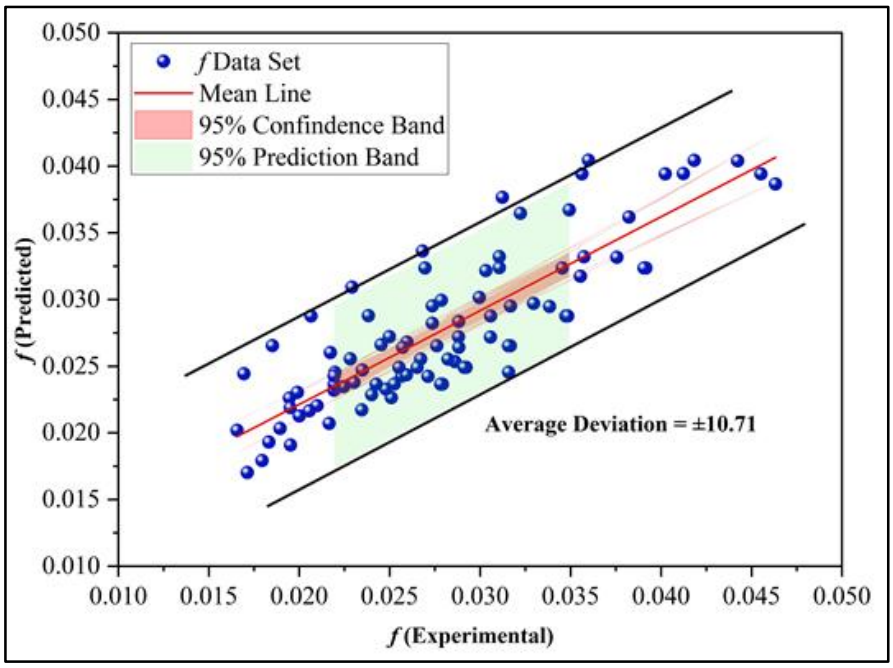

Figure 4.24 : Comparison of *f* (predicted) and *f* (Experimental)

Table 4.5: Comparison of THPP of the presented solar air heater with previous studies

Sl. no.	Duct Type	Roughness Type	Maximum THPP
Xie et al. [86]	Rectangular	Dimple	1.2
	Rectangular	Internal-protruded arrangement near the centre of the dimple	1.21
Liu et al. [87]	Rectangular	Dimple	1.44
	Rectangular	Dimple with secondary protrusion	1.47
Panda et al.[88]	Rectangular	miniature combined with dimple	1.15
Chamoli et al. [89]	Rectangular	V-shaped rectangular perforated blocks	1.3
Ku mar et al. [90]	Rectangular	Transverse semi-circular ribs with arched blocks	1.32
Present Study	Rectangular	V-notch pattern of hemispherical protrusions	1.60

4.8.3 Optimization

4.8.3.i Single objective optimization

The developed correlation for Nu and *f* is presented in Eqs. (4.27) and (4.28) are used to perform the single objective optimization using a metaheuristic approach. The Maximization of Nu and minimization of *f* are two objective functions. The upper and lower flow range and geometric parameters are selected as per Figure 4.2 A total of 100 iterations and five sets of runs were performed for each algorithm. The results obtained are provided in Table 4.6, and it can be clearly observed that WOA and GWO reveal the best

solution for both objectives rather than ACO, GOA, and DA. Also, the WOA attained the objective faster with less computational effort and negligible variance; this can be observed from the convergence diagram of Nu and *f*, as shown in Figure 4.25 and Figure 4.26.

Table 4.6: Results of single-objective optimization.

Objective Function	Method	Mean Output	Standard Deviation	Objective Function Output	Optimal flow and geometric parameters			
					Re	h_p/D_h	p_p/h_p	α_{ap}
Nu (Maximization)	ACO	139.75	2.16	140.92	21662.2	0.06	8.46	65.26
	GOA	142.55	3.95	144.56	21700	0.07	8.54	75
	WOA	144.56	0	144.56	21700	0.07	8.54	75
	GWO	144.567	0	144.56	21700	0.07	8.54	75
	DA	132.468	6.34	130.09	21349.5	0.07	8.61	41.75
f (Minimization)	ACO	0.014	0.001	0.013	18190.21	0.03	13.98	15.31
	GOA	0.012	0	0.012	21700	0.03	14	15
	WOA	0.012	0	0.012	21700	0.03	14	15
	GWO	0.012	0	0.012	21700	0.03	14	15
	DA	0.014	0.001	0.014	21673.52	0.03	13.27	15

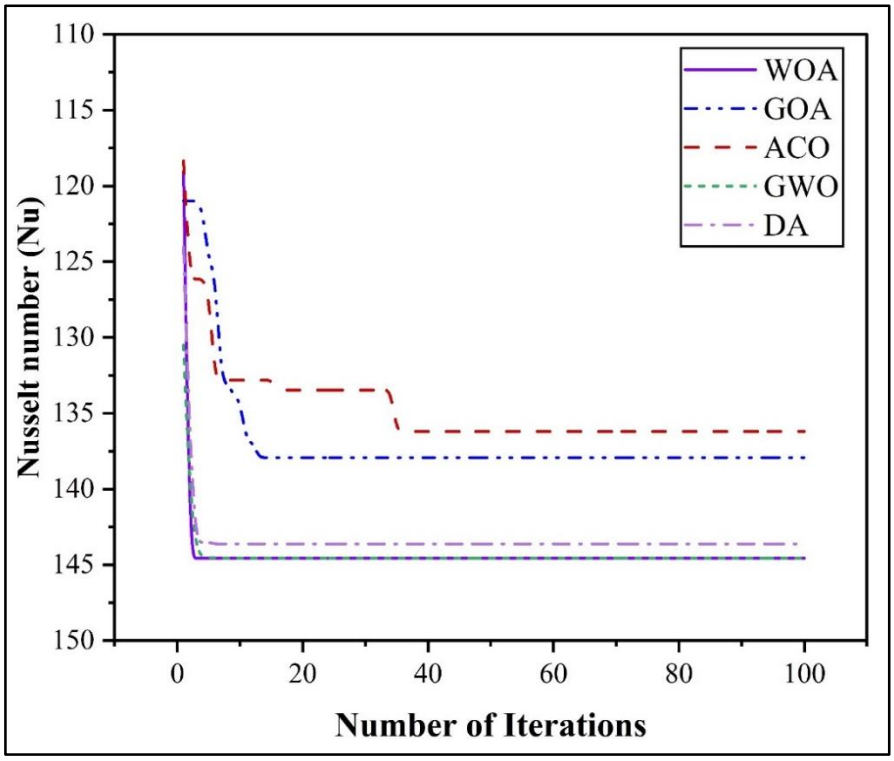

Figure 4.25 :Convergence diagram for Nu.

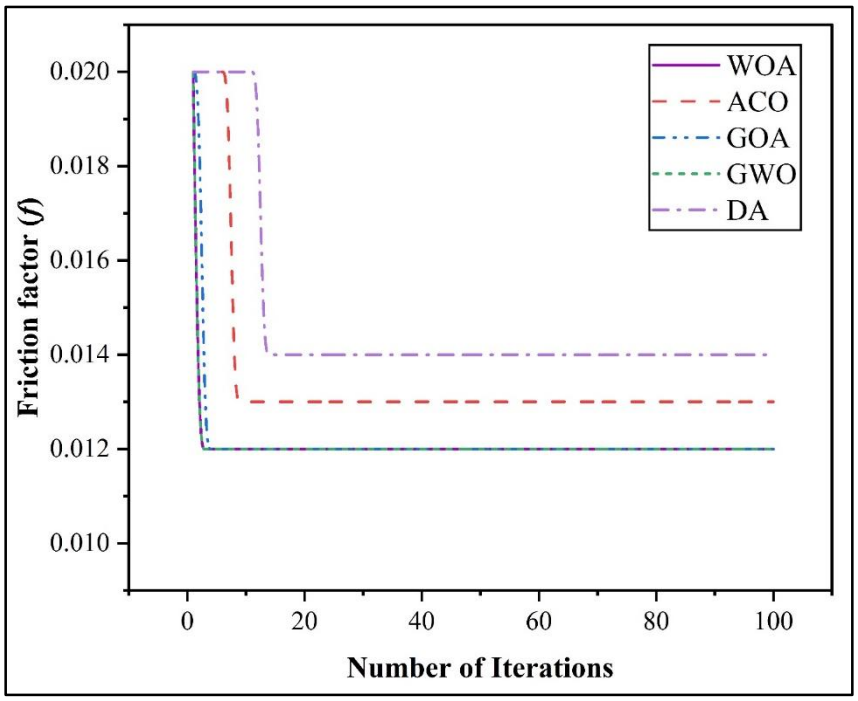

Figure 4.26 :Convergence diagram for *f*.

4.8.3.ii Multi-objective optimization

The parametric combination obtained in single objective optimizations is different for both objective functions, so it is not practical in actual practice to get maximum Nu and minimum *f* with two different parametric settings at the same time. In this contrast, meta-heuristic algorithm-based intelligence techniques have become more prevalent than aggregation-based techniques due to their greater flexibility and ability to generate multiple solutions. Thus, population-based meta-heuristic algorithms have generated the Pareto front by simultaneously optimizing the two objectives. Five hundred interns and 200 search agents, i.e., 500×200 function evaluations, have created optimal solutions. The total non-dominated optimum solutions generated by ACO, GOA, WOA, GWO and DA are 100, 54, 82,121, and 149, respectively. So, DA, is more exploratory than others. A Pareto front has been generated after combining all possible optimal values of Nu and *f*, representing a set of non-dominated solutions simultaneously containing the maximum Nu and minimum *f*. The Pareto optimal solutions for all three meta-heuristic algorithms, i.e., ACO, GOA, WOA, GWO, and DA are shown in Figure 4.27. From the Pareto front, it can be observed that the WOA has deliver consistent, non-dominated optimal solutions with less variation. The upper and lower range of all non-dominated solutions are provided in Table 4.7. The intermediate solutions between the upper and lower ranges give a compromise solution for both objective functions. The selection of a parametric setting for optimal solutions depends on the priority of the decision maker.

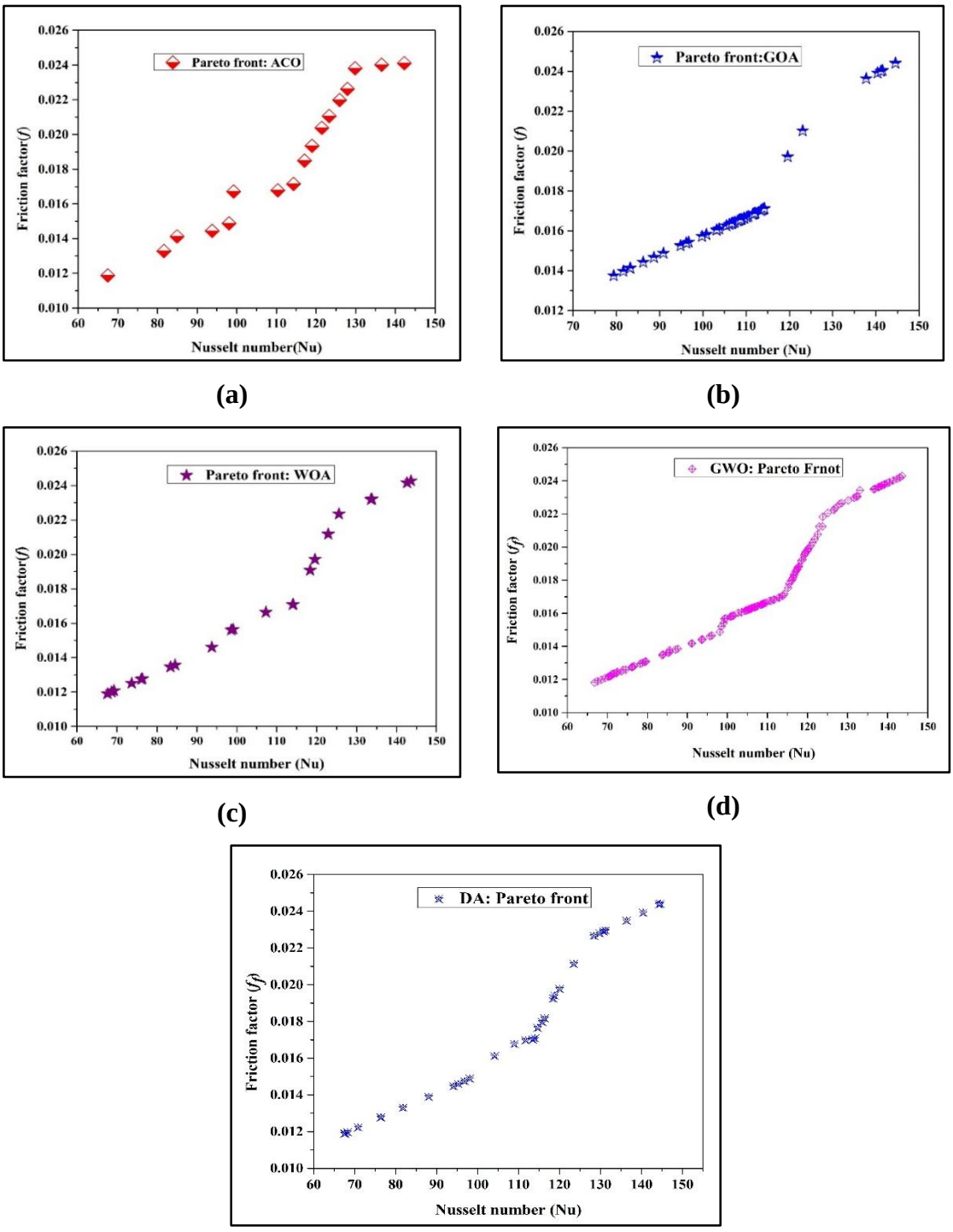

Figure 4.27 : Pareto front for:- (a) ACO, (b) GOA, (c) WOA, (d) GWO, (e) DA.

Table 4.7 : Results of Pareto multi-objective optimization.

Methods	Optimal Range	Output			Optimal parameters setting			
		Nu	*f*	THPP	*Re*	e_p/D_h	p/e_p	α_a
ACO	Upper	142.24	0.024	1.61	21700	0.069	9.44	75
	Lower	67.46	0.011	0.97	21700	0.027	13.91	15
GOA	Upper	144.52	0.024	1.63	21700	0.069	8.65	75
	Lower	79.38	0.013	1.08	21700	0.069	13.81	15
WOA	Upper	143.62	0.024	1.62	21700	0.069	9.10	75
	Lower	67.64	0.011	0.97	21700	0.027	13.88	15
GWO	Upper	143.08	0.024	1.62	21700	0.069	9.25	75
	Lower	66.80	0.012	0.96	21700	0.027	14	15
DA	Upper	144.55	0.024	1.63	21700	0.069	8.58	74.97
	Lower	68.23	0.011	0.97	21700	0.027	13.80	15

4.8.3.iii Validation of optimization results

The single- and multi-objective optimization results show that WOA yielded improved optimal solutions compared to other algorithms. The results obtained by WOA have been validated with experimental results are shown in Figure 4.28 and Figure 4.29. The results show a competent agreement with a correlation coefficient of about 0.95 and 0.90 for the Nusselt number and friction factor, respectively. Thus, the WOA metaheuristic optimization methodology is quite efficient regarding competence and global convergence and can deliver consistent, non-dominated optimal solutions with less variation.

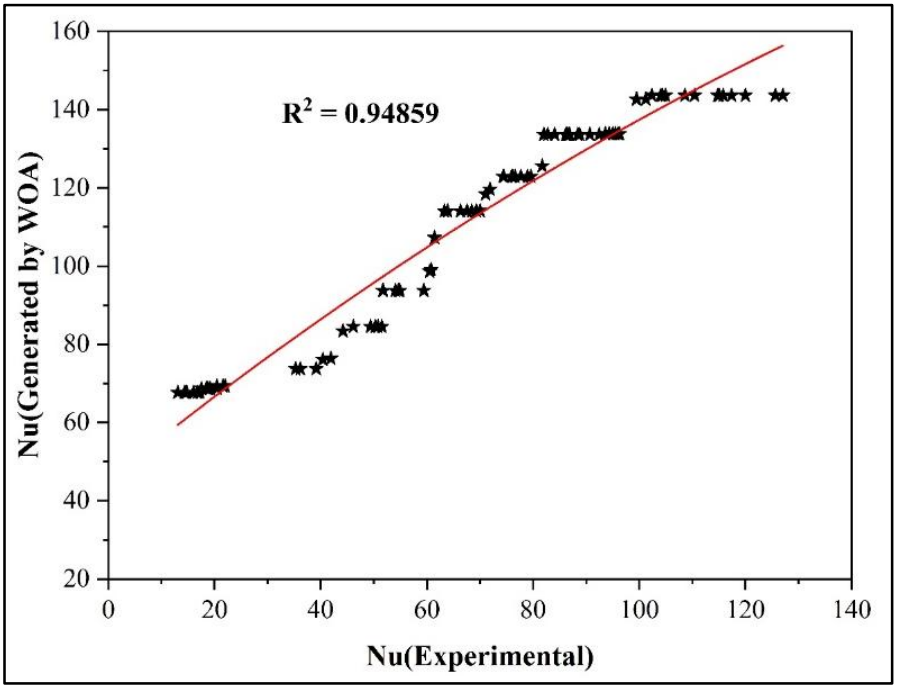

Figure 4.28 : Validation of WOA results with experimental results for Nusselt number.

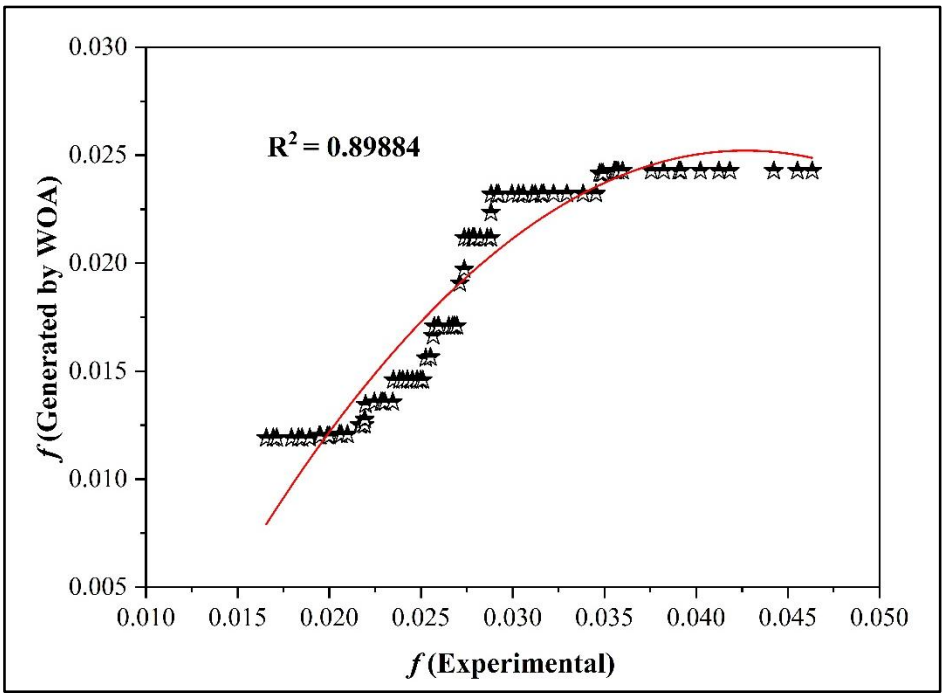

Figure 4.29 : Validation of WOA results with experimental results for friction factor.

4.9 Conclusions

This research completed a thermo-hydraulic performance evaluation of a new solar air heater with hemispherical protrusions in a single V-notch pattern. Extensive experimentation was conducted to analyze the effects of various flow and geometric parameters. A correlation for Nu and *f* is developed using regression analysis based on the experimental results. Also, three swarm intelligence-based metaheuristic optimization algorithms, namely ACO, GOA, WOA, GWO, and DA, have been employed for single and multi-objective optimization to select a suitable parametric setting for optimal output.

The significant findings from this study are as follows:

- The highest value of THPP is 1.60 for p_p/h_p =10, h_p/D_h=0.050, α_{ap} =60^0, and Re =7200.
- The maximum value of Nu is 127.07 at h_p/D_h=0.050, p_p/h_p =10 α_{ap}=60^0, and Re=21700.
- The minimum value of *f* is 0.0165 at h_p/D_h=0.027, p_p/h_p =10, α_{ap}=45^0, and Re=21700.
- Statistical correlations have been developed for Nu and *f* for flow and roughness parameters. The average deviation of predicted results for Nu and *f* was observed as ±12.38% and ±10.71%, respectively.

- In both the cases of single and multi-objective optimization, the WOA metaheuristic algorithm outperformed over other considered metaheuristic algorithms.

4.10 Summary

In this chapter, the effects of hemispherical protrusions in V-notch patterns have been investigated. For this investigation, an experimental setup has been designed and fabricated as per the ASHRAE Standard 93-77 standard. The dimension of a rectangular solar air heater is 1000 mm × 330 mm × 30 mm, and the aspect ratio is 11. The hemispherical protrusions were created using punch and die in an aluminium absorber plate. Various measuring instruments such as thermocouples, digital micro-manometer, digital anemometer, and pyranometer were installed to measure temperature, pressure drop, airflow, and irradiation. A 0.5 HP centrifugal blower was used to provide airflow through the duct, and the halogen lamp gave an artificial source of heat. The performance parameter of the solar air heater was evaluated by alternating the geometrics and flow parameters in 15 sets of experiments.

Nusselt number (Nu) and friction factor (*f*) are analyzed as two major output parameters that specify solar air heaters' thermal and hydraulic performance. Also, the effectiveness of protrusions as artificial roughness is considered as a thermo-hydraulic performance parameter (THPP). The experimental results show that artificial roughness as hemispherical protrusions in a V-notch pattern effectively enhanced the thermo-hydraulic performance of solar air heaters by generating turbulence at the laminar sub-layer zone. The maximum value of Nu is 127.07 at h_p/D_h=0.050, p_p/h_p =10 $\alpha_{ap}=60^0$, and Re=21700. The minimum value of *f* is 0.0165 at h_p/D_h=0.027, p_p/h_p =10, $\alpha_{ap}=45^0$, and Re=21700.The highest value of THPP is 1.60 to p_p/h_p =10, h_p/D_h=0.050, $\alpha_{ap}=60^0$, and Re =7200.

Based on the experimental results, a statistical correlation model for Nu and *f* has been developed using regression analysis. The average deviation in predicted and experimental results for Nu and *f* was observed as ±12.38% and ±10.71%, respectively.

Further, the comparative optimization performance analysis has been performed using five metaheuristic optimizations, which are Ant colony optimization (ACO), Whale optimization algorithm (WOA), Grass-hopper optimization algorithm (GOA), grey wolf optimization (GWO), Dragonfly algorithm (DA). The WOA delivered the best performance in both single and multi-objective optimization.

CHAPTER 5

SEMI-CAPSULE PROTRUSIONS IN STAGGERED PATTERN

Preface

This chapter discusses heat transfer, flow characteristics, and thermo-hydraulic performance of solar air heater having semi-capsule protrusions in a staggered pattern. The performance of SAH has been examined experimentally after considering the variation of different geometric and flow parameters. Based on the experimental observations, an algebraic correlation between the Nusselt number and friction factor was developed. Further, the algebraic correlations were used for single and multi-objective optimization of influencing parameters using five metaheuristic algorithms, i.e. Grey Wolf optimization algorithm (GWO), Whale optimization algorithm (WOA), Grass-hopper optimization algorithm (GOA), Ant colony optimization algorithm (ACO), and Dragonfly algorithm (DA).

5.1 Introduction

In this chapter the effects of semi-capsule protrusions on the thermo-hydraulic performance of a solar air heater equipped with semi-capsule-shaped protrusions roughness arranged in a staggered pattern has been discussed. The heat transfer, flow characteristics, and thermo-hydraulic performance of solar air heater are examined experimentally with altered relative protrusion heights (e_c/D_h = 0.041-0.067), Relative pitch (p/e_c = 18-36), protrusion angle as angle of attack (α_p = 30º-90º), and Reynolds number (Re=3600-21700). Also, a comparative performance analysis of five metaheuristic optimization, i.e. Grey Wolf optimization algorithm (GWO), Whale optimization algorithm (WOA), Grass-hopper optimization algorithm (GOA), and Ant colony optimization algorithm (ACO), and Dragonfly algorithm (DA), has been performed.

The extensive literature survey reveals that using roughness as protrusions or dimples becomes attractive for the researchers as its embossing in the absorber plate is easy without extra weight. Also, flow over the protrusion and dimples is easy with

minimum friction [31]. These features motivated the authors to investigate roughness as protrusions. In this proposed roughness, semi-capsule-shaped protrusions with successive alter orientations in a staggered pattern are engraved in the absorber plate as shown in Figure 5.1. Each alternate protrusion is positioned in the lateral direction in the fluid flow path, and corresponding successive protrusions are arranged in angular position in both rows and column-wise with an angle for different sets of experiments. The shape of the protrusion and its patterns make the proposed roughness new, and best of the authors' knowledge, there is no such literature available. Before conducting this experiment, the authors pre-assumed that the roughness in the form of semi-capsule-shaped protrusions with successive alter orientations would be able to increase secondary flow and vortices generation that may improve the thermohydraulic performance. Further, the literature review also discloses that researchers have explored various analytical and metaheuristic optimization techniques to determine the best parametric settings for optimal performance of SAHs. It was observed that the analytical optimization techniques face difficulties in optimizing complex problems. However, the metaheuristic algorithms-based optimization techniques supersede optimization problems with multi, non-linear, distinct, and unceasing variables with less information and more computational effort. However, each metaheuristic algorithm has unique behaviour when solving problems due to its stochastic nature. So, a comparative performance investigation is most required for a particular optimization problem. Therefore, the present research work also explored the comparative performance analysis of four metaheuristic algorithms, namely, GWO, WOA, GOA, ACO, and DA.

Figure 5.1 : Actual absorber plate having semi-capsule protrusions

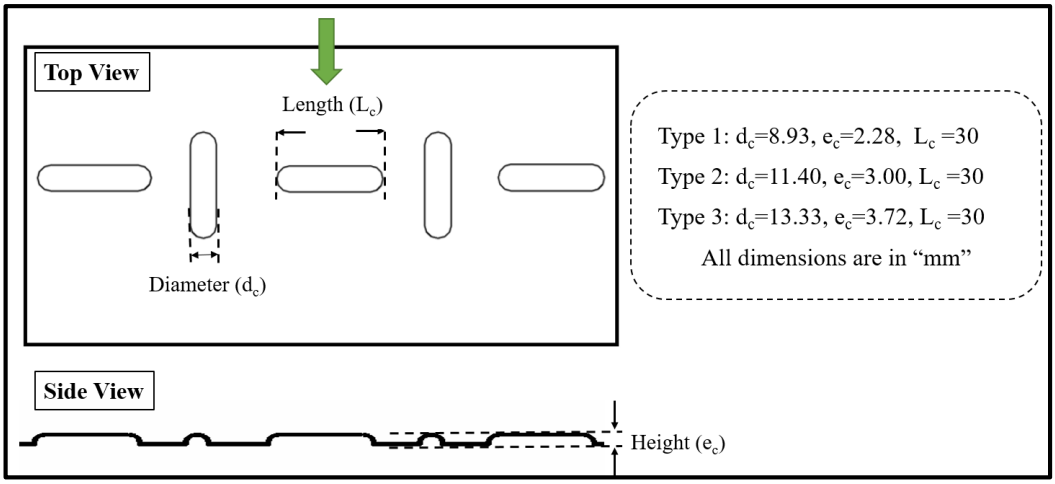

(a)

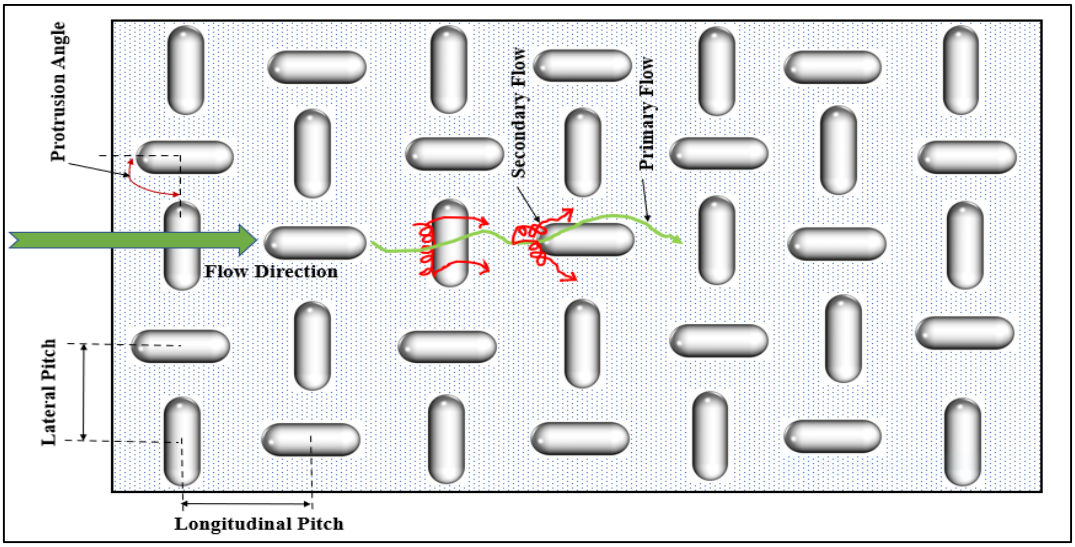

(b)

Figure 5.2: Absorber plate **(a)** 2-D diagram **(b)** Schematic representation of absorber plate

5.2 Experimental Setup and Conduction

The experimental setup was fabricated and installed at Sikkim Manipal Institute of Technology, Sikkim, India. Figure 5.2 (a) and (b) show the schematic diagram and actual setup. The rectangular SAH is designed based on ASHRAE[76] standards, having dimensions of 2200mm × 330mm ×30mm, comprises of entry, test, and exit section lengths of 800mm, 1000mm, and 400mm, respectively, as presented in Figure 5.3. The aspect ratio of the channel is 11. Minimizing heat loss from the duct is due to the insulation from the bottom and two sides, which are made of wood powder and glass wool. The semi-capsule shape protrusions are embossed on an aluminium absorber plate with the help of a punch and die. The real picture and schematic drawing of the absorber plate are shown in Figure

5.1 and Figure 5.2, respectively. An absorber plate is placed inside the test section, where four sensors directly interact with the plate. Eight more temperature sensors are positioned above and beneath the plate at a specific distance to determine the temperature of the flowing and trapped air. The plate is airtight around its edge for the airflow through the duct. The energy-absorbed plate is sealed and covered with transparent glass above to trap hot air. A centrifugal blower was engaged to blow the air in a rectangular duct, and a butterfly valve controlled the flow rate. A vane-type digital anemometer measured the airflow velocity. Four halogen lamps provide artificial solar radiation with constant heat flux and are controlled by autotransformers. A digital pyranometer determined the irradiation falling on the test section, whereas a digital differential manometer noticed the pressure drop in the test section. The present experiment was conducted under steady-state conditions. Table 5.1furnishes this study's geometric range and flow parameters.

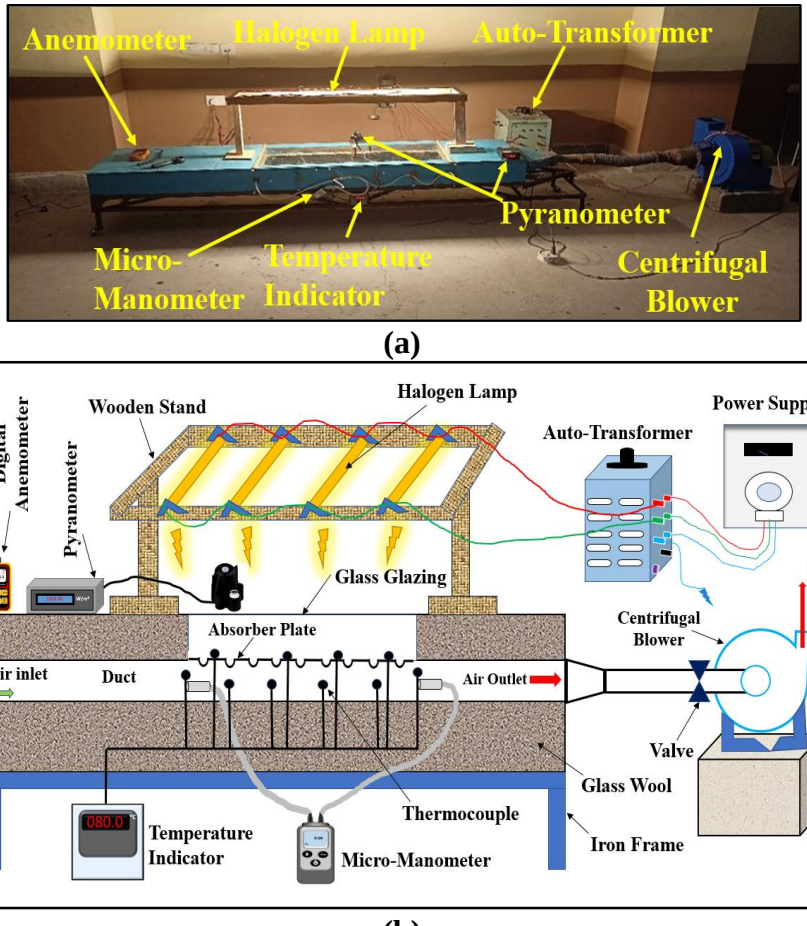

Figure 5.2:Experimental setup: (**a**) Actual experimental setup (**b**) Schematic diagram

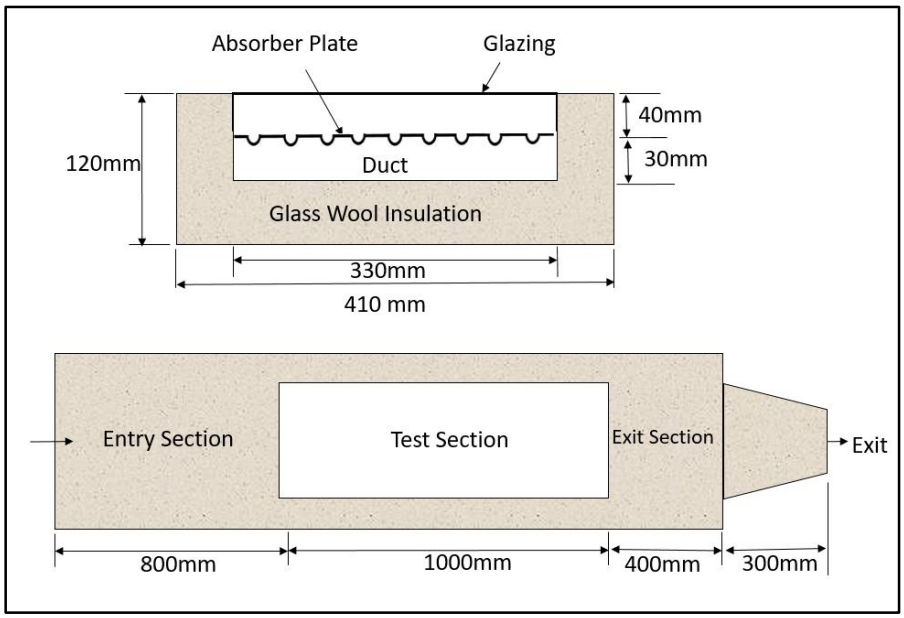

Figure 5.3: Dimensions of the test duct.

Table 5.1 : Geometric and flow parameters.

Sl. no.	Parameter	Range	Type
1	Relative pitch (p/e_c)	18-36	Geometric parameter
2	Relative protrusion height (e_c/D_h)	0.041-0.067	Geometric parameter
3	Alternate protrusion angle (α_p)	30º-90º	Geometric parameter
4	Reynolds Number (Re)	3600-21700	Flow parameter

5.2.i Data Reduction

After collecting the data, the energy analysis was performed[31] . For energy analysis the mass flow of air can be determined from the mass conservation equation [39],

$$m = \rho A_d V \tag{5.1}$$

The following formula obtains the usefulness of heat gain [36],[91]:

$$Q_u = mC_p(T_o - T_i) \tag{5.2}$$

The heat transfer coefficient (h) is to be evaluated as [36],[91]:

$$h = \frac{Q_u}{A_p(T_{pm} - T_{ma})} \tag{5.3}$$

The flow parameter, namely Reynolds number (Re), is computed as [91], [29]:

$$Re = \frac{\rho V D_h}{\mu} \tag{5.4}$$

where mean hydraulic diameter (D_h) is given by[91], [29] :

$$D_h = \frac{4WH}{2(W+H)} \tag{5.5}$$

The thermal performance parameter, Nusselt number (Nu) is estimated by [39], [31]:

$$Nu = \frac{hD_h}{k} \tag{5.6}$$

The hydraulic performance parameter, friction factor (f_f) can be calculated by [31],[42]:

$$f_f = \frac{2\Delta P D_h}{4\rho L V^2} \tag{5.7}$$

The over-all performance is estimated as thermo- hydraulic performance index (THPi). THPi >1 validates the notable progress in the performance. The THPi expression is given by [92]:

$$THPi = \frac{Nu/Nu_s}{(f_f/f_s)^{1/3}} \tag{5.8}$$

5.2.ii Data validation test

Data validation is necessary for any experimentation to ensure similarity with past research. The experimental results obtained from the presented test rig are validated with standard correlations for similar designs with smooth absorber plates. The Nusselt number and friction factor standard value is calculated using Dittus-Boetler [83] and Blasius equations [84] as provided in Eqs. (9) and (10).

$$Nu_s = 0.023\, Re^{0.8} Pr^{0.4} \tag{5.9}$$

$$f_{fs} = 0.085 Re^{-0.25} \tag{5.10}$$

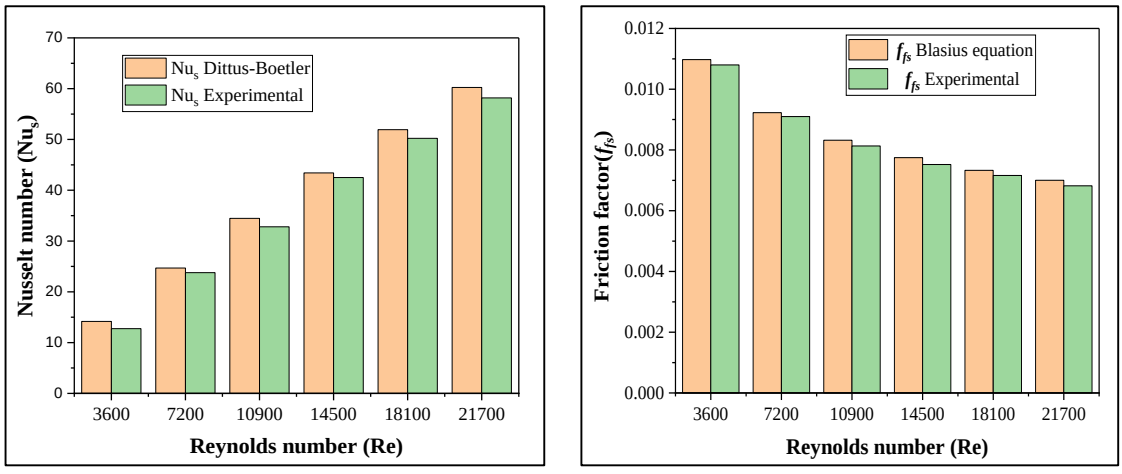

(a) **(b)**

Figure 5.4 : Practical data validation with variations of Re: (**a**) Nusselt number, and (**b**) Friction factor.

Figure 5.4 displays the verification of testing results with standard theoretical results. The comparison outcomes reveal decent closeness, with a mean absolute deviation

of 4.55% and 2.17% for Nu_s and f_{fs}, respectively, which validates the precision of the data taken in the investigations.

5.2.iii Uncertainty test

An uncertainty test is conducted to check the accuracy of measured and calculated parameters. It defines the processes' errors and validates the experimental results. Kline and Mcclintock equations [85] are used for the uncertainty study.

$$U_x = \left[\left(\frac{\delta x}{\partial k_1}\delta k_1\right)^2 + \left(\frac{\delta x}{\partial k_2}\delta k_2\right)^2 + \cdots + \left(\frac{\delta x}{\partial k_n}\delta k_n\right)^2\right]^{1/2} \quad (5.11)$$

Table 5.2 shows the uncertainty of diverse gauging instruments. Table 5.3 provides uncertainty in computing numerous parameters.

Table 5.2: Uncertainty of gauging devices

Gazing Parameter	Instrument	Uncertainty
Sizable Dimensions	Vernier Caliper	±0.02mm
Temperature	Thermocouple	±1ºC
Air Velocity	Anemometer	±0.1m/s
Pressure Drop	Digital Micro-Manometer	±0.1Pa
Irradiation	Pyranometer	±20W/m^2

Table 5.3 : Uncertainty of gauging parameters.

Parameter	**%Uncertainty**
Area of duct (cross-section) (A_d)	0.069
Absorber plate surface area (A_p)	0.11
Hydraulic mean diameter (D_h)	0.97
Air Density (ρ)	1.65
Air mass flow rate (m)	2.34
Reynolds Number of airflow (Re)	3.45
Usefulness of heat gain (Q_u)	2.61
Convective heat transfer coefficient (h)	2.62
Nusselt Number for convection (Nu)	2.74
Friction coefficient (f_f)	2.54

5.3 Metaheuristic optimization

Metaheuristic optimization techniques have progressed rapidly alongside advancements in computational power. These techniques consist of two primary algorithms: single-based and population-based. The first algorithm produces individual solutions, whereas the second generates multiple solution sets with each iteration. Again, the second algorithm has various types: evolutionary, swarm intelligence, event, and physics-based.

Five swarm intelligence-based metaheuristic algorithms, namely Grey Wolf optimization (GWO), Whale optimization algorithm (WOA), Grass-hopper optimization algorithm (GOA), Ant colony optimization (ACO), and Dragonfly algorithm(DA) are employed to optimize the design conditions of the proposed solar air heater. The flowcharts of WOA, GWO, GOA, ACO and DA algorithms are already provided in chapter 1.

5.4 Results and discussion

The flow parameters effect for Reynolds number and different parameters involving geometry, viz. e_c/D_h, p/e_c, and α_p has been analyzed by varying one of them and keeping constant others. The analyzed parameters are Nu, f_f, and THPi.

5.4.i Influence of Reynolds number (Re)

Figure 5.5 shows the Nusselt number variation with Reynolds numbers with selected roughness parameters. The results highlight a monotonously increasing function of Nu with Re regardless of roughness parameters. This represents a direct and significant influence on heat transfer and fluid flow behaviour. The enhanced turbulence intensity with higher Re carries strong flow momentum and turbulent kinetic energy, causing a higher mass flow of air and intensified flow disturbance. This disrupts the thermal boundary layer near, reducing thermal resistance and increases convective heat transfer coefficient. An increase in Nu concerning different roughness parameters is much higher than that of the absorber plate without a roughened surface. This trend is owing to the protrusion roughness parameter, which converts the laminar flow. The breaking of the laminar sub-layer generates energized secondary flow and vortices, augmenting the absorber plate's heat rate. Re=21700 and 3600 provide the most elevated and most down values of the Nusselt number, respectively. The highest Nu is observed at an e_c/D_h ratio of 0.067, p/e_c of 27, and an α_p of 60º.

On the other hand, the friction factor drops with an increase in Reynolds number, as depicted in Figure 5.6. This may be due to a decrease in velocity gradient and frictional resistance with the increase in Re. The maximum friction factor is observed at the lowest value of Re and corresponding e_c/D_h values. This tendency is quite evident: the larger size of the semi-capsule protrusion (e_c) offers more drag at low kinetics fluid flow. The drag resistance decreases further with an increase in the flow's kinetic energy. The highest and lowest f_f are found at Re = 3600 and 21700, corresponding to e_c/D_h of 0.067 respectively.

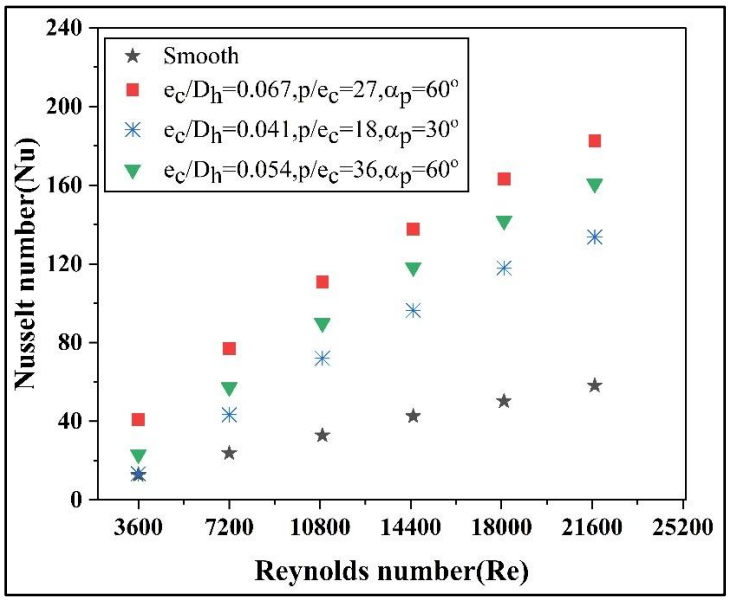

Figure 5.5 : Effects of Re on Nu.

5.4.ii Effects of comparative protrusion tallness (e_c/D_h)

The impact of e_c/D_h on Nu and f_f during Reynolds numbers variation from 3600 to 21700 are presented. Three values of e_c/D_h are taken as 0.041, 0.054, and 0.067. Figure 5.7 shows a growth in Nu with e_c/D_h. This result is due to the raised height and protrusion diameter, causing the laminar sub-layer to split and amplify flow disturbance. As, the protrusion height increases, its penetrate deeper into the core flow and promote separation of the laminar sub-layer. This separation leads to production of more secondary stream flow, which increases flow reattachment at the absorber plate surface. A higher reattachment point with the absorber plate increases the heat augmentation. Also, Nu is observed to elevate with a higher value of Re because of increased high kinetic energy vortex formation in the sub-layer zone. Nu's maximum value is 182.63, corresponding to e_c/D_h = 0.067 and Re=21700. Figure 5.8 depicts the influence of e_c/D_h on f_f. The trend variation of f_f shows an increment with an increase in e_c/D_h. The rise in e_c/D_h causes an intensification of flow separation in the mainstream, promoting a directional pressure drop. The protrusion height acts as a physical obstruction to the down-flow stream, generating higher wall shear stresses and thereby enhancing the pressure drop across the duct. This results in more frictional resistance, especially at lower Reynolds numbers where viscous effects dominate. Lower frictional resistance is at lower Re and e_c/D_h. The highest friction factor is 0.072, at e_c/D_h = 0.067 and Re=3600

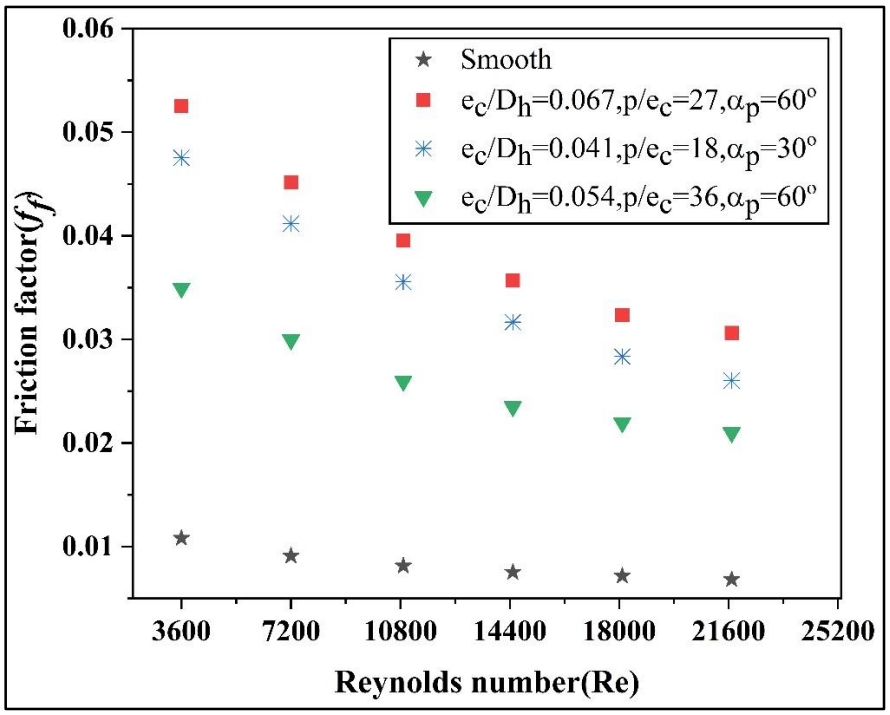

Figure 5.6 : Effect of Reynolds number on f_f.

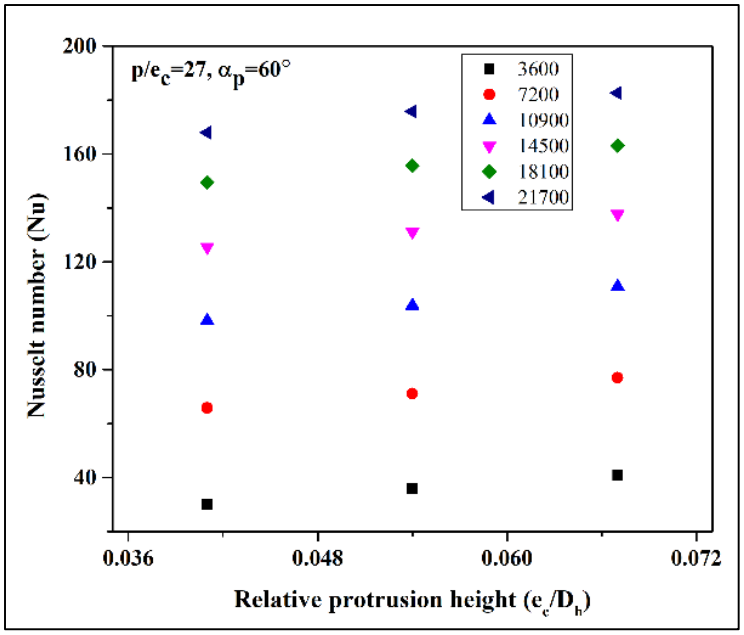

Figure 5.7 : Influence of e_c/D_h on Nu.

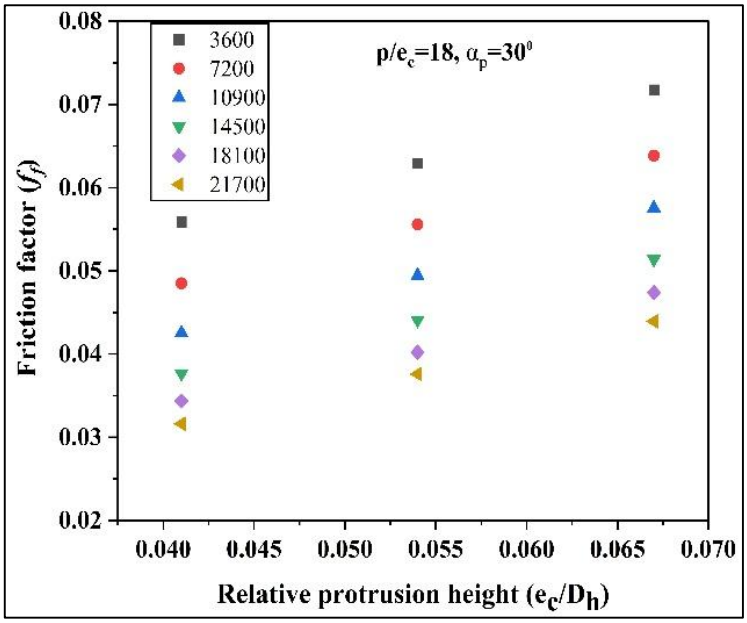

Figure 5.8 : Influence of e_c/D_h on f_f.

5.4.iii Influence of comparative pitch (p/e_c)

The influence of comparative pitch (p/e_c) on Nu and f_f with changing Reynolds numbers from 3600 to 21700 are presented. Three values of p/e_c, i.e., 18, 27, and 36, are taken. Figure 5.9 shows that Nu initially increased, reached the highest value at p/e_c of 27, and then decreased. This variation is due to the aerodynamic behaviour of the flow and protrusion spacing. At a p/e_c of 18, the protrusions are closely spaced, that is lead to congested vortex formation with early suppression of downstream eddies, resulting in less effective disruption of boundary layer and heat augmentation. At a p/e_c of 27, a conducive environment exists for cross-flow interactions, flow separation, and downstream re-attachment. The flow behaviour associated with this configuration promotes turbulent mixing, thereby enhancing heat transfer. The recirculating vortices generated by the protrusions are amplified at a p/e_c of 27, which effectively disrupts the thermal boundary layer and elevates the value of Nu. However, a further increase in p/e_c adheres to less re-circulation and re-attachment of air due to fewer protrusions. lower protrusion reduces the overall downstream obstruction, resulting in a decrease in vortex generation and less re-circulation and re-attachment of air. Therefore, p/e_c of 27 delivers the highest Nu. Extremum Nu is 182.63, corresponding to p/e_c 27. The impact of comparative pitch (p/e_c) on friction factor (f_f) is illustrated in Figure 5.10. It can be seen that the friction factor decreases with increasing relative pitch; this is due to a decrease in flow resistance and pressure drop as the number of protrusions decreases. An increase in relative pitch results in a greater spacing between the protrusions, thereby reducing the number of protrusions

encountered along the airflow path. Consequently, the presence of fewer obstructions decreases turbulence and flow interference, which in turn leads to a reduction in frictional losses. A higher density of protrusions at p/e_c of 18 and Re of 3600, creates a large flow resistance with frequent turbulence generation and surface interaction, causing elevation in highest value of f_f. On the other hand, the wide spacing between protrusions at p/e_c of 36, minimizes flow disruption. In this case, the airflow encounters less obstructions and re-attachments of vortices with the absorber plate, which resulting lower wall share stress and pressure drop. The most elevated and lowest friction factor is at p/e_c of 18 and 36, respectively. Overall, the p/e_c also plays a critical role in determine the balance between Nu and f_f.

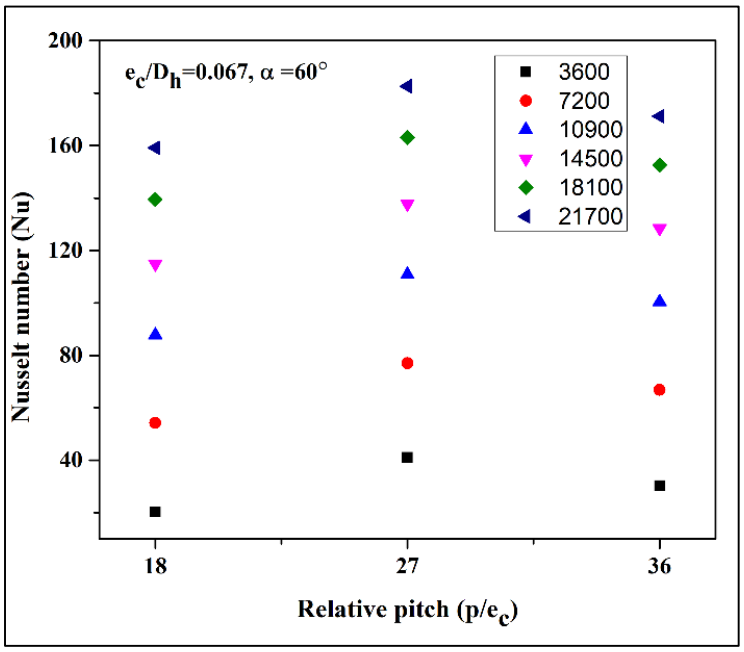

Figure 5.9 : Influence of comparative pitch (p/e_c) on Nu.

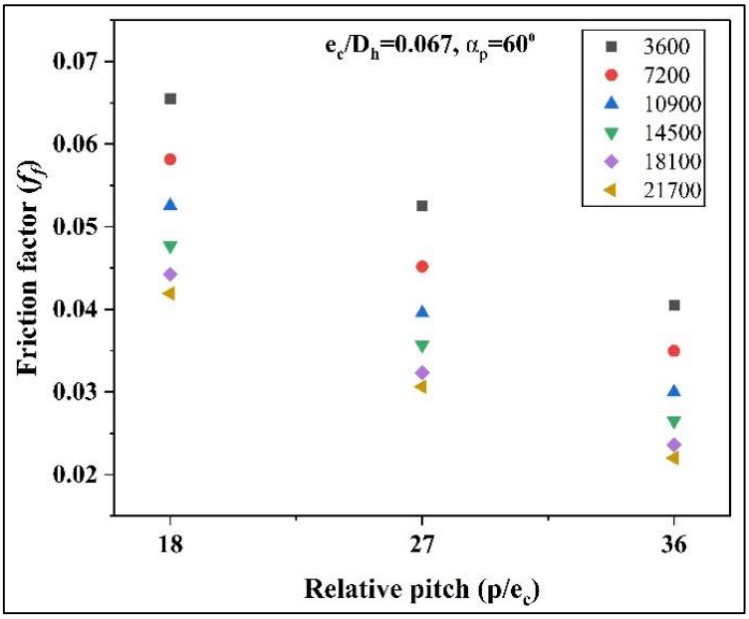

Figure 5.10 : Influence of comparative pitch (p/e_c) on f_f.

5.4.iv Protrusion angle (α_p) influence

The influence of α_p on Nu and f_f by altering Reynolds numbers from 3600 to 21700. Three values of α_p, i.e., 30º, 60º, and 90º, were used in this study. The heat augmentation increases up to α_p = 60º and then decreases, as depicted in Figure 5.11. As the protrusion angle increases from 30º to 60º, the inclination of protrusion creates more secondary flow that increases the re-attachment of the air stream at the plate surface. Furthermore, the oblique orientation of protrusions disrupts the stream's axial flow, causing a strong cross-flow motion between the primary and secondary flows. The cross-flow interaction between primary and secondary flow streams encourages vortice generation and flow impingement, which leads to the thinning of the thermal boundary layer and enhanced Nu. The further increase of α_p above 60º causes a reduction in secondary flow, re-attachment point, and less disruption of the axial flow profile, which reduces heat enhancement. The most elevated value of Nu is found at α_p=60º. The variation in f_f reduces with α_p, as illustrated in Figure 5.12. The highest and lowest frictional effects are at α_p equal to 30º and 90º, respectively. This trend is because the protrusion angle at 30º provides more obstruction as the gaps between successive protrusion are minimal and more lateral surfaces along the flow direction. Higher obstruction causes greater flow deceleration and wall share stress, leading to maximum frictional resistance and pressure drop. The protrusion angle at 90º offers minimum f_f . The vertical orientation of protrusions at α_p of 90º has minimum frontal body resistance, and more gaps between successive protrusions. This reduces the flow deceleration and wall share stress, resulting in smooth flow passage with minimal friction.

Overall, the optimal value of f_f is at α_p of 60º, because it balances the enhanced heat transfer at moderate pressure loss.

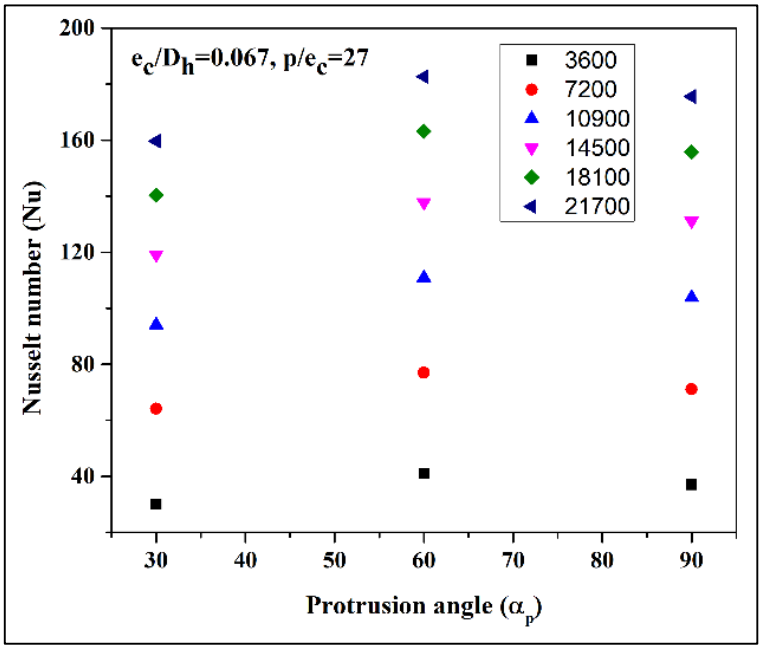

Figure 5.11 : Influence of protrusion angle (α_p) on Nu.

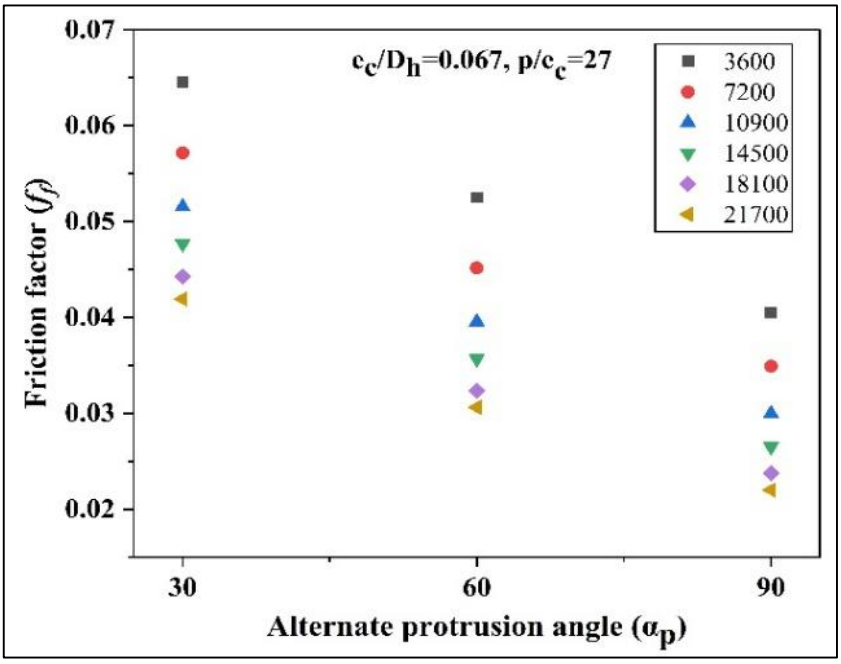

Figure 5.12 : Influence of protrusion angle (α_p) on f_f.

5.4.v Thermohydraulic Performance Index (THPi)

Solar air heater performance study means jointly determining the Nusselt number and friction factor. The protrusion on the absorber plate increases the Nusselt number and frictional losses. So, the effectiveness of protrusion roughness depends on the thermo-hydraulic performance index (THPi) as expressed in Eq. (8). THPi>1 validates the

substantial effect of roughness in heat augmentation. The variation of THPi across different configurations of semi-capsule protrusions are influenced by the combined effects of change in heat transfer increment factor (Nu/Nu_s), friction factor increments (f_f/f_s) and the inherent non-linear nature of THPi, especially under turbulent and complex flow regimes.

Figure 5.13 presents the variation of THPi with different geometric and flow conditions. It highlights an increase in THPi for all three case of e_c/D_h ratios, as the Re rises up to 10,900. Then, it becomes flat to a slight downtrend as Re grows further for all experimentation sets. This result indicates that with an increase in e_c/D_h, there is no significant change in friction factor increments (f_f/f_s) due to a lower pressure drop after Re reaches 10,900, which leads to saturation in the enhancement of THPi. The maximum THPi is 2.06, corresponding to e_c/D_h=0.067, p/e_c=27, α_p= 90º, and Re=10900.

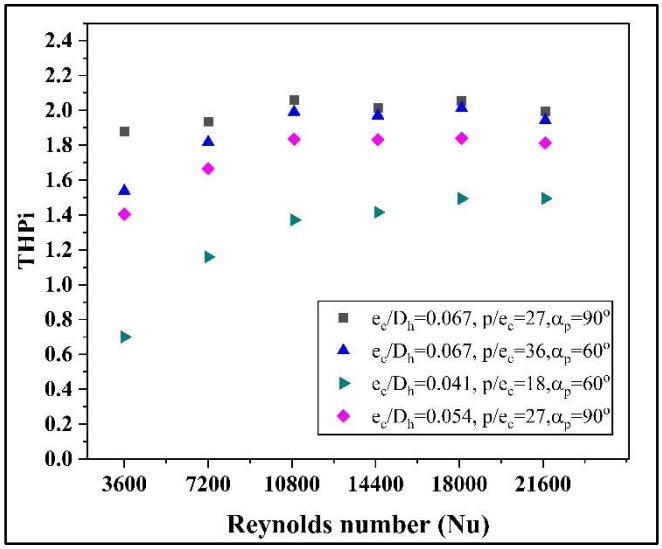

Figure 5.13 : THPi vs. Reynolds number.

5.5 Statistical correlations

The correlations are necessary for Nu and f_f obtained from the experiment, which showed a vital function with geometrical and flow parameters. They can be associated as,

$$Nu = f(Re, e_c/D_h, p/e_c, \alpha_p) \quad (5.12)$$

$$f_f = f(Re, e_c/D_h, p/e_c, \alpha_p) \quad (5.13)$$

A regression analysis based on the experimental data was developed to determine a statistical correlation for Nu and f_f parameters. Nu is plotted against Re to initiate the regression analysis, as illustrated in Figure 5.14. A functional relation obtained to fit the best line is represented as,

$$Nu = X_0 Re^{1.0271} \quad (5.14)$$

where X_0 is constant and is influenced by the other parameters, considering e_c/D_h as an influencing parameter, the value of e_c/D_h is plotted against X_0 on a logarithmic scale, and presented in Figure 5.15. The regression study for the second-order polynomials is carried out as

$$\ln(X_0) = \ln(-2.8139) + 1.2518\ln(e_c/D_h) + 0.1554(\ln(e_c/D_h)^2 \quad (5.15)$$

The above equation can further be written using Eq. (5.15) as

$$\mathrm{Nu} = X_1 Re^{1.0271}\,(e_c/D_h)^{1.2518}\,\mathrm{Exp}\,[0.1554\ln(e_c/D_h)^2] \quad (5.16)$$

In the above equation, the variable X_1 is a function that depends on p/e_c. Figure 5.16 plots a logarithmic relation between p/ec and X_1. The second-order polynomial regression provides the following expression:

$$\ln(X_1) = \ln(-21.113) + 11.2124\ln(p/e_c) - 1.7004(\ln(p/e_c)^2) \quad (5.17)$$

The above equation can be further written as

$$\mathrm{Nu} = X_2 Re^{1.0271}\,(e_c/D_h)^{1.2518}\,\mathrm{Exp}\left[0.1554\ln(e_c/D_h)^2\right](p/e_c)^{11.2124}\,Exp[-1.7004(\ln(p/e_c)^2] \quad (5.18)$$

where X_2 is a parameter and is a function of $\alpha_p/60$. The value of $\alpha_p/60$ and X_2 is depicted by a logarithmic scale, as displayed in Figure 5.17. The regression analysis gives a second-order polynomial as

$$\ln(X_2) = \ln(-21.165) - 0.0146\ln(\alpha_p/60) - 0.4333(\ln(\alpha_p/60)^2 \quad (5.19)$$

The above equation can be used to determine Nu as

$$\mathrm{Nu} = X_3 Re^{1.0271}\,(e_c/D_h)^{1.2518}\,\mathrm{Exp}\left[0.1554\ln(e_c/D_h)^2\right](p/e_c)^{11.2124}$$
$$Exp\left[-1.7004(\ln(p/e_c)^2\right](\alpha_p/60)^{-0.0146}\mathrm{Exp}[-0.4333(\ln(\alpha_p/60)^2)] \quad (5.20)$$

where X_3 is a constant, and X_3=6.4292×10^{-10}.

The final correlation of Nu is obtained as,

$$\mathrm{Nu} = 6.4292\times10^{-10} Re^{1.0271}\,(e_c/D_h)^{1.2518}\,\mathrm{Exp}\left[0.1554\ln(e_c/D_h)^2\right](p/e_c)^{11.2124}$$
$$Exp\left[-1.7004(\ln(p/e_c)^2\right](\alpha_p/60)^{-0.0146}\mathrm{Exp}[-0.4333(\ln(\alpha_p/60)^2)] \quad (5.21)$$

Similarly, the regression analysis is performed in Figure 5.18-Figure 5.21. The statistical correlation for f_f is derived as

$$f_f = 0.294876 \times Re^{-0.305} \, (e_c/D_h)^{2.4893} \, \mathrm{Exp}\left[0.3207 \ln(e_c/D_h)^2\right](p/e_c)^{4.0739}$$

$$Exp\left[-0.7543(\ln(p/e_c)^2\right](\alpha_p/60)^{-0.5594}\mathrm{Exp}[-0.3445(\ln(\alpha_p/60)^2)] \quad (5.22)$$

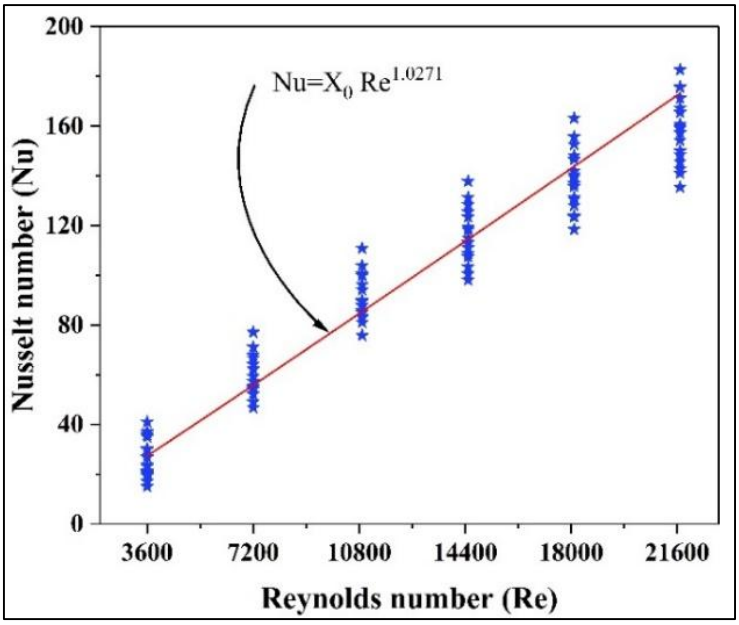

Figure 5.14 : Variation of Nu as a function of Re.

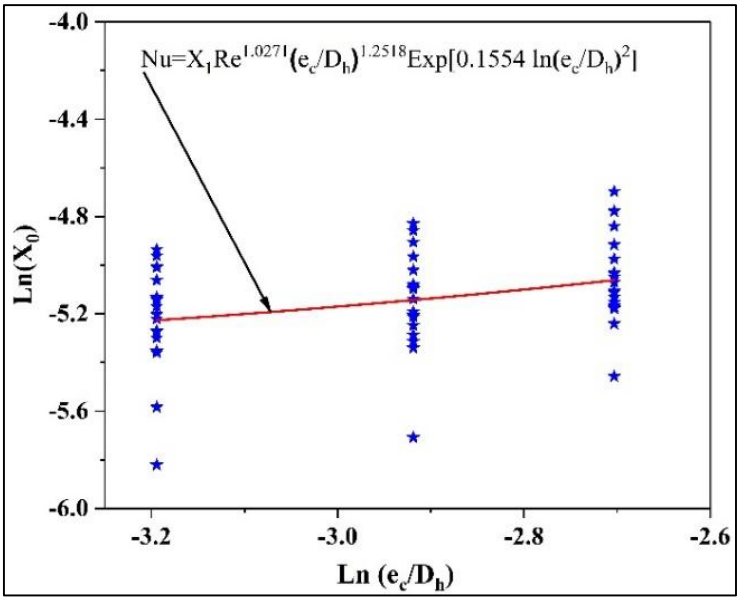

Figure 5.15 : Logarithmic plotting between Xo and e_c/D_h.

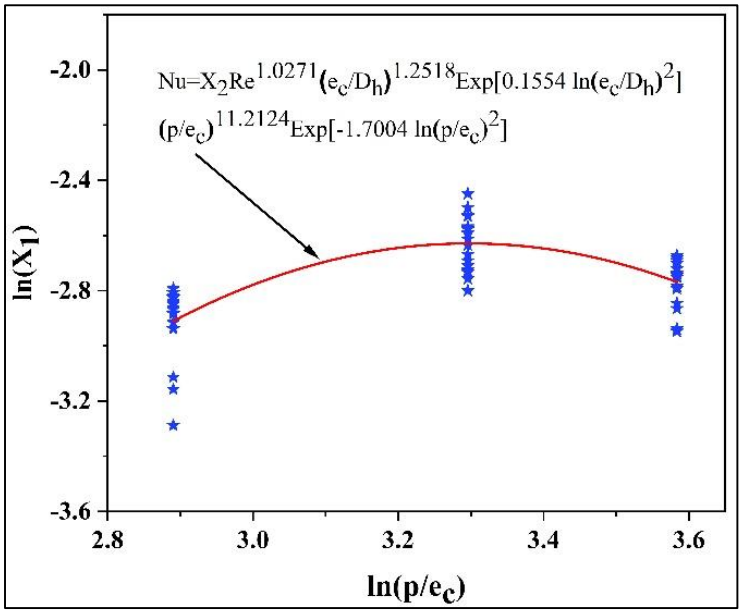

Figure 5.16 : Logarithmic variation of X_1 and p/e_c.

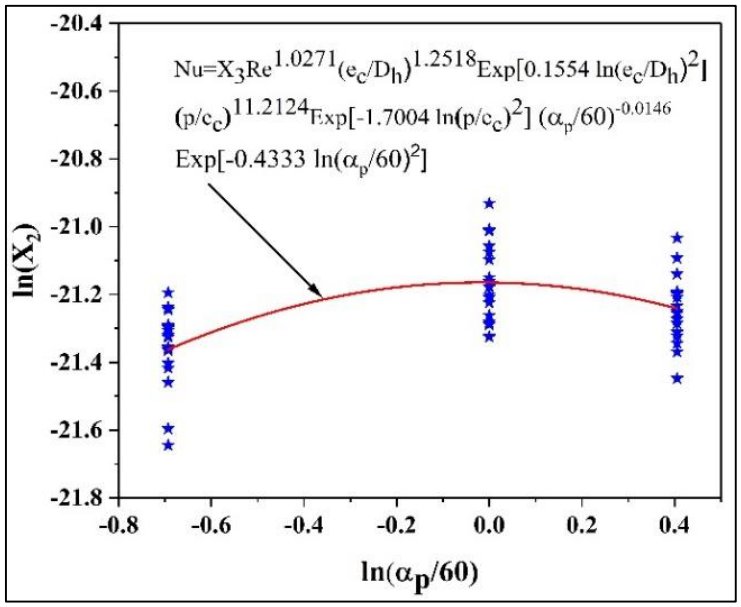

Figure 5.17 : Logarithmic plotting of X_2 and $\alpha_p/60$.

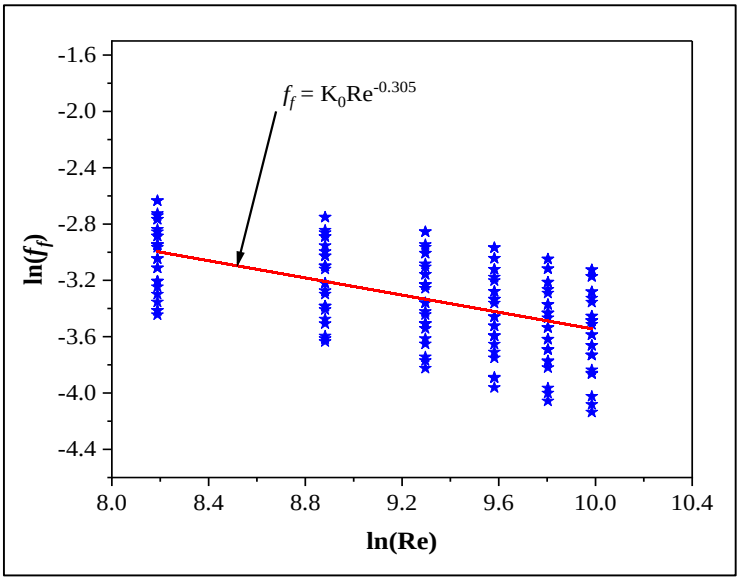

Figure 5.18 : Plotting in log scale of f_f and Re.

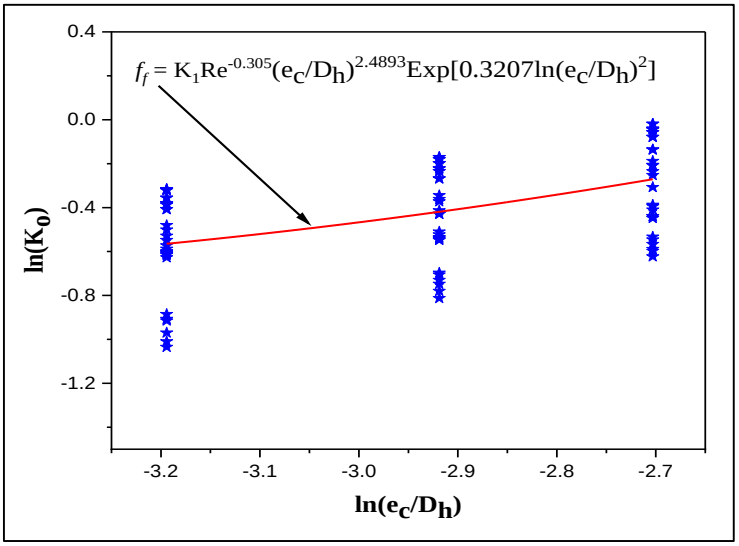

Figure 5.19 : Variation of Ko and e_c/D_h in log scale.

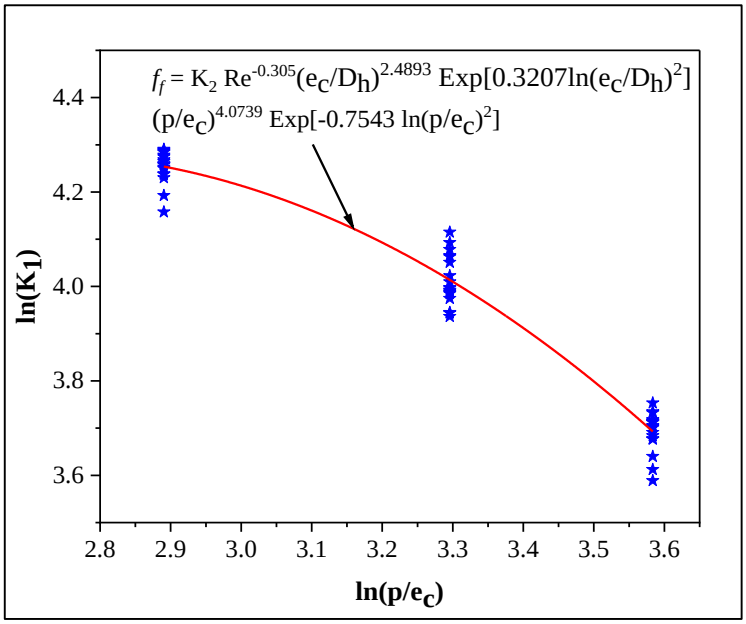

Figure 5.20: Variation of K_1 and p/e_c in log scale.

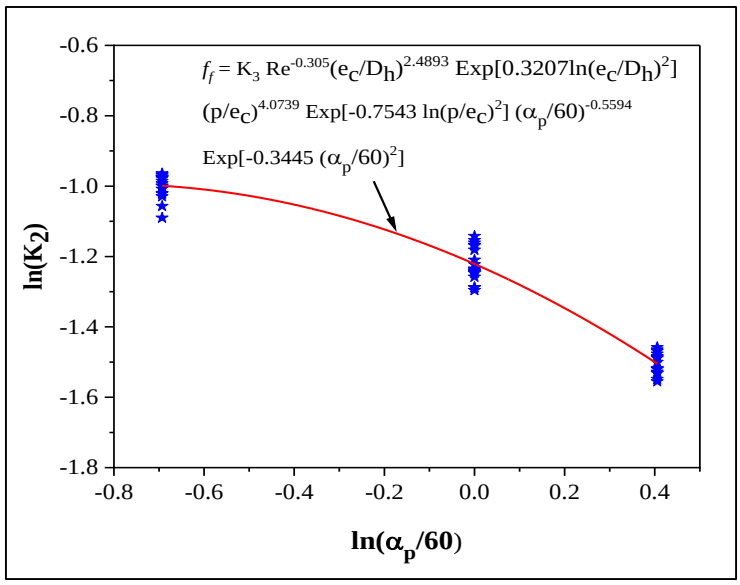

Figure 5.21 : Variation of K_2 and $\alpha_p/60$ in log scale.

5.6 Performance Comparison

The statistical correlations (Eq. 5.21-5.22) for Nu and f_f give results that compare with the experimental values depicted in Figure 5.22. The noted mean absolute percentage error (MAPE) for Nu and f_f are ±9.19% and ±3.26%, respectively. Most data sets lie within the 95% prediction band, confirming the accuracy of developed statistical correlations. Therefore, this deviation justifies good agreements and an acceptable limit with the coefficient of determination (R-Square) values for Nu and f_f are 0.97145 and 0.98136, respectively. Also, a comparative study is conducted among the obtained thermo-hydraulic performance index and the studies available for different roughness, and it is plotted in

Figure 5.23. The proposed new air heater exhibits an improvement in THPi compared to the cited literature. From figure, it can be observed that the present study with semi-capsule protrusions provided a consistent THPi varied from 1.87 to 2.06 across the range of Re. Unlike hemispherical cavity with sharp drop of THPi with increase in Re and a limited gain of THPi in the case of cylindrical/ stepped cylindrical/ cubical, semi-capsule protrusions offers an effective balance between heat transfer and friction loss. These trade-offs with cited roughness confirm a practical applicability with sustained improvements in THPi, making the proposed solar air heater with semi-capsule protrusions superior for real-world solar air heating systems.

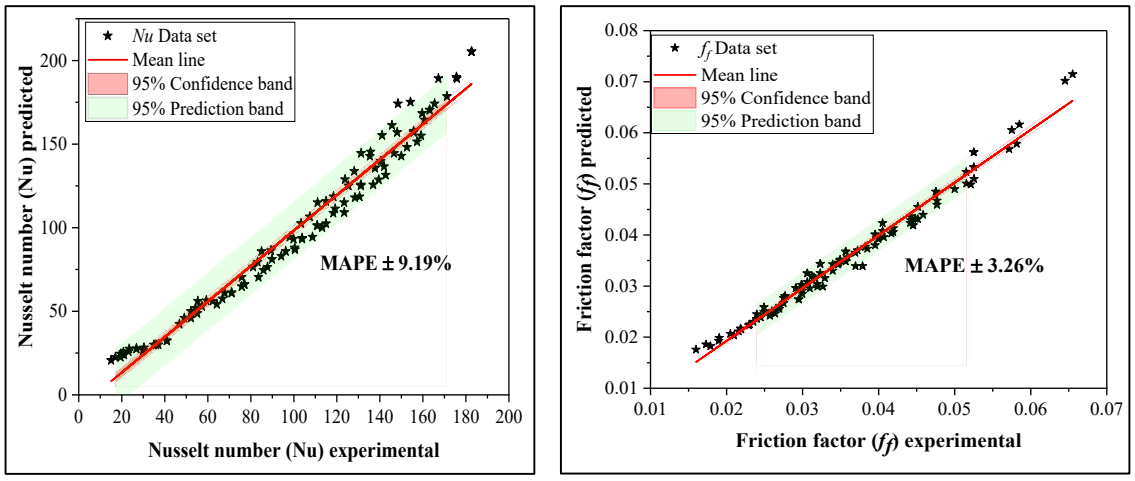

(a) **(b)**

Figure 5.22: Comparisons of experimental and correlation results for (**a**) Nu and (**b**) f_f.

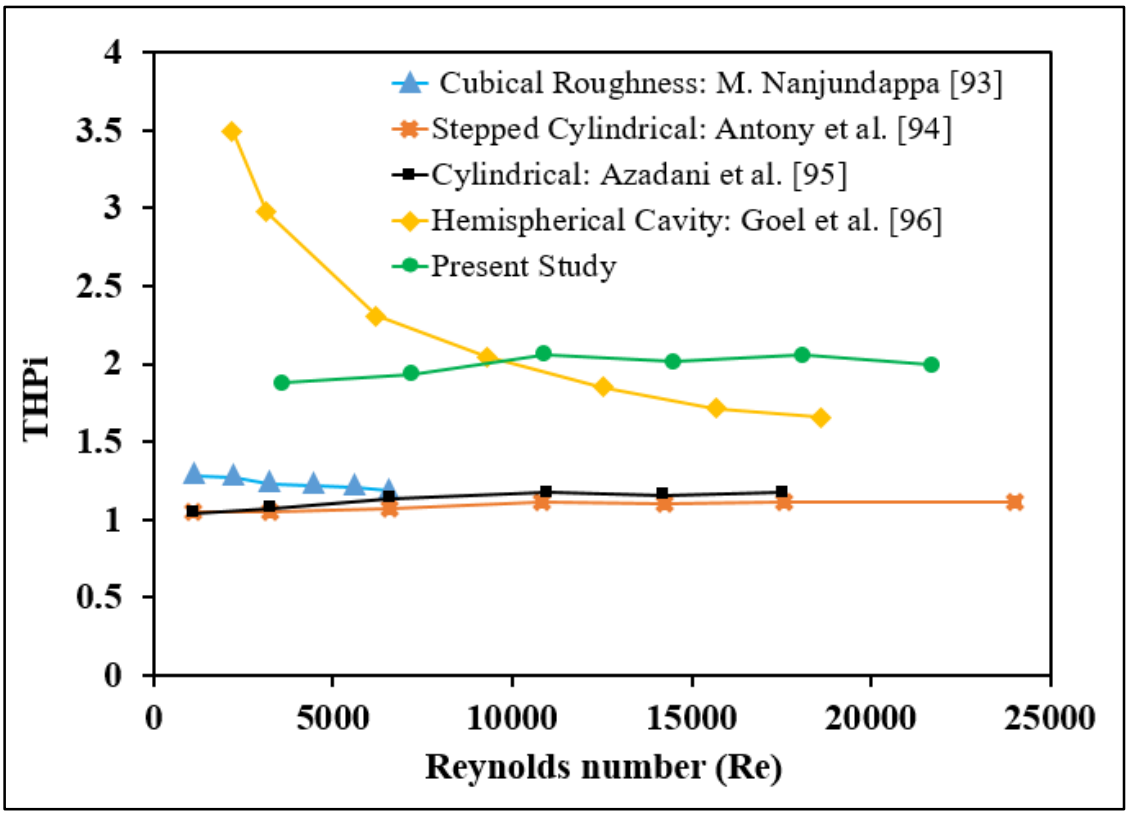

Figure 5.23: THPi comparisons of semi-capsule protrusion with existing roughness [93],[94],[95],[96].

5.7 Optimization

Correlation equations expressed in Eqs. (5.21) and (5.22) for Nu and f_f are employed in single and multi-objective optimization using metaheuristic optimization techniques. The highest Nu or lowest f_f are the objective function in single-objective optimization considering the constraints of Re, e_c/D_h, p/e_c, and α_p. The range of constraints is considered in The range of constraints is considered in Table 5.1. Five sets of runs with 100 iterations were performed to check the consistency of each algorithm in single objective optimization, and Table 5.4. provides the final results. The results depict the WOA generated superior output for both objectives with minimum variability and standard deviation. The GWO provided a very close output to the WOA. Also, Figure 5.24(a) and (b) exhibit information on Nusselt number and friction factor convergence to check each algorithm's computational efficacy. The convergence plot shows the computational effort made during each iteration until it reaches the best solution. The convergence plot indicates that the WOA converges towards the best solutions with a faster rate and the least computational effort. Hence, it can be concluded that the WOA metaheuristic optimization outperformed GWO, GOA, ACO and DA.

Table 5.4 : Outcomes of single-objective optimization

Objective Function	Meta-heuristic algorithms	Mean	St.Dev	Output	Parametric settings of Geometric and flow parameters			
					Re	e_c/D_h	p/e_c	α_p
Nu (Max.)	GWO	205.63	0.001	205.63	21700	0.07	27.05	58.87
	WOA	205.64	0	205.64	21700	0.07	27.03	58.97
	GOA	195.56	11.84	193.10	21700	0.06	27.03	59
	ACO	199.92	1.26	200	21489	0.07	26.76	65.99
	DA	196.83	5.23	192.32	21700	0.070	24.54	82.71
f_f (Min.)	GWO	0.013	0	0.013	21700	0.04	36	90
	WOA	0.013	0	0.013	21700	0.04	36	90
	GOA	0.013	0	0.013	21700	0.04	36	90
	ACO	0.015	0.001	0.014	21205	0.04	35.92	86.31
	DA	0.015	0.002	0.013	21700	0.040	36	90

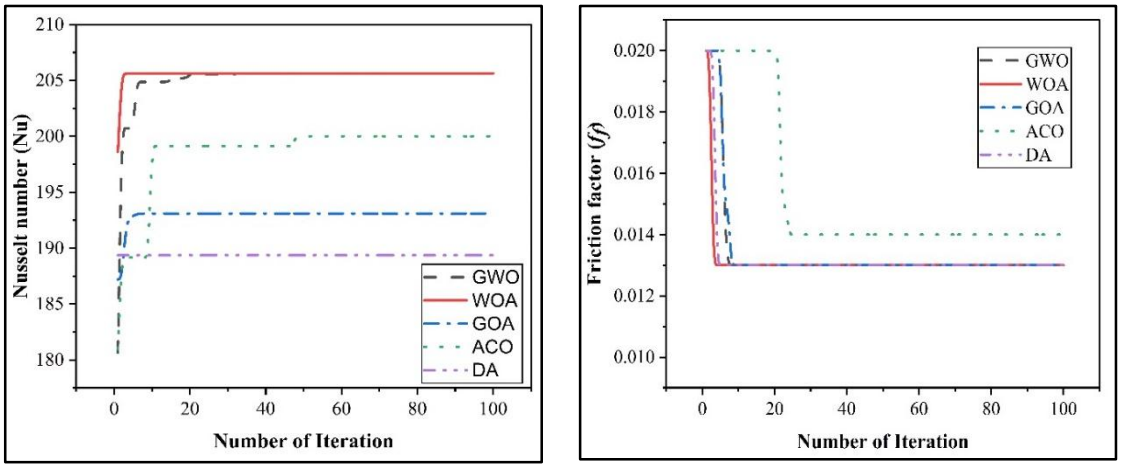

(a) **(b)**

Figure 5.24 : Convergence plot for: (**a**) Nu, and (**b**) f_f.

Table **5.4** shows the unequal parametric settings for both objectives, making it unfeasible to apply them simultaneously. So, finding a single parametric setting for better optimal Nu and f_f, simultaneously using multi-objective optimization, is necessary. Metaheuristic algorithms work better in this scenario than aggregation-based optimization methods. Hence, Pareto multi-objective meta-heuristic optimization was performed, and several compromise optimal solutions were generated using GWO, WOA, GOA, ACO, and DA metaheuristic algorithms. One hundred fifty search agents and 500 interns were involved in identifying the compromise optimal solutions. Figure 5.25-Figure 5.29 displays the Pareto front of compromised solutions, and its range is provided in Table 5.5.

From the Pareto front, it is clear that all the algorithms have put effort into the search for a total of 150 non-dominated optimal solutions. However, the maximum number of non-dominated solutions given by WOA have fallen in the best compromise zone, i.e., 50% zone. So, the WOA has performed better than other algorithms. The Pareto multi-objective optimization is limited, as it cannot produce single solutions. The suitable parameters can be chosen per the objective function's priority, meaning the Nu does not maximize at lower f_f. So, a decision maker can select an optimum parametric setting for Nu and f_f.

Table 5.5 : Optimum range for Nu and f_f using Pareto multi-objective optimization.

Meta-heuristic algorithms	Optimal Range	Output		Parametric settings of Geometric and flow parameters			
		Nu	f_f	*Re*	e_c/D_h	p/e_c	α_p
GWO	Upper	205.52	0.034	21700	0.067	26.62	57.98
	Lower	142.46	0.014	21700	0.043	36	90
WOA	Upper	205.15	0.031	21700	0.067	27.45	63.11
	Lower	140.88	0.013	21700	0.041	35.94	89.76
GOA	Upper	203.93	0.030	21700	0.067	28.51	64.34
	Lower	155.15	0.016	21700	0.057	36.00	90
ACO	Upper	204.77	0.031	21700	0.067	27.94	63.51
	Lower	144.23	0.014	21700	0.041	35.06	90
DA	Upper	204.99	0.031	21700	0.067	27.94	62.28
	Lower	144.64	0.014	21700	0.041	34.85	90

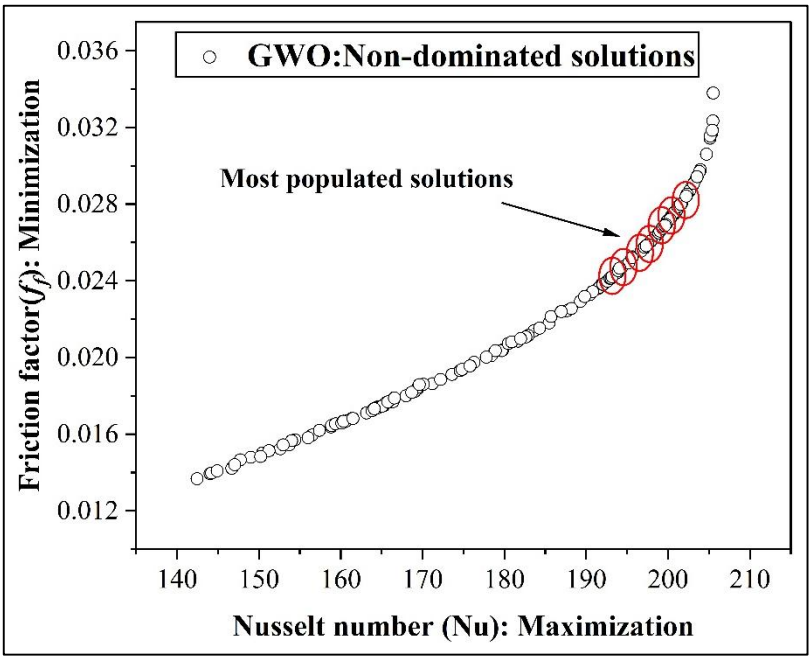

Figure 5.25 : Pareto front of GWOPareto front of GWO

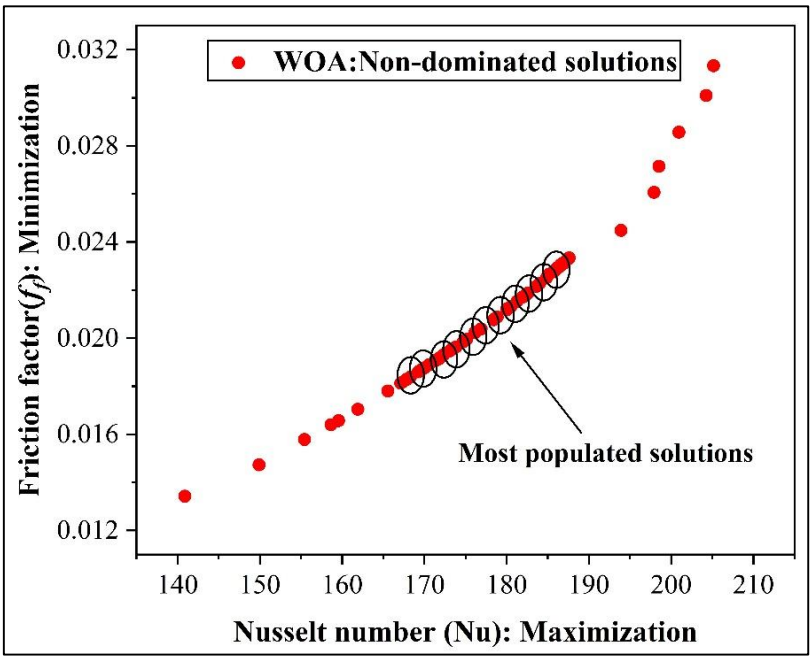

Figure 5.26: Pareto front of WOA

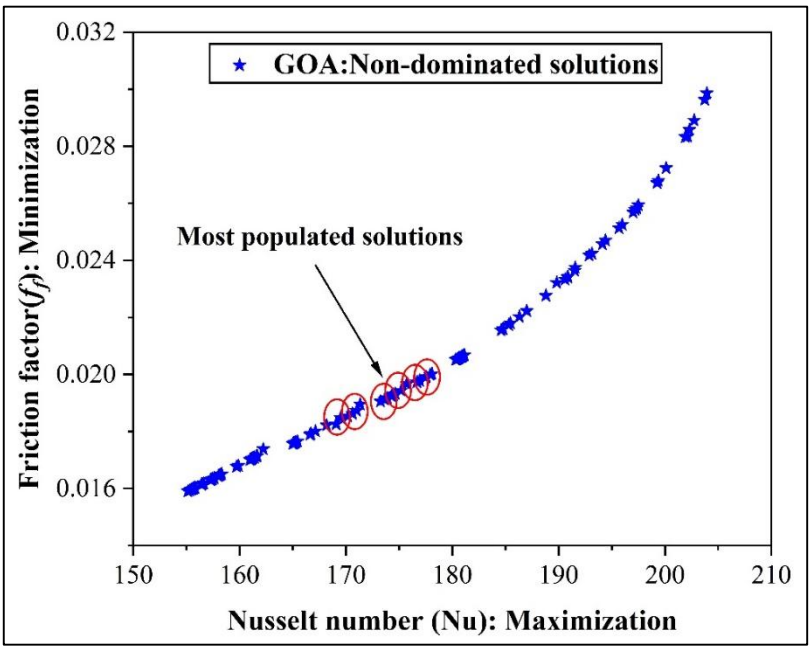

Figure 5.27 : Pareto front of GOA

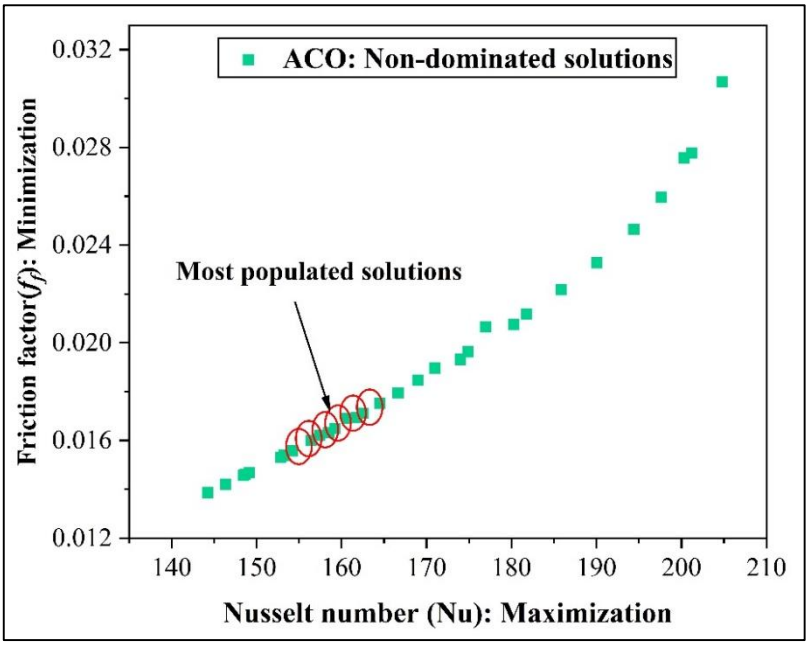

Figure 5.28 : Pareto front of ACO

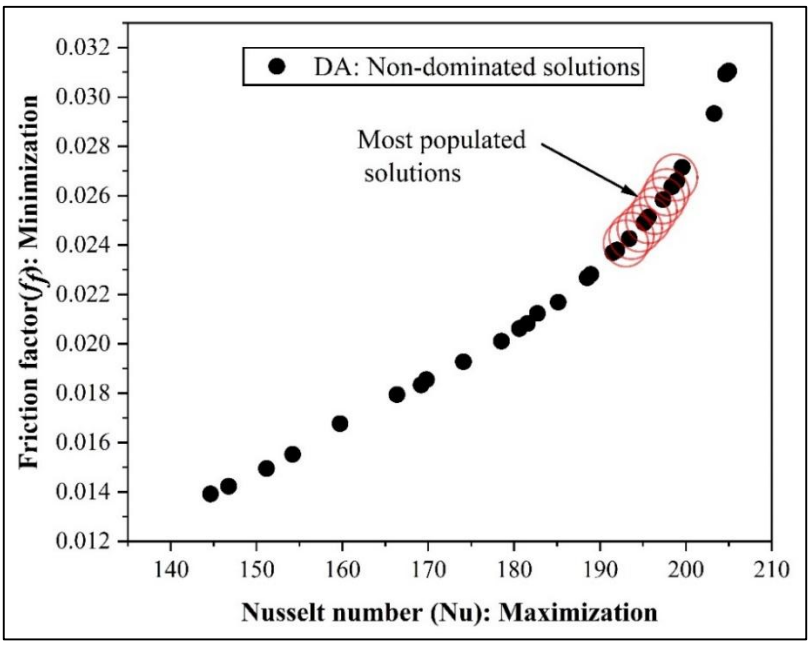

Figure 5.29 : Pareto front of DA

5.8 Conclusions

A new artificial roughness, as semi-capsule-shaped protrusions in a staggered pattern, has been proposed in the presented work. This arrangement aims to increase heat augmentation by suppressing the laminar sub-layer. Three geometrical parameters, i.e., relative height (e_c/D_h) =0.041-0.067, relative pitch (p/e_c) =18-36, and protrusion angle (α_p) = 30^o-90^o, were considered in different sets of experimentations. The flow parameter (Re) is varied from 3600 to 21700 in each observation. Leveraging the experimental data,

regression analysis establishes correlations for Nu and f_f separately. Also, metaheuristic optimization algorithms, namely GWO, WOA, GOA, ACO, and, DA, are developed for single and multi-objective optimization.

The current study draws the following substantial conclusions:

i. The highest Nusselt number (Nu) is 182.62, corresponding to e_c/D_h=0.067, p/e_c=27, α_p= 60º, and Re=21700. The highest enhancement in heat augmentation is 3.14 times compared to a conventional heater.
ii. The extremum friction (f_f) is 0.073, at e_c/D_h=0.067, p/e_c=18, α_p= 30º, and Re=3600. The most incremented friction is 6.66 times compared to a conventional heater.
iii. The optimum THPi is 2.06, corresponding to e_c/D_h=0.067, p/e_c=27, α_p= 90º, and Re=10900.
iv. Statistical correlations for Nu and f_f are developed and exhibited a satisfactory prediction with MPAE of ±9.19%, and ±3.26% respectively.
v. Compared to GWO, GOA, ACO, and DA; the WOA produces the best optimal solutions in optimization studies.

5.9 Summary

This chapter deals with the implementation of semi-capsule-shaped protrusions in a staggered pattern as roughness. Three geometric parameters, i.e., relative height, relative pitch, and protrusion angle of attack, were considered in different sets of experimentations, with a range of Reynolds number as a flow parameter. The effects of these parameters have been studied on the thermo-hydraulic performance. Nusselt number, friction factor and thermo-hydraulic performance index were the main outputs. Algebraic correlations for the Nusselt number and friction factor are developed. A single and multi-objective optimization has been performed using Five swarm intelligence-based metaheuristic algorithms, namely Grey Wolf optimization (GWO), Whale optimization algorithm (WOA), Grass-hopper optimization algorithm (GOA), Ant colony optimization (ACO), and Dragonfly algorithm(DA). The comparative optimization capability of their algorithms has been explored.

CHAPTER 6

CONCLUSIONS, LIMITATIONS AND SUGGESTIONS FOR FUTURE WORK

Preface

This chapter summarized the outcomes and limitations of this research work and proposed the future scope.

6.1 Introduction

This research work focused on implementing artificial roughness as dimples/protrusions on the absorber plate of solar air heater to improve thermo-hydraulic performance. Different metaheuristic optimization algorithms have also been employed for single and multi-objective optimization. Three research problems have been addressed in this work and are presented in chapters 3-5.

- **Problem 1** in Chapter 3 detailed the parametric optimization of solar air heaters with dimples in straight-line patterns and zig-zag patterns on absorber plates using metaheuristic approaches.
- **Problem 2** in Chapter 4 focused on the experimental and metaheuristic optimization for the highest thermo-hydraulic performances of a solar air heater with a V-notch pattern of hemispherical protrusions on absorber surfaces.
- **Problem 3** in Chapter 5 focused on experimental and metaheuristic optimization study on the effect of semi-capsule protrusions on the performance of solar air heater.

The previous chapters focus on the objectives of each research problem presented in the thesis. The analysis of each problem's results is thoroughly discussed in chapters 3-5 respectively. To provide a more complete overview of the study, the key findings are summarized below:

6.2 Overall Conclusions of this Research Work

In this research work the effects of dimples and protrusions as artificial roughness on the absorber plate of solar air heater has been addressed. The broad spectrum of this research is represented by the shape, size, and patterns of the dimples and protrusions as geometric influencing parameters and the Reynolds number as a flow parameter. The effects of these geometric and flow parameters on the thermo-hydraulic performance of solar air heater has been addressed.

The broad conclusions drawn from each problem are summed up as follows:

6.2.i Problem 1

a. In single objective optimization of solar air heater having dimples in a zig-zag pattern, the TLBO metaheuristics algorithm exhibited better results than the other three algorithms. The maximum value of Nusselt number was obtained to be 214.2550 concerning Re=20000, P_S/e=27.0691, P_I/e =30.1565, and d/D=0.2670, and the minimum value of friction factor was obtained to be 0.010606 at Re=20000, P_S/e=37.50, P_I/e =37.50, and d/D=0.1470. In multi-objective optimization, the suitable geometric and flow parameters parameter were found to be Re = 20000, P_S/e = 30.83, P_I/e = 30.83, and d/D = 0.2515 for the optimal value of Nusselt number and friction factor of 204.7034 and 0.0134 respectively.
b. In a single objective optimization of a solar air heater having dimples in a straight-line pattern, the TLBO metaheuristics algorithm demonstrated better results than the other three algorithms. The maximum value of Nusselt number was obtained to be 107.7515 at Re=20000, p/e =12, e/D =0.0377, and the minimum value of F_f was obtained to be 0.0237 at Re=11976, p/e =12, e/D =0.0379. In multi-objective optimization, the suitable geometric and flow parameters were found as Re = 12000, p/e= 12, and e/D = 0.0379 for the optimal values of Nusselt number and friction factor as108.6901 and 0.0237, respectively.
c. The TLBO metaheuristics algorithm outperformed over other three metaheuristics algorithms in terms of accuracy with low variability and minimal computational effort as observed from the t-test and convergent diagram.

6.2.ii Problem 2

a. The highest value of THPP was observed as 1.60 at p_p/h_p =10, h_p/D_h=0.050, α_{ap} =60^0, and Re =7200.

b. The maximum value of Nusselt number is 127.07 at h_p/D_h=0.050, p_p/h_p =10 $\alpha_{ap}=60^0$, and Re=21700.
c. The minimum value of friction factor is 0.0165 at h_p/D_h=0.027, p_p/h_p =10, $\alpha_{ap}=45^0$, and Re=21700.
d. Statistical correlations for Nusselt number and friction factor are developed, which exhibited a satisfactory prediction with average deviation of ±12.38% and ±10.71%, respectively.
e. In both the cases of single and multi-objective optimization, the WOA metaheuristic algorithm outperformed over other considered metaheuristic algorithms.

6.2.iii Problem 3

a. The highest Nusselt number is 182.62, corresponding to e_c/D_h=0.067, p/e_c=27, α_p= 60º, and Re=21700. The highest enhancement in heat augmentation is 3.14 times compared to a conventional heater.
b. The extremum friction factor is 0.073, at e_c/D_h=0.067, p/e_c=18, α_p= 30º, and Re=3600. The most incremented friction is 6.66 times compared to a conventional heater.
c. The optimum THPi is 2.06, corresponding to e_c/D_h=0.067, p/e_c=27, α_p= 90º, and Re=10900.
d. Statistical correlations for Nusselt number and friction factor are developed and exhibited a satisfactory prediction with MPAE of ±9.19%, and ±3.26% respectively.
e. Compared to GWO, GOA, ACO, and DA, the WOA produces the best optimal solutions in optimization studies.

6.3 Comprehensive comparison of the performance across the three problems

a. The solar air heater with dimples in a V-notch pattern shows improved results compared to dimples in straight-line and zig-zag patterns, because of effective roles of V-notch angle of attack. The V-notch pattern offers an optimum hindrance of air in diagonal directions with minimum drag at inlet, leading to enhanced secondary flow formation, vortex generation and flow impingement. The V-notch wings also promote strong longitudinal and diagonal vortices, which helps in disrupting the thermal and laminar sub-layer.

b. The highest thermohydraulic performance was observed in artificial roughness in the form of semi-capsule protrusions in a staggered pattern. The oblique orientation of protrusions disrupts the stream's axial flow, resulting in a strong cross-flow interaction between the primary and secondary flows. This interaction promotes vortice generation and flow impingement, which thins the thermal boundary layer and increases the heat augmentation.
c. In single and multi-objective optimization, TLBO and WOA have delivered better optimal solutions than other metaheuristic algorithms. These two algorithms converged to the best solutions more rapidly and with less computational effort compared to the other algorithms. These two algorithms stand out not only for exceptional computational performance but also for their balanced approach to exploration and exploitation. Also, their capability to prevent premature convergence and robustness in handling nonlinear, multi-dimensional problems, make them successful navigation to the best optimal solutions.

6.4 Limitations

a. The study was conducted in defined range of flow and geometric parameters due to physical and fabrication constraints.
b. The flow dynamics were not validated using computational fluid dynamics techniques and the analysis was based on experimental and analytical results.
c. The results were not validated under transient heat flux conditions or different geographical locations, which may influence the performance of solar air heaters.

6.5 Suggestions for Future Work

Despite the notable progress made in developing solar air heaters, the current research has generated several new research questions that should be explored in future studies. It is recommended that this research be expanded in the following directions:

a. Study on the combined effects of semi-capsule protrusions and hemi-spherical dimples as artificial roughness in solar air heater.
b. Performance evaluation of simple solar dryer coupled with solar air heater having semi-capsule protrusions.
c. The hybrid version of employed metaheuristic algorithms can be applied for the optimization of geometric and flow parameters.

Appendix A

Measurement uncertainty of various parameters is as follows:

1. Cross-section area of duct and area of absorber plate:

$$\frac{\delta A_d}{A_d} = \left[\left(\frac{\delta H}{H}\right)^2 + \left(\frac{\delta W}{W}\right)^2\right]^{\frac{1}{2}} \quad \text{(A1)}$$

$$\frac{\delta A_p}{A_p} = \left[\left(\frac{\delta L}{L}\right)^2 + \left(\frac{\delta W}{W}\right)^2\right]^{\frac{1}{2}} \quad \text{(A2)}$$

2. Hydraulic diameter:

$$\frac{\delta D_h}{Dh} = \frac{\left[\left(\frac{\delta D_h \delta W}{W}\right)^2 + \left(\frac{\delta D_h \delta H}{H}\right)^2\right]^{\frac{1}{2}}}{[2(W\times H)(W+H)^{-1}]} \quad \text{(A3)}$$

3. Air density (ρ):

$$\frac{\delta \rho}{\rho} = \left[\left(\frac{\delta P_a}{P}\right)^2 + \left(\frac{\delta T_O}{T_O}\right)^2\right]^{\frac{1}{2}} \quad \text{(A4)}$$

4. Mass flow rate of air (m):

$$\frac{\delta m}{m} = \left[\left(\frac{\delta \rho}{\rho}\right)^2 + \left(\frac{\delta A_d}{A_d}\right)^2 + \left(\frac{\delta V}{V}\right)^2\right]^{\frac{1}{2}} \quad \text{(A5)}$$

5.Reynolds number (Re):

$$\frac{\delta Re}{Re} == \left[\left(\frac{\delta \rho}{\rho}\right)^2 + \left(\frac{\delta V}{V}\right)^2 + \left(\frac{\delta D_h}{D_h}\right)^2 + \left(\frac{\delta \mu}{\mu}\right)^2\right]^{\frac{1}{2}} \quad \text{(A6)}$$

6. Useful heat gain (Q_u):

$$\frac{\delta Q_u}{Q_u} = \left[\left(\frac{\delta m}{m}\right)^2 + \left(\frac{\delta C_p}{C_p}\right)^2 + \left(\frac{\delta \Delta T}{\Delta T}\right)^2\right]^{\frac{1}{2}} \quad \text{(A7)}$$

7. Convective heat transfer coefficient (*h*):

$$\frac{\delta h}{h} = \left[\left(\frac{\delta Q_u}{Q_u}\right)^2 + \left(\frac{\delta A_p}{A_p}\right)^2 + \left(\frac{\delta \Delta T_m}{\Delta T_m}\right)^2\right]^{\frac{1}{2}} \quad \text{(A8)}$$

8. Nusselt number (Nu):

$$\frac{\delta Nu}{Nu} = \left[\left(\frac{\delta h}{h}\right)^2 + \left(\frac{\delta D_h}{D_h}\right)^2 + \left(\frac{\delta k}{k}\right)^2\right]^{\frac{1}{2}} \quad \text{(A9)}$$

9.Friction factor (*f*):

$$\frac{\delta f}{f} = \left[\left(\frac{\delta \Delta P}{\Delta P}\right)^2 + \left(\frac{\delta D_h}{D_h}\right)^2 + \left(\frac{\delta \rho}{\rho}\right)^2 + \left(\frac{\delta L}{L}\right)^2 + \left(\frac{\delta V}{V}\right)^2\right]^{\frac{1}{2}} \quad \text{(A10)}$$

REFERENCES:

[1] J. Dar and M. Asif, "Environmental feasibility of a gradual shift from fossil fuels to renewable energy in India: Evidence from multiple structural breaks cointegration," *Renew. Energy*, vol. 202, pp. 589–601, Jan. 2023, doi: 10.1016/J.RENENE.2022.10.131.

[2] C. Yu, M. Moslehpour, T. K. Tran, L. M. Trung, J. P. Ou, and N. H. Tien, "Impact of non-renewable energy and natural resources on economic recovery: Empirical evidence from selected developing economies," *Resour. Policy*, vol. 80, p. 103221, Jan. 2023, doi: 10.1016/J.RESOURPOL.2022.103221.

[3] A. Sharma, C. R. Chen, and N. Vu Lan, "Solar-energy drying systems: A review," *Renew. Sustain. Energy Rev.*, vol. 13, no. 6–7, pp. 1185–1210, Aug. 2009, doi: 10.1016/J.RSER.2008.08.015.

[4] S. K. Pathak *et al.*, "Energy, exergy, economic and environmental analyses of solar air heating systems with and without thermal energy storage for sustainable development: A systematic review," *J. Energy Storage*, vol. 59, p. 106521, Mar. 2023, doi: 10.1016/J.EST.2022.106521.

[5] A. Saxena, Varun, and A. A. El-Sebaii, "A thermodynamic review of solar air heaters," *Renew. Sustain. Energy Rev.*, vol. 43, pp. 863–890, Mar. 2015, doi: 10.1016/J.RSER.2014.11.059.

[6] E. K. Akpinar and F. Koçyiğit, "Experimental investigation of thermal performance of solar air heater having different obstacles on absorber plates," *Int. Commun. Heat Mass Transf.*, vol. 37, no. 4, pp. 416–421, Apr. 2010, doi: 10.1016/J.ICHEATMASSTRANSFER.2009.11.007.

[7] A. K. Hegde, Raghuvir Pai, and K. V. Karanth, "Performance augmentation of solar air heaters: A comprehensive analysis," *Sol. Energy*, vol. 253, pp. 527–553, Mar. 2023, doi: 10.1016/J.SOLENER.2023.01.031.

[8] A. Hedau and R. P. Saini, "Thermo-hydraulic performance of double pass solar air heater duct having semi-circular tubes and perforated blocks as artificial roughness," *Renew. Energy*, vol. 205, pp. 543–562, Mar. 2023, doi: 10.1016/J.RENENE.2023.01.087.

[9] R. Kumar, A. Sharma, V. Goel, R. Sharma, M. Sethi, and V. V. Tyagi, "An experimental investigation of new roughness patterns (dimples with alternative protrusions) for the performance enhancement of solar air heater," *Renew. Energy*, vol. 211, pp. 964–974, Jul. 2023, doi: 10.1016/J.RENENE.2023.04.111.

[10] V. Kumar and D. Kumar, “A Systematic Review on Firefly Algorithm: Past, Present, and Future,” *Arch. Comput. Methods Eng.*, vol. 28, no. 4, pp. 3269–3291, 2021, doi: 10.1007/s11831-020-09498-y.

[11] F. Marini and B. Walczak, “Particle swarm optimization (PSO). A tutorial,” *Chemom. Intell. Lab. Syst.*, vol. 149, pp. 153–165, Dec. 2015, doi: 10.1016/J.CHEMOLAB.2015.08.020.

[12] Bilal, M. Pant, H. Zaheer, L. Garcia-Hernandez, and A. Abraham, “Differential Evolution: A review of more than two decades of research,” *Eng. Appl. Artif. Intell.*, vol. 90, p. 103479, Apr. 2020, doi: 10.1016/J.ENGAPPAI.2020.103479.

[13] R. V. Rao, V. J. Savsani, and D. P. Vakharia, “Teaching–learning-based optimization: A novel method for constrained mechanical design optimization problems,” *Comput. Des.*, vol. 43, no. 3, pp. 303–315, Mar. 2011, doi: 10.1016/J.CAD.2010.12.015.

[14] M. Dorigo and G. Di Caro, “Ant colony optimization: A new meta-heuristic,” *Proc. 1999 Congr. Evol. Comput. CEC 1999*, vol. 2, pp. 1470–1477, 1999, doi: 10.1109/CEC.1999.782657.

[15] S. Saremi, S. Mirjalili, and A. Lewis, “Grasshopper Optimisation Algorithm: Theory and application,” *Adv. Eng. Softw.*, vol. 105, pp. 30–47, Mar. 2017, doi: 10.1016/J.ADVENGSOFT.2017.01.004.

[16] S. Mirjalili and A. Lewis, “The Whale Optimization Algorithm,” *Adv. Eng. Softw.*, vol. 95, pp. 51–67, May 2016, doi: 10.1016/J.ADVENGSOFT.2016.01.008.

[17] S. Mirjalili, S. M. Mirjalili, and A. Lewis, “Grey Wolf Optimizer,” *Adv. Eng. Softw.*, vol. 69, pp. 46–61, Mar. 2014, doi: 10.1016/J.ADVENGSOFT.2013.12.007.

[18] S. Mirjalili, “Dragonfly algorithm: a new meta-heuristic optimization technique for solving single-objective, discrete, and multi-objective problems,” *Neural Comput. Appl.*, vol. 27, no. 4, pp. 1053–1073, 2016, doi: 10.1007/s00521-015-1920-1.

[19] S. Singh, “Performance evaluation of a novel solar air heater with arched absorber plate,” *Renew. Energy*, vol. 114, pp. 879–886, Dec. 2017, doi: 10.1016/J.RENENE.2017.07.109.

[20] B. kumar Ahirwar and A. kumar, “Review on different techniques used to enhance the thermal performance of solar air heater,” *Int. J. Heat Mass Transf.*, vol. 220, p. 124979, Mar. 2024, doi: 10.1016/J.IJHEATMASSTRANSFER.2023.124979.

[21] E. Vengadesan and R. Senthil, "A review on recent developments in thermal performance enhancement methods of flat plate solar air collector," *Renew. Sustain. Energy Rev.*, vol. 134, no. August, p. 110315, 2020, doi: 10.1016/j.rser.2020.110315.

[22] P. Promvonge, P. Promthaisong, and S. Skullong, "Experimental and numerical thermal performance in solar receiver heat exchanger with trapezoidal louvered winglet and wavy groove," *Sol. Energy*, vol. 236, pp. 153–174, Apr. 2022, doi: 10.1016/J.SOLENER.2022.02.052.

[23] J. S. Sawhney, R. Maithani, and S. Chamoli, "Experimental investigation of heat transfer and friction factor characteristics of solar air heater using wavy delta winglets," *Appl. Therm. Eng.*, vol. 117, pp. 740–751, May 2017, doi: 10.1016/J.APPLTHERMALENG.2017.01.113.

[24] P. Promvonge, P. Tongyote, and S. Skullong, "Thermal behaviors in heat exchanger channel with V-shaped ribs and grooves," *Chem. Eng. Res. Des.*, vol. 150, pp. 263–273, Oct. 2019, doi: 10.1016/J.CHERD.2019.07.025.

[25] Y. Agrawal *et al.*, "Investigation of thermal performance of a ribbed solar air heater for sustainable built environment," *Sustain. Energy Technol. Assessments*, vol. 57, p. 103288, Jun. 2023, doi: 10.1016/J.SETA.2023.103288.

[26] S. Singh, S. Suman, S. Mitra, and M. Kumar, "Thermo-hydraulic performance enhancement of a solar air heater using rotating cylindrical turbulators," *Appl. Therm. Eng.*, vol. 236, p. 121748, Jan. 2024, doi: 10.1016/J.APPLTHERMALENG.2023.121748.

[27] R. Karwa, "Thermo-hydraulic performance of solar air heater with finned absorber plate forming multiple rectangular air flow passages in parallel under laminar flow conditions," *Appl. Therm. Eng.*, vol. 221, p. 119673, Feb. 2023, doi: 10.1016/J.APPLTHERMALENG.2022.119673.

[28] A. Kumar *et al.*, "Correlation development for Nusselt number and friction factor of a multiple type V-pattern dimpled obstacles solar air passage," *Renew. Energy*, vol. 109, pp. 461–479, 2017, doi: 10.1016/j.renene.2017.03.030.

[29] S. Şevik, Ö. Özdilli, and M. Abuşka, "Experimental investigation of relative roughness height effect in solar air collector with convex dimples," *Renew. Energy*, vol. 194, pp. 100–116, Jul. 2022, doi: 10.1016/j.renene.2022.05.088.

[30] M. Salman, R. Chauhan, G. kumar Poongavanam, M. H. Park, and S. C. Kim, "Utilizing jet impingement on protrusion/dimple heated plate to improve the

performance of double pass solar heat collector," *Renew. Energy*, vol. 181, pp. 653–665, Jan. 2022, doi: 10.1016/j.renene.2021.09.082.

[31] R. P. Saini and J. Verma, "Heat transfer and friction factor correlations for a duct having dimple-shape artificial roughness for solar air heaters," *Energy*, vol. 33, no. 8, pp. 1277–1287, 2008, doi: 10.1016/j.energy.2008.02.017.

[32] S. D. Hwang, H. G. Kwon, and H. H. Cho, "Local heat transfer and thermal performance on periodically dimple-protrusion patterned walls for compact heat exchangers," *Energy*, vol. 35, no. 12, pp. 5357–5364, 2010, doi: 10.1016/j.energy.2010.07.022.

[33] M. Sethi, Varun, and N. S. Thakur, "Correlations for solar air heater duct with dimpled shape roughness elements on absorber plate," *Sol. Energy*, vol. 86, no. 9, pp. 2852–2861, Sep. 2012, doi: 10.1016/J.SOLENER.2012.06.024.

[34] L. Luo, F. Wen, L. Wang, B. Sundén, and S. Wang, "On the solar receiver thermal enhancement by using the dimple combined with delta winglet vortex generator," *Appl. Therm. Eng.*, vol. 111, pp. 586–598, Jan. 2017, doi: 10.1016/J.APPLTHERMALENG.2016.09.096.

[35] V. Kumar, "Experimental investigation of exergetic efficiency of 3 side concave dimple roughened absorbers," *Energy*, vol. 215, Jan. 2021, doi: 10.1016/j.energy.2020.119039.

[36] R. Kumar, A. Sharma, V. Goel, R. Sharma, M. Sethi, and V. V. Tyagi, "An experimental investigation of new roughness patterns (dimples with alternative protrusions) for the performance enhancement of solar air heater," *Renew. Energy*, vol. 211, pp. 964–974, Jul. 2023, doi: 10.1016/j.renene.2023.04.111.

[37] B. Bhushan and R. Singh, "Nusselt number and friction factor correlations for solar air heater duct having artificially roughened absorber plate," *Sol. Energy*, vol. 85, no. 5, pp. 1109–1118, May 2011, doi: 10.1016/j.solener.2011.03.007.

[38] M. Salman, R. Chauhan, G. K. Poongavanam, and S. C. Kim, "Analytical investigation of jet impingement solar air heater with dimple-roughened absorber surface via thermal and effective analysis," *Renew. Energy*, vol. 199, pp. 1248–1257, Nov. 2022, doi: 10.1016/j.renene.2022.09.092.

[39] S. Panda and R. Kumar, "Combined effect of solar intensity and air mass flow rate on inline spherical dimple based solar air heater during summer season," *Sol. Energy*, vol. 258, pp. 156–174, Jul. 2023, doi: 10.1016/j.solener.2023.05.002.

[40] R. Shaik, E. Punna, and S. K. Gugulothu, “Optimisation of thermohydraulic performance of triangular duct solar air heater with alternative dimple shaped protrusion and intrusion on the absorber plate,” *Therm. Sci. Eng. Prog.*, vol. 42, p. 101957, Jul. 2023, doi: 10.1016/j.tsep.2023.101957.

[41] N. Arya and V. Goel, “Comparative study of V-ribs miniature with dimple hybrid roughness along with dimples shaped roughness used in solar air heating system,” *Energy Sources, Part A Recover. Util. Environ. Eff.*, vol. 45, no. 2, pp. 3297–3317, Jun. 2023, doi: 10.1080/15567036.2023.2195822.

[42] C. Prakash and R. P. Saini, “Heat transfer and friction in rectangular solar air heater duct having spherical and inclined rib protrusions as roughness on absorber plate,” *Exp. Heat Transf.*, vol. 32, no. 5, pp. 469–487, Sep. 2019, doi: 10.1080/08916152.2018.1543367.

[43] L. B. Raju, G. R. Sastry, S. K. Gugulothu, R. Kumar, and D. Balakrishnan, “Computational analysis on solar air heater with combination of alternate dimple protrusions and intrusions on absorber plate with one rounded corner triangular duct,” *Environ. Sci. Pollut. Res.*, 2022, doi: 10.1007/s11356-022-24625-x.

[44] H. K. Moon, T. O’Connell, and B. Glezer, “Channel Height Effect on Heat Transfer and Friction in a Dimpled Passage,” in *Volume 3: Heat Transfer; Electric Power; Industrial and Cogeneration*, American Society of Mechanical Engineers, Jun. 1999. doi: 10.1115/99-GT-163.

[45] M. K. Chyu, Y. Yu, H. Ding, J. P. Downs, and F. O. Soechting, “Concavity Enhanced Heat Transfer in an Internal Cooling Passage,” in *Volume 3: Heat Transfer; Electric Power; Industrial and Cogeneration*, American Society of Mechanical Engineers, Jun. 1997. doi: 10.1115/97-GT-437.

[46] N. Syred, A. Khalatov, A. Kozlov, A. Shchukin, and R. Agachev, “Effect of Surface Curvature on Heat Transfer and Hydrodynamics Within a Single Hemispherical Dimple,” *J. Turbomach.*, vol. 123, no. 3, pp. 609–613, Jul. 2001, doi: 10.1115/1.1348020.

[47] S. W. Moon and S. C. Lau, “Turbulent Heat Transfer Measurements on a Wall With Concave and Cylindrical Dimples in a Square Channel,” in *Volume 3: Turbo Expo 2002, Parts A and B*, ASMEDC, Jan. 2002, pp. 459–467. doi: 10.1115/GT2002-30208.

[48] A. Khalatov, A. Byerley, D. Ochoa, and S.-K. Min, “Flow Characteristics Within and Downstream of Spherical and Cylindrical Dimple on a Flat Plate at Low

Reynolds Numbers," in *Volume 3: Turbo Expo 2004*, ASMEDC, Jan. 2004, pp. 589–602. doi: 10.1115/GT2004-53656.

[49] S. Yadav, Varun, Siddhartha, and M. Kaushal, "Heat Transfer and Frictional Characteristics of Rectangular Channel Air Heater Duct Having Protrusion as Roughness Elements," *J. Inst. Eng. Ser. C*, vol. 93, no. 4, pp. 307–312, Oct. 2012, doi: 10.1007/s40032-012-0047-8.

[50] R. Nadda, R. Maithani, and A. Kumar, "Effect of multiple arc protrusion ribs on heat transfer and fluid flow of a circular-jet impingement solar air passage," *Chem. Eng. Process. - Process Intensif.*, vol. 120, pp. 114–133, Oct. 2017, doi: 10.1016/j.cep.2017.07.005.

[51] A. P. Singh, Varun, and Siddhartha, "Heat transfer and friction factor correlations for multiple arc shape roughness elements on the absorber plate used in solar air heaters," *Exp. Therm. Fluid Sci.*, vol. 54, pp. 117–126, Apr. 2014, doi: 10.1016/j.expthermflusci.2014.02.004.

[52] M. A. Elyyan, A. Rozati, and D. K. Tafti, "Investigation of dimpled fins for heat transfer enhancement in compact heat exchangers," *Int. J. Heat Mass Transf.*, vol. 51, no. 11–12, pp. 2950–2966, Jun. 2008, doi: 10.1016/j.ijheatmasstransfer.2007.09.013.

[53] Y.-L. Lin, T. I.-P. Shih, and M. K. Chyu, "Computations of Flow and Heat Transfer in a Channel With Rows of Hemispherical Cavities," in *Volume 3: Heat Transfer; Electric Power; Industrial and Cogeneration*, American Society of Mechanical Engineers, Jun. 1999. doi: 10.1115/99-GT-263.

[54] P. M. Ligrani, N. K. Burgess, and S. Y. Won, "Nusselt Numbers and Flow Structure on and Above a Shallow Dimpled Surface Within a Channel Including Effects of Inlet Turbulence Intensity Level," *J. Turbomach.*, vol. 127, no. 2, pp. 321–330, Apr. 2005, doi: 10.1115/1.1861913.

[55] S. Acharya and F. Zhou, "Experimental and Computational Study of Heat/Mass Transfer and Flow Structure for Four Dimple Shapes in a Square Internal Passage," *J. Turbomach.*, vol. 134, no. 6, Nov. 2012, doi: 10.1115/1.4006315.

[56] Varun and Siddhartha, "Thermal performance optimization of a flat plate solar air heater using genetic algorithm," *Appl. Energy*, vol. 87, no. 5, pp. 1793–1799, May 2010, doi: 10.1016/J.APENERGY.2009.10.015.

[57] M. Ansari and M. Bazargan, “Optimization of flat plate solar air heaters with ribbed surfaces,” *Appl. Therm. Eng.*, vol. 136, pp. 356–363, May 2018, doi: 10.1016/J.APPLTHERMALENG.2018.02.099.

[58] J. Hu, K. Liu, L. Ma, and X. Sun, “Parameter optimization of solar air collectors with holes on baffle and analysis of flow and heat transfer characteristics,” *Sol. Energy*, vol. 174, pp. 878–887, Nov. 2018, doi: 10.1016/J.SOLENER.2018.09.075.

[59] R. Kumar, V. Goel, P. Singh, A. Saxena, A. S. Kashyap, and A. Rai, “Performance evaluation and optimization of solar assisted air heater with discrete multiple arc shaped ribs,” *J. Energy Storage*, vol. 26, p. 100978, Dec. 2019, doi: 10.1016/J.EST.2019.100978.

[60] B. S. Qader, E. E. Supeni, M. K. A. Ariffin, and A. R. A. Talib, “RSM approach for modeling and optimization of designing parameters for inclined fins of solar air heater,” *Renew. Energy*, vol. 136, pp. 48–68, Jun. 2019, doi: 10.1016/J.RENENE.2018.12.099.

[61] A. Gholami, Y. Ajabshirchi, and S. F. Ranjbar, “Thermo-economic optimization of solar air heaters with arcuate-shaped obstacles,” *J. Therm. Anal. Calorim.*, vol. 138, no. 2, pp. 1395–1403, 2019, doi: 10.1007/s10973-019-08273-x.

[62] R. Chauhan and S. C. Kim, “Thermo-hydraulic characterization and design optimization of dimpled/protruded absorbers in solar heat collectors,” *Appl. Therm. Eng.*, vol. 154, pp. 217–227, May 2019, doi: 10.1016/J.APPLTHERMALENG.2019.03.094.

[63] C. P. Mohanty *et al.*, “Environmental Effects Parametric performance optimization of three sides roughened solar air heater solar air heater,” *Energy Sources, Part A Recover. Util. Environ. Eff.*, vol. 00, no. 00, pp. 1–21, 2020, doi: 10.1080/15567036.2020.1752855.

[64] P. T. Saravanakumar, D. Somasundaram, and M. M. Matheswaran, “Exergetic investigation and optimization of arc shaped rib roughened solar air heater integrated with fins and baffles,” *Appl. Therm. Eng.*, vol. 175, p. 115316, Jul. 2020, doi: 10.1016/J.APPLTHERMALENG.2020.115316.

[65] D. J. Dezan, A. D. Rocha, and W. G. Ferreira, “Parametric sensitivity analysis and optimisation of a solar air heater with multiple rows of longitudinal vortex generators,” *Appl. Energy*, vol. 263, p. 114556, Apr. 2020, doi: 10.1016/J.APENERGY.2020.114556.

[66] V. S. Korpale, S. P. Deshmukh, C. S. Mathpati, and V. H. Dalvi, "Numerical simulations and optimization of solar air heaters," *Appl. Therm. Eng.*, vol. 180, p. 115744, Nov. 2020, doi: 10.1016/J.APPLTHERMALENG.2020.115744.

[67] P. J. Bezbaruah, R. S. Das, and B. K. Sarkar, "Overall performance analysis and GRA optimization of solar air heater with truncated half conical vortex generators," *Sol. Energy*, vol. 196, pp. 637–652, Jan. 2020, doi: 10.1016/J.SOLENER.2019.12.057.

[68] A. Kumar and A. Layek, "Thermo-hydraulic performance of roughened solar air heater by design of experiment and meta-heuristic approach," *Therm. Sci. Eng. Prog.*, vol. 10, pp. 92–102, May 2019, doi: 10.1016/J.TSEP.2019.01.011.

[69] L. Luo, W. Du, S. Wang, L. Wang, B. Sundén, and X. Zhang, "Multi-objective optimization of a solar receiver considering both the dimple/protrusion depth and delta-winglet vortex generators," *Energy*, vol. 137, pp. 1–19, Oct. 2017, doi: 10.1016/J.ENERGY.2017.07.001.

[70] A. Sharma *et al.*, "Optimizing discrete V obstacle parameters using a novel Entropy-VIKOR approach in a solar air flow channel," *Renew. Energy*, vol. 106, pp. 310–320, Jun. 2017, doi: 10.1016/j.renene.2017.01.010.

[71] A. Acır, M. E. Canlı, İ. Ata, and R. Çakıroğlu, "Parametric optimization of energy and exergy analyses of a novel solar air heater with grey relational analysis," *Appl. Therm. Eng.*, vol. 122, pp. 330–338, Jul. 2017, doi: 10.1016/j.applthermaleng.2017.05.018.

[72] R. Kumar *et al.*, "Parametric optimization of an impingement jet solar air heater for active green heating in buildings using hybrid CRITIC-COPRAS approach," *Int. J. Therm. Sci.*, vol. 197, p. 108760, Mar. 2024, doi: 10.1016/j.ijthermalsci.2023.108760.

[73] G. K. Pramod, U. C. Arunachala, N. Madhwesh, and M. S. Manjunath, "A comprehensive review on the effect of turbulence promoters on heat transfer augmentation of solar air heater and the evaluation of thermo-hydraulic performance using metaheuristic optimization algorithms," *Environ. Dev. Sustain.*, Feb. 2024, doi: 10.1007/s10668-023-04402-7.

[74] P. K. Mishra, R. Nadda, R. Kumar, A. Rana, M. Sethi, and A. Ekileski, "Optimization of multiple arcs protrusion obstacle parameters using AHP-TOPSIS approach in an impingement jet solar air passage," *Heat Mass Transf.*, vol. 54, no. 12, pp. 3797–3808, Dec. 2018, doi: 10.1007/s00231-018-2405-4.

[75] V. C. S. S. and A. H. S., "Nature inspired meta heuristic algorithms for optimization problems," *Computing*, vol. 104, no. 2, pp. 251–269, Feb. 2022, doi: 10.1007/s00607-021-00955-5.

[76] Standard, A.S.H.R.A.E., "Methods of testing to determine the thermal performance of solar collectors," Inc. New York, NY, USA, 1977.

[77] D. Singh and V. Kumar, "Thermal performance investigation of frustum roughened solar air heater," *Sol. Energy*, vol. 255, pp. 339–354, May 2023, doi: 10.1016/j.solener.2023.03.036.

[78] R. V. Rao, "Design of a Smooth Flat Plate Solar Air Heater Using TLBO and ETLBO Algorithms," in *Teaching Learning Based Optimization Algorithm*, Cham: Springer International Publishing, 2016, pp. 137–161. doi: 10.1007/978-3-319-22732-0_10.

[79] R. Venkata Rao and G. Waghmare, "Optimization of thermal performance of a smooth flat-plate solar air heater using teaching–learning-based optimization algorithm," *Cogent Eng.*, vol. 2, no. 1, p. 997421, Dec. 2015, doi: 10.1080/23311916.2014.997421.

[80] J. A. Duffie (Deceased), W. A. Beckman, and N. Blair, *Solar Engineering of Thermal Processes, Photovoltaics and Wind*. Wiley, 2020. doi: 10.1002/9781119540328.

[81] S.Verma and B.Prasad, "Investigation for the optimal thermohydraulic performance of artificially roughened solar air heaters," *Renew. Energy*, vol. 20, no. 1, pp. 19–36, May 2000, doi: 10.1016/S0960-1481(99)00081-6.

[82] R. K. Ravi and R. P. Saini, "Experimental investigation on performance of a double pass artificial roughened solar air heater duct having roughness elements of the combination of discrete multi V shaped and staggered ribs," *Energy*, vol. 116, pp. 507–516, Dec. 2016, doi: 10.1016/j.energy.2016.09.138.

[83] F. W. Dittus and L. M. K. Boelter, "Heat transfer in automobile radiators of the tubular type," *Int. Commun. Heat Mass Transf.*, vol. 12, no. 1, pp. 3–22, Jan. 1985, doi: 10.1016/0735-1933(85)90003-X.

[84] M.S.Bhatti, "Turbulent and Transition Flow Convective Heat Transfer in Ducts," in *Handbook of Single-Phase Convective Heat Transfer*, 1987.

[85] S. J. Kline and F. A. McClintock, "Describing Uncertainties in Single-Sample Experiments," *Mech. Eng.*, vol. 75, no. 1, pp. 3–8, 1953.

[86] G. Xie, J. Liu, P. M. Ligrani, and W. Zhang, "Numerical analysis of flow structure and heat transfer characteristics in square channels with different internal-protruded

dimple geometrics," *Int. J. Heat Mass Transf.*, vol. 67, pp. 81–97, Dec. 2013, doi: 10.1016/j.ijheatmasstransfer.2013.07.094.

[87] J. J. Liu, M. Yamamoto, and L. Yan, "On the uniqueness and reconstruction for an inverse problem of the fractional diffusion process," *Appl. Numer. Math.*, vol. 87, pp. 1–19, Jan. 2015, doi: 10.1016/j.apnum.2014.08.001.

[88] S. Panda and R. Kumar, "Flow friction and thermal performance of dimple imprinted based solar air-heater: A numerical study," *Numer. Heat Transf. Part A Appl.*, vol. 84, no. 1, pp. 35–53, Jul. 2023, doi: 10.1080/10407782.2022.2105066.

[89] S. Chamoli and N. S. Thakur, "Heat transfer enhancement in solar air heater with V-shaped perforated baffles," *J. Renew. Sustain. Energy*, vol. 5, no. 2, Mar. 2013, doi: 10.1063/1.4798411.

[90] A. Kumar, Akshayveer, A. P. Singh, and O. P. Singh, "Investigations for efficient design of a new counter flow double-pass curved solar air heater," *Renew. Energy*, vol. 185, pp. 759–770, Feb. 2022, doi: 10.1016/j.renene.2021.12.101.

[91] R. Kumar, S. Kumar, R. Nadda, K. Kumar, and V. Goel, "Thermo-hydraulic efficiency and correlation development of an indoor designed jet impingement solar thermal collector roughened with discrete multi-arc ribs," *Renew. Energy*, vol. 189, pp. 1259–1277, Apr. 2022, doi: 10.1016/j.renene.2022.03.037.

[92] R. L. Webb, "Performance evaluation criteria for use of enhanced heat transfer surfaces in heat exchanger design," *Int. J. Heat Mass Transf.*, vol. 24, no. 4, pp. 715–726, Apr. 1981, doi: 10.1016/0017-9310(81)90015-6.

[93] M. Nanjundappa, "Optimum thermo-hydraulic performance of solar air heater provided with cubical roughness on the absorber surface," *Exp. Heat Transf.*, vol. 33, no. 4, pp. 374–387, Jun. 2020, doi: 10.1080/08916152.2019.1652214.

[94] A. L. Antony, S. P. Shetty, N. Madhwesh, N. Yagnesh Sharma, and K. Vasudeva Karanth, "Influence of stepped cylindrical turbulence generators on the thermal enhancement factor of a flat plate solar air heater," *Sol. Energy*, vol. 198, pp. 295–310, Mar. 2020, doi: 10.1016/j.solener.2020.01.065.

[95] L. N. Azadani and N. Gharouni, "Multi objective optimization of cylindrical shape roughness parameters in a solar air heater," *Renew. Energy*, vol. 179, pp. 1156–1168, Dec. 2021, doi: 10.1016/j.renene.2021.07.084.

[96] V. Goel, R. Kumar, S. Bhattacharyya, V. V. Tyagi, and A. M. Abusorrah, "A comprehensive parametric investigation of hemispherical cavities on thermal performance and flow-dynamics in the triangular-duct solar-assisted air-heater,"

Renew. Energy, vol. 173, pp. 896–912, Aug. 2021, doi: 10.1016/j.renene.2021.04.006.

30/12/2025

30-12-2025

Professor
Dept. of Mechanical Engineering
Jadavpur University, Kolkata-32

Applied Thermal Engineering 242 (2024) 122537

Contents lists available at ScienceDirect

Applied Thermal Engineering

journal homepage: www.elsevier.com/locate/apthermeng

Research Paper

Parametric optimization of solar air heaters with dimples on absorber plates using metaheuristic approaches

Premchand Kumar Mahto [a,b], Partha Protim Das [b], Sunny Diyaley [b], Balaram Kundu [a,*]

[a] Mechanical Engineering Department, Jadavpur University, 188, Raja S.C. Mallick Rd, Kolkata 700032, West Bengal, India
[b] Mechanical Engineering Department, Sikkim Manipal Institute of Technology, Sikkim Manipal University, Majhitar, Sikkim, India

ARTICLE INFO

Keywords:
Solar air heater
Dimple
Metaheuristic algorithms
Single and multi-objective optimization

ABSTRACT

The performance optimization analysis of artificially roughened solar air heaters (SAH) becomes complex due to the inherent difficulties of the optimization analytical processes. Metaheuristic algorithms can be employed as optimization methodologies to handle complex engineering problems with minimal computational efforts and high accuracy. However, due to their stochastic nature, only some metaheuristic algorithms are suitable for solving a specific problem. Hence, there is a need to perform a comparative performance analysis of different metaheuristic algorithms in optimizing SAH. The current paper presents a comparative performance analysis of four metaheuristics algorithms, i.e., Firefly algorithm (FA), Particle swarm optimization (PSO), Differential evolution (DE), and Teaching learning-based optimization (TLBO), in optimizing the system and operating parameters of SAH. Two types of artificially roughened SAH absorber plate design patterns have been taken: dimpled plate in a zig-zag pattern and straight-line pattern. Both single and multi-objective optimization techniques are carried out while viewing the maximization of Nusselt number (Nu) and minimization of friction factor (F_f) as two objective functions in single-objective optimization. Results showed that the TLBO algorithm delivered better optimal solutions for single and multi-objective optimization than the other three metaheuristic algorithms. In the single-objective optimization, the maximum improvement in Nu and F_f is 16.81 % and 3.61 %, respectively. In the multi-objective optimization of a zig-zag pattern, the suitable parametric setting is Re = 20000, S/e = 30.83, L/e = 30.83, and d/D = 0.2515 for the optimal value of Nu and F_f as 204.7034 and 0.0134, respectively. For a straight-line pattern, the optimal values for Nu and F_f are 108.6901 and 0.0237, respectively at Re = 12000, p/e = 12, and e/D = 0.0379.

1. Introduction

The world in the present scenario has witnessed two major concerns, one related to global environmental pollution and, secondly, the rising demand for energy requirements, which are likely to gain attention soon. Switching towards various renewable energy sources is paramount to maintaining the appropriate fulcrum between environment-responsive and sustainable energy sources. Different renewable energy sources are rapidly being used to fulfil daily energy requirements. Solar energy is one of the important sustainable energy sources used in direct heating, indirect heating, and photovoltaic (PV). Solar heat collectors play a significant role in directly utilizing solar energy by trapping solar thermal energy [1]. As per the global data, a massive amount of energy is being used for space heating, and it continuously increases due to the increase in pollution, standard of living, and industrialization. So, solar air heaters (SAHs) find space for utilization, as solar thermal energy is abundantly available on the earth's surface. SAH can be predominantly utilized in the agricultural sector to process farm products. It can also be used for different purposes, such as drying laundry, paper, food products, bricks, minerals, coal, etc [2]. SAH is comparatively cheap and requires a nominal expenditure on maintenance. However, it has poor thermo-hydraulic performance because of the squat thermo-physical properties of the air and the generation of a laminar sub-layer adjacent to the heated surface [3]. This laminar sub-layer obstructs heat transfer between the absorber plate and the transport medium (air). Therefore, seeing the vast applicability of solar air heaters, the scientific community is continuously trying to improve the performance of solar air heaters. Providing an artificial roughness in the absorber plate of SAHs is a prominent methodology to uplift performance [4,5]. Numerous pieces of literature are already available on the performance evaluation of SAHs with different shapes/patterns of roughness

* Corresponding author.
E-mail address: bkundu@mech.net.in (B. Kundu).

https://doi.org/10.1016/j.applthermaleng.2024.122537
Received 30 August 2023; Received in revised form 15 December 2023; Accepted 23 January 2024
Available online 26 January 2024

International Communications in Heat and Mass Transfer 154 (2024) 107440

Contents lists available at ScienceDirect

International Communications in Heat and Mass Transfer

journal homepage: www.elsevier.com/locate/ichmt

Experimental and meta-heuristic optimization for the highest thermo-hydraulic performance of a solar air heater with a V-notch pattern of hemispherical protrusions on absorber surfaces

Premchand Kumar Mahto [a,b], Balaram Kundu [b,*]

[a] Department of Mechanical Engineering, Sikkim Manipal Institute of Technology, Sikkim Manipal University, Majhitar 737136, Sikkim, India
[b] Department of Mechanical Engineering, Jadavpur University, Kolkata 700032, West Bengal, India

ARTICLE INFO

Keywords:
Artificial roughness
Hemispherical protrusion
Metaheuristic algorithms
Nusselt number
Friction factor

ABSTRACT

Thermo-hydraulic performances of a new solar air heater with single V-notch patterns of hemispherical protrusions on the absorber plate are investigated experimentally for different relative protrusion heights (h_p/D_h = 0.027–0.069), relative pitch (p_p/h_p = 6–14), attack angle (α_{ap} = 15°-75°), and Reynolds number (*Re* =3600–21,700). Three meta-heuristic algorithms, i.e., Ant colony optimization (ACO), Whale optimization algorithm (WOA), and Grass-hopper optimization algorithm (GOA), were used for single and multi-objective optimizations. Experimental results provide the maximum Nusselt number (*Nu*) as 127.07 at $h_p/D_h = 0.050$, $p_p/h_p = 10$, $\alpha_{ap} = 60^0$, and *Re* =21,700, whereas the minimum friction factor (*f*) becomes 0.0165 at $h_p/D_h = 0.027$, $p_p/h_p = 10$, $\alpha_{ap} = 45^0$, and *Re* =21,700. The highest normalized Nusselt number (Nu/Nu_s) is found to be 2.56 for $h_p/D_h = 0.050$, $p_p/h_p = 10$, $\alpha_{ap} = 60^0$, and *Re* =7200, and the maximum normalized friction factor (f/f_s) is observed as 4.30 at $h_p/D_h = 0.050$, $p_p/h_p = 10$, $\alpha_{ap} = 45^0$, and *Re* =7200. The highest thermo-hydraulic performance parameter (THPP) was to be 1.60 at $p_p/h_p = 10$, $h_p/D_h = 0.050$, $\alpha_{ap} = 60^0$, and *Re* =7200. Empirical correlations were developed. In single objective optimization for Nu, WOA provided the best results. For *f*, WOA gives a minimum value. The WOA metaheuristic algorithm outperformed the other algorithms.

1. Introduction

The rapid depletion of nonrenewable energy sources is a significant concern and a challenge to the very existence of humans [1]. The current energy scenario in the world has become necessary to shift focus towards more sustainable energy solutions. Hence, the dependency on fossil fuels must be minimized, and the search for better and more efficient renewable energy sources is essential. The evolution of renewable technologies has optimistic effects on the global economy and the development of nations. Renewable energy technologies are beneficial as they are clean energy sources with less environmental impact than nonrenewable energy sources. Investment in renewable energy leads to a reduction in energy expenses, the creation of job opportunities, and monetary benefits. Like any other human activity, all energy sources significantly impact our environment. However, renewable energy has a much lesser impact in terms of pollution [2,3].

1.1. Solar air heater

Solar energy is abundantly available on the earth's surface and could be subjugated in various applications. Along with being an inexhaustible energy source, it is also a clean energy source and can be supplied without harm to the environment. Solar air heating has many applications, such as space heating, wood seasoning, crop drying, etc. [4]. Solar air heaters absorb irradiation and alter it into heat through a medium (Air/Water).

Solar air heaters (SAHs) are generally cheap as they use less material to fabricate and are more compact than Solar Water Heaters. However, these solar air heaters have low thermal efficiency because of their low heat transfer from absorber plates to the air flowing in the duct. The low convective heat transfer coefficient is due to generating a viscous sub-layer, also called a laminar sub-layer [5]. The collector design must be improved to increase the heat transfer coefficient and thermal performance. In past research, various methods have been used to improve the thermo-hydraulic performance of SAHs [6].

* Corresponding author.
E-mail address: bkundu@mech.net.in (B. Kundu).

https://doi.org/10.1016/j.icheatmasstransfer.2024.107440

Available online 1 April 2024

International Journal of Thermal Sciences 220 (2026) 110435

Contents lists available at ScienceDirect

International Journal of Thermal Sciences

journal homepage: www.elsevier.com/locate/ijts

Thermo-hydraulic characteristics of solar air heaters designed with semi-capsule-shaped protrusions arranged in a staggered pattern

Premchand Kumar Mahto [a,b], Balaram Kundu [a,*]

[a] Department of Mechanical Engineering, Jadavpur University, Kolkata, 700032, West Bengal, India
[b] Department of Mechanical Engineering, Sikkim Manipal Institute of Technology, Sikkim Manipal University, Majhitar, 737136, Sikkim, India

ARTICLE INFO

Keywords:
Solar air heater
Semi-capsule protrusion
Nusselt number
Friction factor
Thermo-hydraulic performance index
Metaheuristic optimization

ABSTRACT

This paper investigates the thermo-hydraulic performance of a solar air heater featuring semi-capsule-shaped protrusions on the absorber plate. The study focuses on key parameters: the Nusselt number (*Nu*) and the friction factor (f_f), while varying factors such as relative protrusion heights, relative pitch, protrusion angle, and Reynolds number. Experimental results reveal a maximum Nusselt number of 182.62, indicating a 3.14-fold improvement in heat transfer compared to conventional designs, and a maximum friction factor of 0.073, which is 6.66 times lower than that of traditional heaters. The thermo-hydraulic performance index (THPi) reached a maximum of 2.06. Four metaheuristic optimization algorithms were evaluated, with Whale Optimization Algorithm (WOA) found to be the most effective for both single- and multi-objective optimization. The research highlights significant potential for enhancing the performance of solar air heaters.

1. Introduction

The Earth is undergoing a significant transition from fossil fuels to renewable energy resources driven by severe weather changes and the growing demand for cleaner energy [1]. Solar energy, in particular, offers several benefits and stands out as a major renewable energy source. It reduces greenhouse gas emissions, promotes energy independence, and provides clean energy at competitive prices. By harnessing solar energy in its thermal or photovoltaic forms, we could significantly contribute to meeting global energy needs. Harnessing thermal energy is a straightforward process that can be applied in various contexts, such as water heating, air and space heating, and crop drying, among others [2,3]. Solar air heaters (SAHs) are widely used thermal devices that capture solar thermal energy by warming the air around them. Despite the many advantages of solar air heaters, including a simple design, ease of fabrication, low manufacturing costs, and minimal maintenance, their overall thermal performance is relatively low. This limitation presents a significant barrier to the widespread adoption of these technologies in various applications. The insufficient thermal performance is primarily due to several factors: the low quality of the thermo-physical properties of air, a limited absorber surface area, low convection rates, a short air flow duration, and the formation of a laminar sub-layer near the absorber plate [4,5].

Researchers have employed various active approaches to enhance the performance of solar air heaters [6]. One efficient approach is to add artificial roughness to the absorber plate. This roughness disrupts air flow, creating eddies and secondary flows that enhance heat transfer [7]. However, it is essential to note that artificial roughness also leads to increased losses, which in turn increase the energy consumption required for pumping.

To achieve maximum heat transfer while minimizing friction loss, the geometric features of artificial roughness are crucial. Protrusions or dimples are commonly created for artificial roughness due to their lightweight properties and the ease of manufacturing the absorber plate [8]. Sevik et al. [9] investigated the impact of roughness height on the absorber performance of solar air collectors with convex dimples. They discovered that these collectors were 0.32 times more efficient than conventional flat plates. Kumar et al. [10] designed an interior structure to enhance the performance of the jet solar thermal collector, finding that the maximum thermo-hydraulic efficiency was 7.61 times greater than that of a traditional channel. Salman et al. [11] investigated a double-pass solar collector to analyze the impact of jets on a heated plate with protrusions or dimples, aiming to increase efficiency. Their results indicated that the efficiency improved by a factor of 3.86 compared to a flat surface, measured at a Reynolds number of 15,000. Salman et al. [12] discovered that the jet impingement solar collector outperforms

* Corresponding author.
E-mail address: bkundu@mech.net.in (B. Kundu).

https://doi.org/10.1016/j.ijthermalsci.2025.110435
Received 4 April 2025; Received in revised form 29 September 2025; Accepted 27 October 2025
Available online 4 November 2025

engineering proceedings

MDPI

Proceeding Paper

Parametric Optimization of Solar Air Heaters Having Hemispherical Protrusion Roughness in the V-Notch Pattern on the Absorber Plate: A Metaheuristics Optimization Approach †

Premchand Kumar Mahto [1,2,*] and Balaram Kundu [2,*]

[1] Department of Mechanical Engineering, Sikkim Manipal Institute of Technology, Sikkim Manipal University, Majhitar 737136, Sikkim, India
[2] Department of Mechanical Engineering, Jadavpur University, Kolkata 700032, West Bengal, India
* Correspondence: prem4es@gmail.com (P.K.M.); bkundu@mech.net.in (B.K.)
† Presented at the International Conference on Recent Advances in Science and Engineering, Dubai, United Arab Emirates, 4–5 October 2023.

Abstract: Artificial roughness in the form of protrusions has become a popular technique to improve the thermohydraulic performance of SAHs. So, utmost attention should also be given to determining the suitable parametric values that directly affect the performance of SAHs. Hence, in this work, an attempt has been made to optimize the performance of solar air heaters having hemispherical protrusion roughness in a V-notch pattern on an absorber plate using two different metaheuristic optimization algorithms, i.e., the grey wolf optimization (GWO) algorithm and the dragonfly (DA) algorithm. This study makes use of the correlation equations for the friction factor (f_f) and Nusselt number (Nu), which were developed after conducting the experiments. Four independent parameters, namely the Reynolds number (Re = 3600–21,700), relative protrusion height (e_p/D_h = 0.027–0.069), relative pitch (p/e_p = 6–14), and attack angle (α_a = 15°–75°), were considered to obtain the optimal values of Nu and f_f. In single-objective optimization, the maximization of Nu and the minimization of f_f are two objective functions. The GWO has delivered the best solutions for both objectives with a faster computational rate and less variation. A convergence curve and box plot validated these findings. The maximum value of Nu was found to be 144.567, corresponding to Re = 21,700, e_p/D_h = 0.07, p/e_p = 8.54, and $\alpha_a = 75^0$, and the minimum value of f_f was found to be 0.012, corresponding to Re = 21,700, e_p/D_h = 0.03, p/e_p = 14, and α_a = 15°. Pareto multi-objective optimization provides compromised solutions that provide flexibility to the decision maker in selecting a parametric setting.

Keywords: metaheuristic; optimization; solar air heater; hemispherical protrusion; Nusselt number; friction factor

Citation: Mahto, P.K.; Kundu, B. Parametric Optimization of Solar Air Heaters Having Hemispherical Protrusion Roughness in the V-Notch Pattern on the Absorber Plate: A Metaheuristics Optimization Approach. *Eng. Proc.* **2023**, *59*, 183. https://doi.org/10.3390/engproc2023059183

Academic Editors: Nithesh Naik, Rajiv Selvam, Pavan Hiremath, Suhas Kowshik CS and Ritesh Ramakrishna Bhat

Published: 18 January 2024

1. Introduction

In recent years, the demand for electricity requirements has increased drastically due to technological enhancement, population growth, and an improvement in the standards of living [1]. So, people are searching for alternative energy resources, i.e., solar, wind, and hydro, to fulfill the energy demand. Solar thermal energy can be used for various purposes, like air heating, water heating, drying, etc. A solar air heater heats ambient air by trapping solar thermal energy, but it has low thermal performance due to the formation of a laminar sub-layer over a heated absorber plate [2]. Various techniques, such as packed beds, ribs, fins, dimples, and protrusion, are used to improve the thermohydraulic performance by breaking the laminar sub-layer [3–5]. Artificial roughness, such as dimples and protrusions, has become the most popular technique [6–9]. Employing roughness in the absorber plate increases the convective heat transfer by breaking the laminar sub-layer and developing a secondary flow; however, it also increases the pressure drop due to friction. Hence, it